

## **Use Authorization**

In presenting this thesis in partial fulfillment of the requirements for an advanced degree at Idaho State University, I agree that the Library shall make it freely available for inspection.

I further state that permission to download and/or print my thesis for scholarly purposes may be granted by the Dean of the Graduate School, Dean of my academic division, or by the University Librarian. It is understood that any copying or publication of this thesis for financial gain shall not be allowed without my written permission.

Signature \_\_\_\_\_

Date \_\_\_\_\_

LightGauge®: Production of Photonic Sensor Devices on Nuclear Materials

By

Scott McBeath

A thesis submitted in partial fulfillment of the requirements for the degree of

MASTER OF SCIENCE

in

NUCLEAR SCIENCE AND ENGINEERING

Idaho State University

2014

To the Graduate Faculty:

The members of the committee appointed to examine the thesis of SCOTT  
CHRISTOPHER MCBEATH find it satisfactory and recommend that it be accepted.

---

Eric Burgett

Major Advisor

---

Tony Hill

Committee Member

---

David Beard

Graduate Faculty Representative

## **Acknowledgements**

I would like to thank my committee for their time and effort in assisting my preparation of this thesis, ATI Wah Chang, Inc. for providing Zircaloy-4 samples for use in this research, the DOE Nuclear Energy University Programs for funding contributing to this research, and my family for their love and support.

# Table of Contents

|  |             |
|--|-------------|
| <b>Table of Figures</b> .....                | <b>viii</b> |
| <b>Abstract</b> .....                        | <b>xii</b>  |
| <b>1. Introduction</b> .....                 | <b>1</b>    |
| <b>2. Background</b> .....                   | <b>4</b>    |
| 2.1 Commercial Nuclear Reactors.....         | 4           |
| 2.2 Nuclear Fuels.....                       | 5           |
| 2.2.1 Ceramic Fuel Pellets .....             | 5           |
| 2.2.2 Construction .....                     | 5           |
| 2.2.3 Fuel Damage.....                       | 6           |
| 2.3 Monitoring .....                         | 7           |
| 2.3.1 Desirability.....                      | 7           |
| 2.3.2 Traditional Monitoring .....           | 8           |
| 2.3.3 Photonic Sensors .....                 | 9           |
| <b>3. Theory</b> .....                       | <b>13</b>   |
| 3.1 Photonic Theory .....                    | 13          |
| 3.2 Types of Photonic Crystal.....           | 14          |
| 3.2.1 1-Dimensional.....                     | 14          |
| 3.2.2 2-Dimensional.....                     | 15          |
| 3.2.3 3-Dimensional.....                     | 18          |
| 3.3 Photonic Thermo-Mechanical Sensors ..... | 19          |
| 3.3.1 Description .....                      | 19          |
| 3.3.2 Simulation.....                        | 20          |

|                                      |           |
|--------------------------------------|-----------|
| <b>4. Methods</b>                    | <b>22</b> |
| 4.1 Equipment                        | 22        |
| 4.1.1 Traditional Micro-fabrication  | 22        |
| 4.1.2 Focused Ion Beam Microscopes   | 23        |
| 4.1.2.1 FEI FIB800                   | 27        |
| 4.1.2.2 FEI DualBeam835              | 27        |
| 4.1.3 Sample/Substrate Preparation   | 28        |
| 4.1.4 Other Equipment                | 28        |
| 4.2 Production Methodology           | 29        |
| 4.2.1 Sample Preparation             | 29        |
| 4.2.2 Initial Lattice Selection      | 29        |
| 4.2.3 Pillars or Holes               | 30        |
| 4.2.4 Honeycomb Lattice Fabrication  | 30        |
| 4.2.5 Square Lattice                 | 35        |
| 4.2.6 Parallel vs. Serial            | 39        |
| 4.3 Quality Control                  | 45        |
| 4.3.1 Depth                          | 45        |
| 4.3.2 Re-deposition                  | 47        |
| 4.3.3 Beam Current                   | 48        |
| 4.3.4 Drift                          | 55        |
| 4.4 Photonic Crystal Arrays          | 58        |
| <b>5. Results and discussion</b>     | <b>62</b> |
| 5.1 Photonic Device Size and Quality | 62        |
| 5.1.1 Size                           | 62        |
| 5.1.2 Quality                        | 71        |
| 5.1.3 Optical Response               | 72        |

|       |                                       |           |
|-------|---------------------------------------|-----------|
| 5.2   | Future Work.....                      | 76        |
| 5.2.1 | Alternative Production Methods.....   | 76        |
| 5.2.2 | Photonic Crystal Error Tolerance..... | 78        |
|       | <b>Glossary .....</b>                 | <b>79</b> |
|       | <b>Works Cited .....</b>              | <b>81</b> |

## Table of Figures

|  |    |
|--|----|
| Figure 1 - Schematic view of PWR (pressurized water reactor) fuel assembly (Mitsubishi Nuclear Fuel) [5].....  | 6  |
| Figure 2 - Example of a Bragg grating fiber optic strain gauge [13].....   | 10 |
| Figure 3 - Conceptual rendering of photonic crystal sensors on single grains or across grain boundaries.....   | 11 |
| Figure 4 - A diagrammatic representation of a 1-D photonic crystal. The arrow represents the incident angle at which photonic effects occur. ....  | 15 |
| Figure 5 - A diagrammatic view of a 2-D photonic crystal. The arrows represent the incident angles at which photonic effects occur. ....   | 16 |
| Figure 6 - The three basic 2D lattices. (A) is a square lattice, (B) is a triangular lattice and (C) is a honeycomb lattice .....  | 17 |
| Figure 7 - A diagrammatic view of a 3-D photonic crystal. The arrows indicate the incident angles at which photonic effects occur. Unlike 1-D and 2-D crystals, photonic effect is observable from any angle. .... | 18 |
| Figure 8 - A photonic waveguide in silicon created with RIE [21].....  | 23 |
| Figure 9 - An FEI liquid metal ion source (LMIS).....  | 25 |
| Figure 10 – A diagram of a typical FIB column [24] .....   | 26 |
| Figure 11 - A test mill of a honeycomb lattice of holes using a parallel stream file mill on blank steel. ....   | 31 |
| Figure 12 - A test mill of a honeycomb lattice of holes using parallel mill script file on FIB smoothed steel. ....  | 33 |

|  |    |
|--|----|
| Figure 13 - A honeycomb lattice of holes milled using a milling script in parallel on un-smoothed steel.....   | 34 |
| Figure 14 - Honeycomb lattice of holes milled using a serial mode milling script. Note that holes are not connected, unlike parallel mode. Beam shift was used to try to align two patterns; overlap errors are clearly visible at the center of the image. .... | 35 |
| Figure 15 - A square lattice of holes.....   | 37 |
| Figure 16 - 45 degree tilt view of a square lattice of holes; note that the result more closely resembles a square lattice of pyramidal structures. ....   | 38 |
| Figure 17 - A square lattice of square rods in silicon milled in parallel.....   | 40 |
| Figure 18 - 45 degree tilt view of a square lattice of square rods on silicon milled in parallel. Note that the top of the pillars is significantly lower than the un-milled surface. This is an effect of parallel milling. ....                                | 41 |
| Figure 19 - Square lattice of square rods on silicon milled in parallel through a protective layer of platinum. ....   | 42 |
| Figure 20 - 45 degree cross section view of square lattice of square rods in silicon milled in parallel through a protective layer of platinum.....  | 43 |
| Figure 21 - A test of a square lattice of square rods on steel.....  | 44 |
| Figure 22 - 45 degree tilt view of a test of a square lattice of square rods on steel.....   | 45 |
| Figure 23 - A simple depth test on steel. Pattern III was milled to a depth setting of 300nm, pattern II was milled to a depth setting of 200nm and pattern I was milled to a depth setting of 100nm. All three show an optical return signal. ....              | 47 |
| Figure 24 - A square lattice of square rods on steel milled serially with re-mills at 12pA beam current.....   | 49 |

|  |    |
|--|----|
| Figure 25 - 45 degree tilt view of a square lattice of square rods on steel milled serially with re-mills at 12pA current.....                   | 50 |
| Figure 26 - A square lattice of square rods milled serially with re-mill at 70pA .....   | 51 |
| Figure 27 - 45 degree tilt view of a square lattice of square rods milled serially with re-mill at 70pA .....                                    | 52 |
| Figure 28 - 52 degree tilt view of a square lattice of square rods milled serially with re-mill at 500pA. ....                                   | 53 |
| Figure 29- A comparison of trenches milled with the multi-line method (left) and the box method (right) .....                                    | 54 |
| Figure 30 - A honeycomb lattice where drift has caused the structure, which should be square, to shift to the left over time. ....               | 56 |
| Figure 31 - A very large honeycomb lattice test where long term cyclic drift has caused the clearly visible wavy border between structures. .... | 57 |
| Figure 32 - An array of 16 photonic crystals imaged via optical microscope under oblique lighting .....  | 59 |
| Figure 33 - An array of 16 5 $\mu$ m photonic crystals on steel milled at 12pA .....   | 60 |
| Figure 34 – A large array of 4 arrays of 225 photonic crystals each milled on steel at 300pA.....  | 61 |
| Figure 35 - A large array of 4 arrays of 225 photonic crystals each milled on steel with a 300pA aperture.....                                   | 63 |
| Figure 36 - 45 degree tilt view of a section of a large array of photonic crystals each milled on steel with a 300pA aperture .....              | 64 |

|   |    |
|---|----|
| Figure 37 - A large array of 4 arrays of 225 photonic crystals each milled on steel at 100pA. The data bar has an error – total milling time was closer to 145 hours for this array ..... | 65 |
| Figure 38 – 45 degree tilt view of part of a large array of 4 arrays of 225 photonic crystals each milled on steel at 100pA.....  | 66 |
| Figure 39 - A large array of 4 arrays of 144 photonic crystals each milled on zircaloy-4 at 300pA.....  | 67 |
| Figure 40 - 45 degree tilt view of a section of a large array of photonic crystals milled on zircaloy-4 at 300pA.....   | 68 |
| Figure 41 - A large array of 4 arrays of 144 photonic crystals each milled on zircaloy-4 at 100pA.....  | 69 |
| Figure 42 - 45 degree tilt view of a section of a large array milled on zircaloy-4 at 100pA .....   | 70 |
| Figure 43 – Optical micrographs of an array of photonic crystals on UO <sub>2</sub> under top light (left) and varying oblique angles of optical illumination.....                        | 71 |
| Figure 44- A diagram showing the fiber layout of the reflection probe fiber bundle used for optical measurements .....  | 72 |
| Figure 45- A diagram defining the coordinate system used during optical measurements. The red line represents the fiber bundle reflection probe. ....                                     | 73 |
| Figure 46- Relative intensity graph of the response of a large array on steel, where phi was set to zero and theta varied. ....   | 74 |
| Figure 47- Color plot of the optical response of a large array on steel.....  | 75 |
| Figure 48 - An example of deep silicon etching using a Bosch process etch [27] .....  | 77 |

## **Abstract**

The LightGauge project seeks to develop photonic crystal sensor devices for use as a sensor network to be employed inside an operating nuclear power plant reactor core. Using finite difference frequency domain simulation, photonic crystals designs on steel, zircaloy, and  $\text{UO}_2$  (uranium dioxide) substrates were designed. Prototype photonic crystals were produced using FIB (focused ion beam) tools, and selected devices were optically interrogated. FIB production methodology was then optimized to reduce milling time and maintain crystal quality. Prototype results were promising, and results are expected to improve as future work investigates the use of additional fabrication techniques.

## **1. Introduction**

It is currently difficult, if not impossible, to directly monitor the state of nuclear fuel during reactor operation. Fuel behavior must thus be inferred based on pre and post-radiation examination as well as through a limited set of instruments in the reactor core and surrounding support structure. It is desirable to be able to monitor fuel behavior in-situ and in real time. In order to achieve this, a new sensor technology is required. Ideally, such a sensor would be able to detect changes in both temperature and strain state.

These sensors must be able to survive in an operating nuclear power reactor, which requires that they be resistant to radiation and able to withstand high pressure and high temperature. Additionally, they must not have a negative impact on reactor safety conditions or the reactor's operational performance and efficiency. The most significant source of radiation damage is the neutron flux; neutron irradiation can damage materials via a variety of mechanisms. Additionally, the sensor must be able to transmit data to a collection point outside the reactor's containment building. With electrical data transmission, gamma induced noise and signal deterioration become a significant problem. Due to the physical constraints in penetration through the reactor pressure vessel and reactor vessel head/base plate, large bundles of electrical wires that are prone to noise and deterioration are not desirable.

There exist temperature sensor technologies (thermocouples) that could survive the high temperature, typically 1800 to 2200 °C [1], and high pressure present inside a fuel pin. However, traditional temperature sensors cannot provide strain data. Nor are they small

enough to provide some of the localized data that would allow for increased understanding of fuel irradiation behavior via experimentation in a scientific setting, such as grain boundary behavior. The bi-metal material is also susceptible to activation from the intense neutron fields found in a reactor and this can lead to inaccurate measurements.

In order to quantify deformation, temperature and micro-strain data, photonic crystal sensor devices have been designed and constructed on various reactor materials. A photonic crystal device is a metamaterial – its behavior depends both on basic materials properties and its physical structure. It is the latter of these two that allows for photonic crystal devices to be used as sensors, because as the structure is deformed, the photonic behavior changes.

The LightGauge sensor is a photonic sensor which operates by observing the light output of a specially engineered photonic crystal. Broadband light is brought incident on the crystal at a pre-determined angle, and specific wavelengths and polarizations are returned at specific angles based on the geometry of the photonic device. As the structure is deformed, the return wavelength at a given angle changes, which will allow for the return wavelength to be measured and thus determine temperature (isotropic expansion) and other forces (non-isotropic strain). This is achieved by subjecting a photonic crystal of known geometry to temperature and stress that can be measured by an additional sensor, observing the optical return of the photonic device and correlating the two data sets.

This thesis embodies the first LightGauge sensor simulation, design and fabrication for nuclear applications. Photonic devices were designed using the MIT Photonic Bands (MPB) simulation package, and machined into the surface of common nuclear structural

and fuel materials including steel, zircaloy-4 and uranium dioxide using an FEI DualBeam835 or FEI FIB800 FIB tool. Where possible, completed devices were measured using a spectrophotometer. Based on physical appearance, as observed via FIB or SEM (scanning electron microscope) and wavelength returns vs. simulation, production methodology was optimized to balance device size, milling time and feature quality.

Production of photonic sensor devices was optimized to the maximum degree that appears possible using FIB tool based production. Initial tests of these photonic devices are promising. With the use of other, faster production processes, it should be possible to produce large and/or higher quality photonic devices for use as sensors.

## 2. Background

### 2.1 Commercial Nuclear Reactors

The majority of commercial nuclear reactors for electrical power generation are light water moderated reactors (LWRs) utilizing low enriched (up to 5% Uranium-235) uranium dioxide as fuel. The two most common variants of light water reactors are pressurized water reactors and boiling water reactors. In both cases, a fission chain reaction releases considerable quantities of energy. The majority of energy released during  $^{235}\text{U}$  fission is as kinetic energy of the fission products. The remainder of the energy is free neutrons, gamma rays and neutrinos.

Given the high density of  $\text{UO}_2$  and the large mass and high charge state of fission fragments, most of the fission energy ( $\sim 185$  MeV) is deposited in the ceramic fuel material as heat. The fuel is clad in a special alloy of zirconium and tin [2] known as zircaloy. The cladding material has a gas gap between the metallic cladding and ceramic fuel. The ceramic fuel itself heats up with a large thermal resistance present in the gas gap between the cladding and nuclear fuel. This produces a centerline temperature in the nuclear fuel pellet well in excess of  $1000$  °C. The pitch spacing between the fuel pins is small (less than 2 cm in most cases [3]) and each pin is surrounded by high temperature and high-pressure coolant water which contains chemical additives to prevent corrosion and assist in controlling the nuclear chain reaction. The high pressures, temperatures and radiation levels in a confined space, combined with the need to maintain a high flow rate, pose a formidable engineering challenge to measuring in-situ the stress and strain in the nuclear fuel pin cladding. The melting point of the fuel and the heat removal rate of the

reactor must be appropriately balanced to prevent the fuel from melting, colloquially known as a meltdown. The need to prevent fuel melting must also be balanced with the desirability of high operating temperatures, which increase thermodynamic efficiency.

## **2.2 Nuclear Fuels**

### **2.2.1 Ceramic Fuel Pellets**

Most commercial nuclear power plants use oxide fuel pellets, which may be  $\text{UO}_2$  or MOX (mixed oxide fuel which contains mostly uranium oxide and small admixtures of plutonium oxide). Oxide fuel pellets usually have very low thermal conductivity, as low as  $\sim 2.57 \text{ W/mK}$  at  $2000\text{K}$  [4], which presents a non-trivial thermal engineering problem. Typical oxide fuels in LWRs operate with a maximum fuel temperature of about  $1700\text{-}2300 \text{ }^\circ\text{C}$  [1], while  $\text{UO}_2$  has a melting point of  $\sim 3366.85 \text{ }^\circ\text{C}$  [4]. Due to its low thermal conductivity, the edge of the pellet will be significantly cooler than the center.

### **2.2.2 Construction**

Fuel pellets are typically stacked inside a fuel pin composed of stainless steel or zircaloy. A fuel pin is equipped with a spring to hold the pellets in place but still allow for expansion of the pellets without damaging the fuel pin. Once pins are loaded they are filled with helium gas and welded shut.

Fuel pins are combined with empty tubes for sensors, poison rods, blank spaces for control elements, flow channels and a physical support structure to form a fuel assembly. Typical light water reactor fuel assemblies may have between 64 and 300 pins [3]. A drawing of a typical fuel element can be seen in Figure 1. Multiple fuel assemblies make

up the active region of a reactor core, and a typical LWR may have between 193 and 732 assemblies [1].

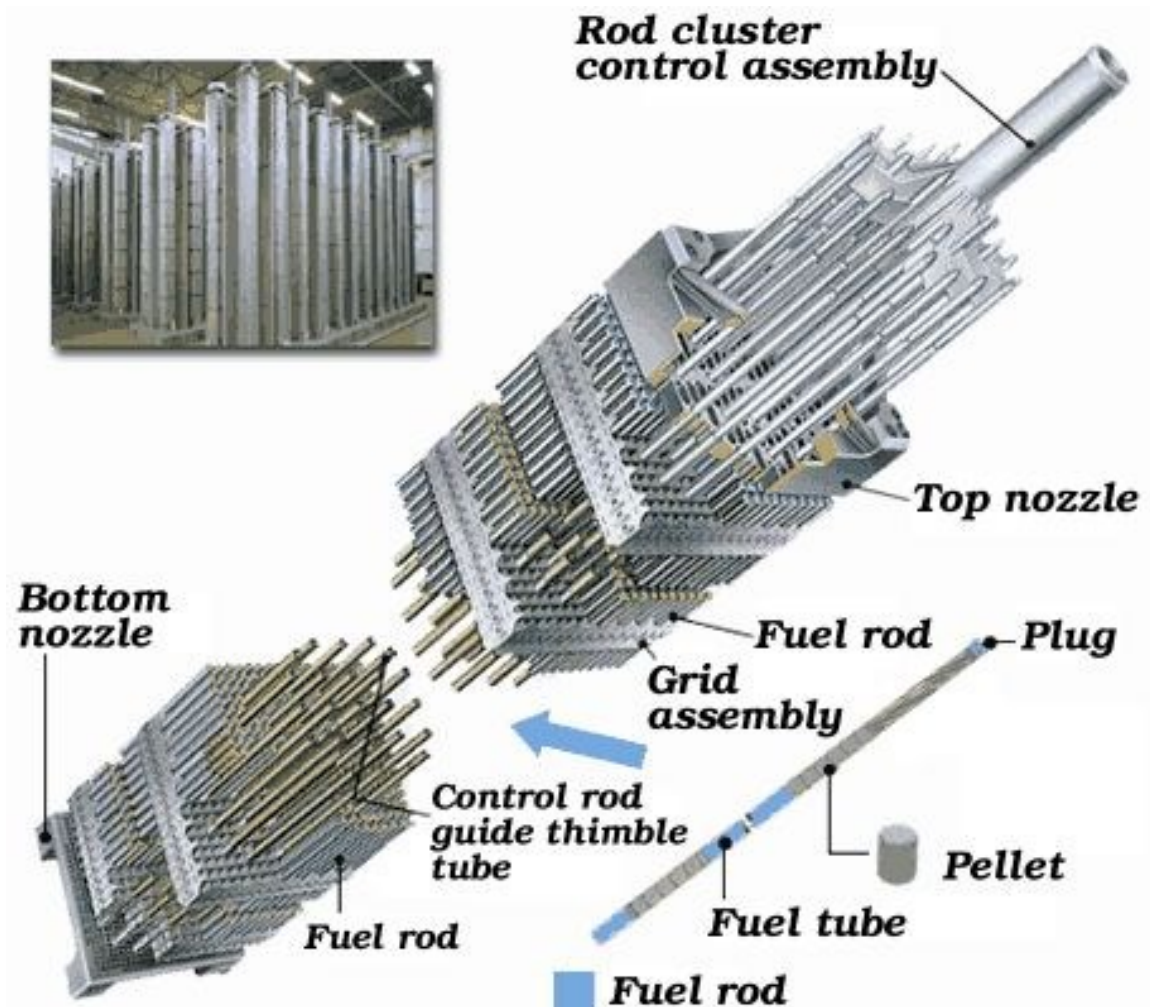


*Figure 1 - Schematic view of PWR (pressurized water reactor) fuel assembly (Mitsubishi Nuclear Fuel) [5]*

### 2.2.3 Fuel Damage

During operation, there are a variety of different mechanisms by which fuel can become damaged. Damage can consist of damage to the cladding material including cladding rupture, corrosion, hot spot formation, swelling and weld breakdown. Fuel pellet damage

can also occur, including macroscopic effects of damage, such as swelling and cracking, and this damage may be observable with appropriately placed and designed LightGauge sensors.

## **2.3 Monitoring**

### **2.3.1 Desirability**

In order to improve fuel performance it is desirable to quantify fuel pellet and fuel rod behavior when irradiated. An improved understanding of fuel behavior would assist in the improvement of the design and manufacture of fuel, leading to more efficient and safer reactor systems.

Since high operating temperatures are thermodynamically more efficient, it is logical to run the reactor as hot as is possible within the bounds of prudence and the reactor's design basis accident conditions. Thermal measurement instrumentation typically consists of thermocouples for measuring the coolant outlet temperature. With actual temperature data from the fuel pellets' surface, margins of safety to account for the approximate nature of extrapolating fuel pellet temperatures could be reduced or eliminated, allowing the reactor to safely run at higher temperatures.

The application of monitoring systems for the cladding goes hand in hand with that of fuel; a more closely monitored system can be safely run closer to its theoretical limits. For example, a sensor on the exterior cladding of a fuel pin could give early warning that a particular pin is experiencing problematic swelling, threading, hot spot formation or is approaching dangerous temperatures.

### **2.3.2 Traditional Monitoring**

Current understanding of fuel pellet behavior is largely based on post-irradiation examination. Conditions inside a typical commercial nuclear plant make the deployment of traditional sensors for in-situ fuel monitoring infeasible. Reactor cores are a high temperature, high-radiation (neutron and gamma) and potentially high-pressure environment. These are difficult conditions for existing sensor technologies.

Traditional monitoring systems for reactors typically rely on a number of different sensors to capture data. Thermocouples are used to monitor inlet and outlet coolant temperatures and flux wires or fission chambers can be used to monitor flux. The most robust thermocouples can operate up to about 2300 °C, which would be sufficient to measure the surface temperature of a fuel pellet in most commercial nuclear reactors [6]. However, the gamma flux in a power reactor is sufficient to cause significant electrical noise in any electrical conductors running through the core, which makes the use of electrical signals problematic. Thermocouples typically use mV range signals [7] and require low noise; gamma rays can induce sufficient noise to make these signals unusable. Cable runs may also be too long to effectively transmit such a low voltage signal.

This is not to say that the use of electrical signals is impossible; in-core flux measuring devices make use of electrical signals, and use digital signal transmission and specialized amplifiers to alleviate gamma induced noise [8]. Of course, the electronics necessary to convert an analog to digital signal are unlikely to have a long lifetime in the neutron flux typical to nuclear power reactors.

Traditional high temperature strain gauges also exist, but they are typically only functional up to around 1100 °C. [9] [10] [11] While the temperature alone might not be an issue for this style of sensors, the radiation flux remains an impediment to their use. Like thermocouples, strain gauges rely on electrical signals for data transmission with all of the challenges that that entails in a strong gamma flux.

### **2.3.3 Photonic Sensors**

By using a sensor entirely based on photonic interactions, a device can be designed which is capable of operating in the aforementioned high radiation, high temperature and high-pressure environment. Optical data transmission at certain wavelengths is immune to gamma-induced noise. Signal loss via radiation induced attenuation (RIA) in traditional fiber optic cables is a well-known problem, but there are photonic fiber optic cables in which the transmission medium is air rather than glass that have very low RIA compared to conventional fiber optics [12]. A photonic device should survive any temperature or pressure that does not destroy the substrate, and neutron damage is unlikely to cause failure of the photonic device, as small, localized changes in structure will not disable the entire sensor.

There is significant existing work on the use of Bragg Fiber grating fiber optic devices as stress and temperature sensors [13]. These are effectively one dimensional photonic crystals located at the center of a fiber optic cable. The structure acts as a dielectric mirror, reflecting light at the Bragg wavelength.

As the fiber is strained, the spacing of the dielectric layers changes, which in turn affects the Bragg wavelength. Strain can thus be measured by observing the change in the

transmission spectra of the fiber. [13] As it is entirely photonic in nature, this type of device overcomes many of the problems associated with more traditional sensor technologies. A drawing of such a device can be seen in Figure 2.

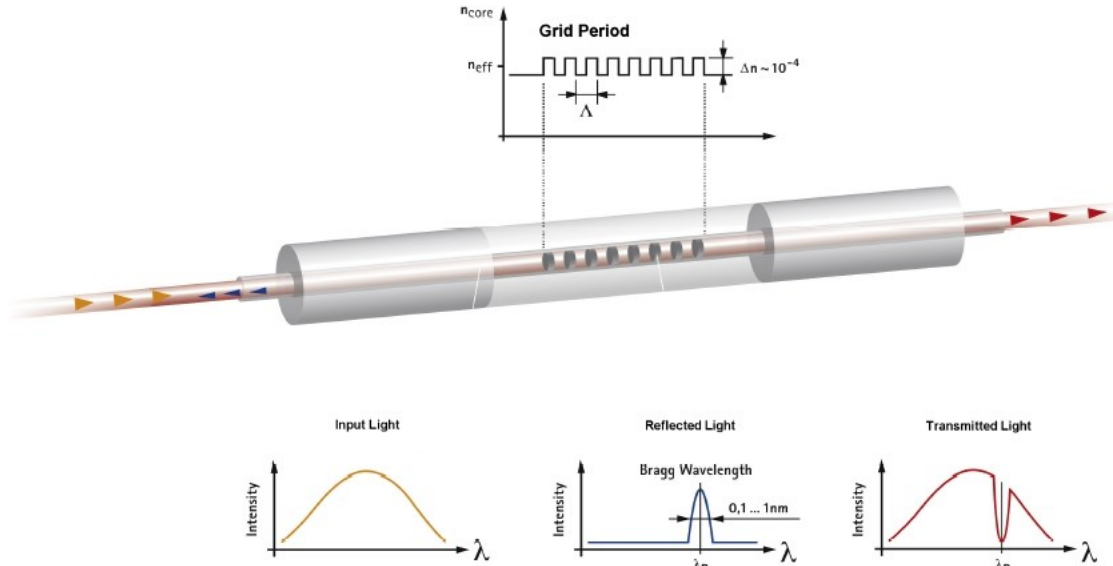


Figure 1. Principle of a Bragg grating measurement in an optical fiber

*Figure 2 - Example of a Bragg grating fiber optic strain gauge [13]*

The LightGauge project proposes an evolution of the same concept. Rather than using a Bragg grating or Bragg mirror, a 2D photonic crystal will be used. This will provide additional axes of sensitivity. LightGauge sensors will also be written directly onto the material of interest, rather than requiring an external sensor to be affixed. This is a macro-scale application potentially useful for in-core monitoring during operation.

In addition to all of the benefits of a solid state optical sensor system, this type of sensor can be produced at the micro-scale. For example, a small photonic crystal placed across a grain boundary on the exterior of a fuel pellet (a conceptual rendering of which can be seen in Figure 3) could allow for grain and grain boundary behavior to be monitored in

real time – a function for which there is no equivalent traditional sensor. Given the necessity for such a photonic crystal to be very small (and thus more difficult to interrogate), this would more likely be a purely scientific application.

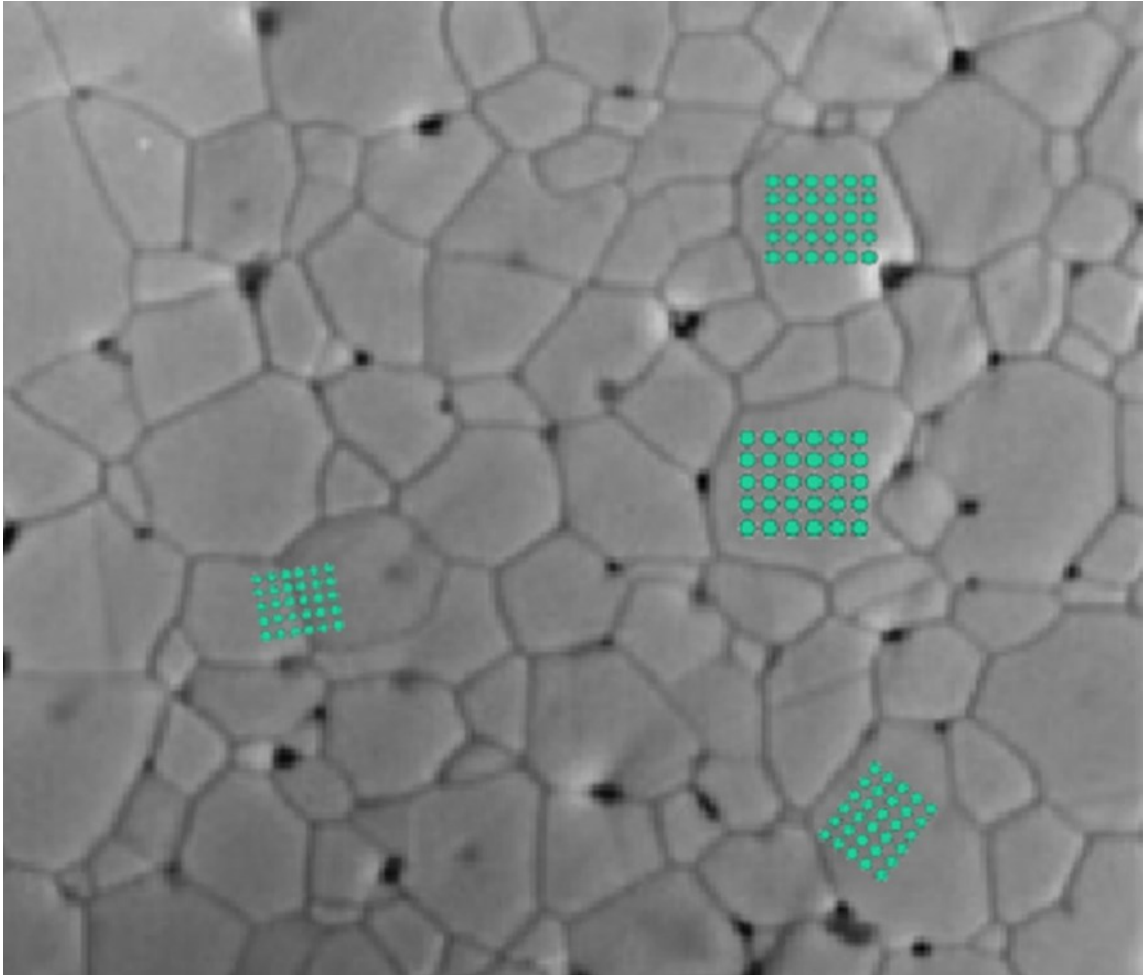


*Figure 3 - Conceptual rendering of photonic crystal sensors on single grains or across grain boundaries*

With a network of photonic sensors, temperature and multi-axis strain could be monitored at a large number of locations inside a fuel pin in order to build a more comprehensive history of fuel pellet behavior during irradiation, and provide valuable real-time data for optimizing reactor operations.

Such sensors can be directly written onto any material possessing a sufficiently high dielectric constant, including iron (and thus steel), uranium dioxide and zirconia (refractive index of  $ZrO_2$  used for zircaloy simulations), all of which are materials of particular interest to the nuclear engineering field. As simple temperature sensors, thin films of an appropriate material, perhaps higher-index materials such as titanium oxide or other high temperature high refractive index material, could host the actual sensor(s) and then be affixed to the object of interest.

### **3. Theory**

#### **3.1 Photonic Theory**

Photonic devices are carefully designed meta-material structures that control the flow of light. A functioning photonic device must be composed of two or more regions of differing dielectric constant. Generally speaking, a greater difference in dielectric constant makes a better photonic device. Many different useful photonic devices, such as monochromatic filters, waveguides, concentrators and cloaking devices can be created. Joannopoulos' text [14] provides an excellent overview of photonic theory should additional information be desired.

It is important to note that the assumptions used for this project are primarily targeted towards a very specific class of materials – those without significant absorption and which have very low conductivity. Unfortunately, this set of materials does not include many metals. As the goal of this thesis project is heavily oriented towards production optimization as opposed to simulation, these assumptions were left intact in order to make practical the use of pre-existing simulation packages created around these assumptions. Once fabrication techniques are perfected, additional work on simulating the response of devices produced on materials with non-zero absorption and non-unity relative permeability could be conducted and designs adjusted appropriately.

Given these assumptions, there exist software packages capable of simulating the 2D photonic devices that were initially targeted for production. The software package used for this thesis, MPB [15], uses a frequency domain solver. This software returns the bands (allowed modes) and band gaps (forbidden modes) for a given crystal.

The fundamental property of photonic crystals that makes them so useful is the band gap. Based on the geometry and materials, certain frequency modes cannot exist in a photonic device. The ability to control the frequency of these band gaps by manipulating the geometry of the photonic crystal is a powerful tool to control the propagation of light in ways that have not previously been possible.

## **3.2 Types of Photonic Crystal**

### **3.2.1 1-Dimensional**

The simplest form of the photonic crystal is simply a stack of planes with differing dielectric constants. A drawing of such a stack can be seen in Figure 4. These are often referred to as Bragg mirrors, and have been known since 1888. They were initially investigated by Professor Stokes and Lord Rayleigh [16]. Bragg mirrors are commonly used in optics when very high reflectivity or very specific reflective wavelengths are desired. There is ongoing work on the use of specialized Bragg grating fibers as thermo-mechanical sensors. The first fiber Bragg grating was produced in 1978 by K.O. Hill et. al. [17].

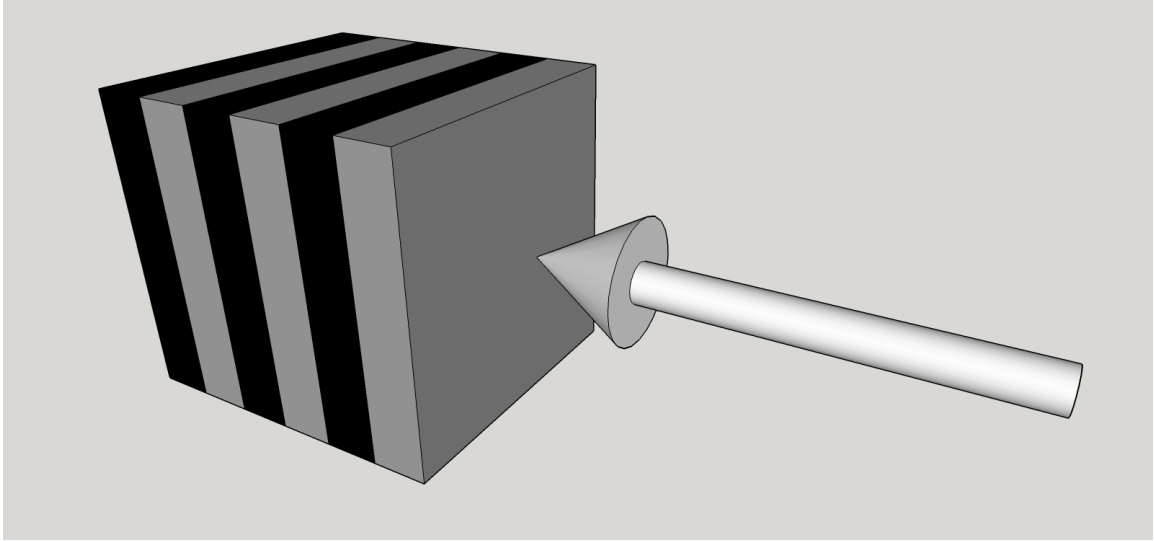


*Figure 4 - A diagrammatic representation of a 1-D photonic crystal. The arrow represents the incident angle at which photonic effects occur.*

### **3.2.2 2-Dimensional**

The next step up in complexity, two-dimensional photonic crystals, vary in two dimensions, and are idealized as being infinite in the third. Figure 5 is a drawing of a 2-D photonic crystal.

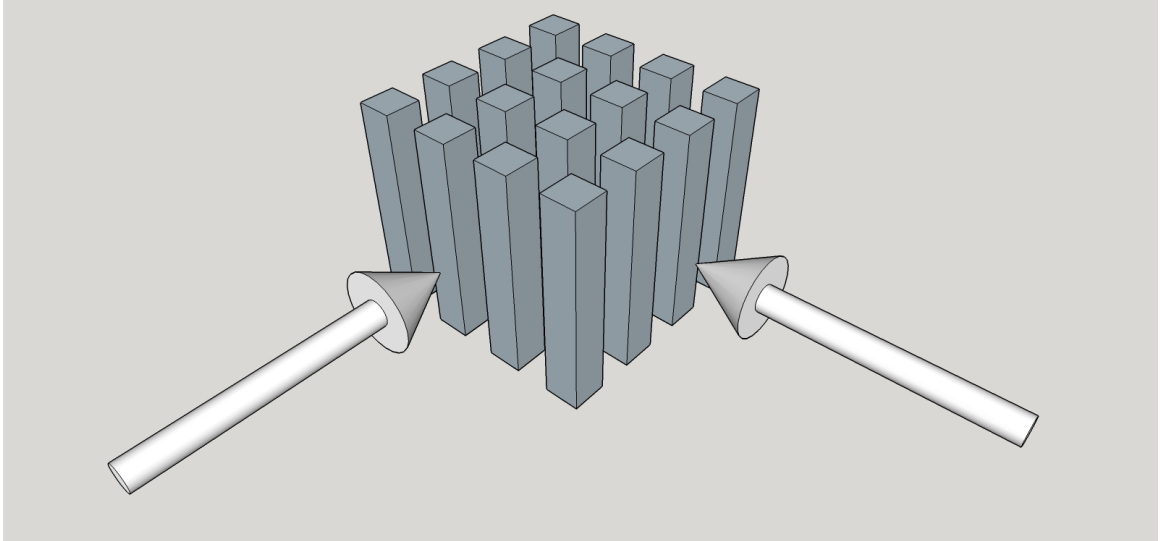


*Figure 5 - A diagrammatic view of a 2-D photonic crystal. The arrows represent the incident angles at which photonic effects occur.*

2-D crystals can have significantly more complex behaviors than 1-D devices. For regular and repeating ordered structures, 2-D crystals are most easily defined by specifying a lattice type and the geometry of a single unit cell. A unit cell is the smallest unit of unique geometry that a regular repeating structure can be broken into. For example, if one imagines a row of identical objects, such as circle, laid out in a line, then the unit cell encloses a circle and one half of the gap between each circle. Thus, the line of circles can be defined by putting multiple unit cells adjacent to each other. The most commonly used lattices are rectangular, triangular and honeycomb (a modified triangular lattice), and examples of all three can be seen in Figure 6.

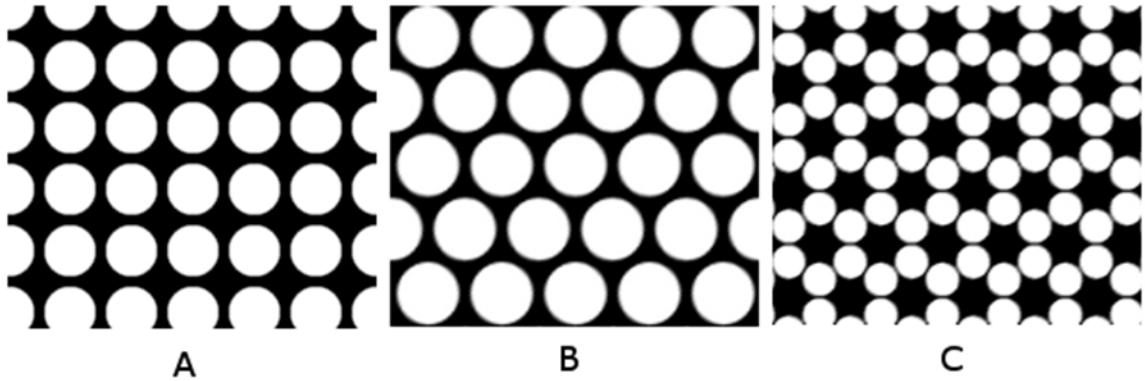


*Figure 6 - The three basic 2D lattices. (A) is a square lattice, (B) is a triangular lattice and (C) is a honeycomb lattice*

As one might expect, different lattices will have different photonic behaviors. For the square lattice, a column-based lattice will have smaller TE (transverse electric) band gaps, while a hole based lattice will have smaller TM (transverse magnetic) gaps.

Generally, lattices composed of connected dielectric areas (often referred to as veins) will have TE gaps, while lattices of discrete dielectric zones (columns) will have TM gaps.

[14]

A triangular lattice can have both isolated areas of high dielectric and connective dielectric veins; for example, if the columns are a low dielectric material (such as air) and the remaining material is high dielectric, the triangular lattice, when the column radius is high, has isolated areas of high dielectric (the spaces in between three adjacent columns) and veins of high dielectric between each “node”. Due to this geometry, it is possible to achieve a complete band gap (an overlapping band gap in both TE and TM polarization) with an appropriately designed triangular lattice photonic crystal.

A honeycomb lattice is a triangular lattice where the unit cell contains two columns rather than just one. The honeycomb lattice can produce larger complete band gaps and be simpler to fabricate than a triangular lattice, because it possess both isolated dielectric regions and veins without requiring very small feature size.

### 3.2.3 3-Dimensional

The most complex type of geometry, 3-dimensional crystals can be highly customized to achieve a specific desired behavior. These crystals have varying geometry in all three dimensions. A drawing of a 3-D photonic crystal can be seen below in Figure 7.

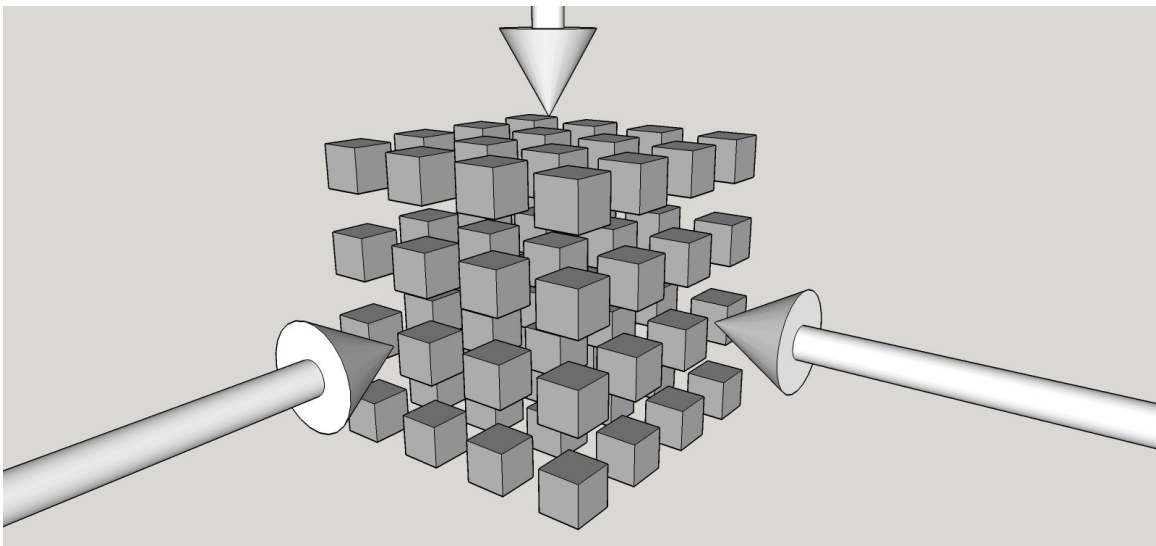


*Figure 7 - A diagrammatic view of a 3-D photonic crystal. The arrows indicate the incident angles at which photonic effects occur. Unlike 1-D and 2-D crystals, photonic effect is observable from any angle.*

In reality, all physical devices are 3-D crystals, though they can often be satisfactorily approximated as one or two dimensional devices for ease of calculation and simulation. For the purposes of this stage of the LightGauge project, it is not necessary to examine

the various possible structures and behaviors of 3-D photonic crystals. However, the structures that were actually fabricated are 3-D in nature, though the design is only regular and repeating in two dimensions. When viewed out of plane, they could be termed limited three-dimensional structures. The design is a two dimensional lattice with non-uniformity in the third dimension.

### **3.3 Photonic Thermo-Mechanical Sensors**

#### **3.3.1 Description**

For use as a thermo-mechanical sensor, a photonic device must be designed which has one or more relatively narrow band gaps. Practically speaking such a device acts somewhat like a color-specific mirror; a white light input will yield a number of colored outputs. On its own, this effect would not be particularly useful as a stress sensor.

Fortunately, both the construction material and the physical shape control the behavior of a photonic device. Thus, a change in the shape of the device (i.e. strain) will change the light output of the device. The output wavelength can then be correlated to the amount of strain and a photonic device can be used in this manner as a strain sensor. The smaller the band gap, the greater the detection resolution of the sensor will be. Multiple gaps are desired so that in addition to gathering data based on the change of return wavelength, the presence or absence of multiple expected returns can also be used to calculate the strain – a device can be designed where sufficient deformation will cause some of the band gaps to cease to exist while others merely shift wavelength.

Depending on the design of the photonic device, a change in one axis should be easily distinguishable from a change in both axes, as the crystal will then have a different

geometry per axis. This should lead to dissimilar return wavelength for light from each axis. Thus, since thermal expansion is isotropic, such a photonic device can distinguish between thermal expansion and mechanical strain. The use of photonic crystals as thermal sensors has been previously demonstrated as part of the LightGauge project.

### **3.3.2 Simulation**

Simulations of photonic devices were conducted with the freely available MIT Photonic Bands package [15]. MPB uses the finite difference, frequency domain (FDFD) modeling paradigm. It is simplest to use when the photonic structure of interest is both regular and repeating. The photonic devices produced in the course of this work fit both of these definitions, although they are not infinite in the z direction as is assumed in MPB simulations. However, MPB provided a relatively simple starting point. More complex calculations will be performed in future work with a related package known as MEEP (MIT electromagnetic equation propagation). MEEP uses the finite difference, time domain modeling (FDTD) paradigm, and generally speaking is useful for performing simulation of more complex systems, such as three dimensional and/or non-regular and non-repeating structures.

MPB simulations require only a few simple parameters since this particular software package is designed to simulate repeating regular structures. It takes as inputs the lattice constant (the spacing between unit cells), the geometry of the unit cell and the materials composing the unit cell. The material property of concern is the dielectric constant, the real portion of which is proportional to the index of refraction. The dielectric constant,  $\epsilon$ , is composed of a real and imaginary part. For work on photonic devices that have real

and frequency independent dielectric constants, this is not an issue. However, metals often have frequency dependent and occasionally imaginary or negative dielectric constants. For the initial portion of the LightGauge project, absorption was ignored, which allowed for the assumption of a real, positive dielectric constant for the materials under consideration. These data are readily available [18] [19] [20]. The absorption/reflectivity issue is one of the reasons that most previous work on metallic photonic crystals has been performed in the microwave regime, where most metals are good reflectors.

## **4. Methods**

### **4.1 Equipment**

#### **4.1.1 Traditional Micro-fabrication**

The majority of existing research on optical regime photonic devices has been performed on materials compatible with common semi-conductor fabrication processes. Most of the processes used to produce modern semi-conductor devices use some variant of lithography to produce masking layers as needed for selective deposition or material removal. For example, a layer of photoresist might be laid down onto the substrate, exposed to UV through a mask or exposed with an electron beam. The developed resist is then removed, leaving the desired mask. Material is then either deposited (via various methods, e.g. evaporative coating) or removed (e.g. RIE, reactive ion etching.)

When working in materials for which these processes are very mature, principally silicon and other semiconductors, large structures of excellent quality can be produced. An example of photonic structure on silicon, produced with an RIE process, can be seen in Figure 8.

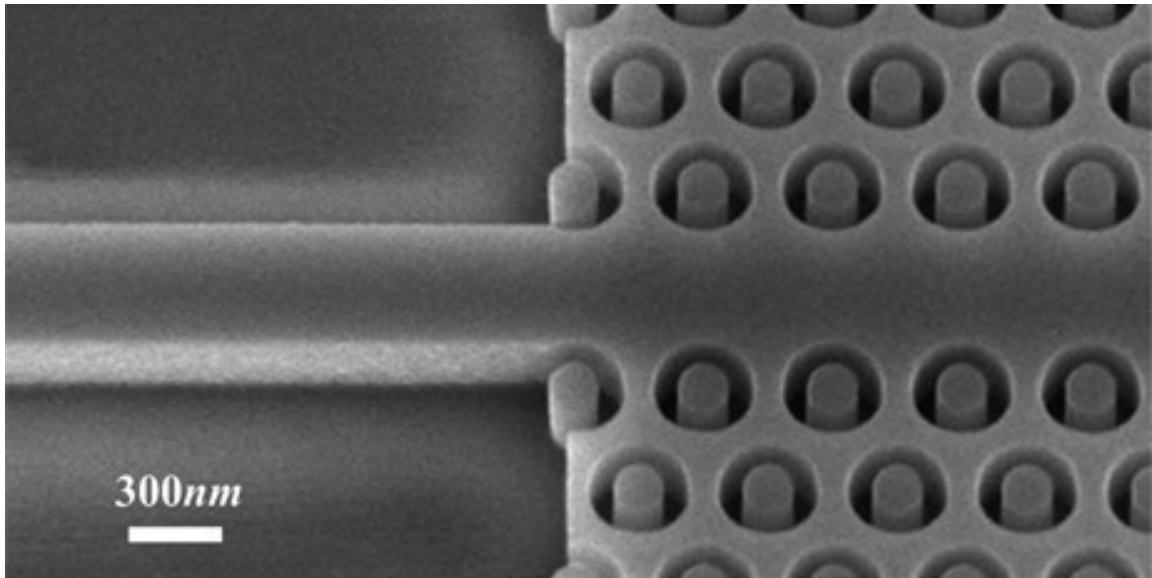


*Figure 8 - A photonic waveguide in silicon created with RIE [21]*

Unfortunately, an analogous suite of tools for micro and nanofabrication has not been developed for most metallic materials. There has been some work in micro and nanofabrication of metallic structures where the metals in question are useful to the semiconductor industry; for materials like steel and Zircaloy, which are not used in semiconductors, little to no effort has been made to develop high-volume nanofabrication techniques. For this reason, it was necessary to use a tool that allows for patterning on the materials of interest and with which techniques could be iterated on relatively quickly: the focused ion beam microscope.

#### **4.1.2 Focused Ion Beam Microscopes**

The basic concept of a focused ion beam microscope is relatively simple. Ions are generated by an ion source and accelerated and steered towards the imaging target. Interactions with the target produce secondary electrons and ions, which are then

collected and measured. FIB microscopes are scanning, surface imaging systems, very similar in operation to scanning electron microscopes.

Unlike a standard optical microscope or transmission electron microscope, where the entire image is formed simultaneously, a scanning microscope focuses the beam (whether it is light, electron, ion, etc.) on a single spot. The intensity of the return from that spot is recorded, and the beam is then moved to the next spot. By scanning the beam very quickly, an image of the entire viewing area can be created in a fraction of a second.

Most FIB microscopes use a liquid metal ion source (LMIS), typically gallium. There are a variety of different designs, but all are variants of a larger gallium reservoir feeding some sort of narrow tip. Gallium has a low melting point, 29.7646 °C [22]. A very sharp tip is necessary for proper ion emission, and this tip is formed by electrically heating the ion source in the presence of an electric field; this heating is carried out in the microscope and is a standard operating procedure that must be performed periodically. Once a tip is generated, a small current keeps it liquid and ions are stripped via electric field and accelerated by a large voltage potential. Figure 9 is a photograph of an FEI LMIS like that in the FIB tools used during this research.



*Figure 9 - An FEI liquid metal ion source (LMIS). There is a large helical wire wrapped around the gallium reservoir for heating with a single wire at the top for the gallium to flow along or through to form the tip. [23]*

Similar to electron microscopes, the lenses on a focused ion beam tool can be either magnetic or electrostatic, as both forces act on charged particles (in this case gallium ions). A series of lenses condense and focus the ion beam, and one or more multi-pole magnets (often quadrupoles or octopoles) are used to steer the beam. Figure 10 is a diagram representing a typical FIB column.

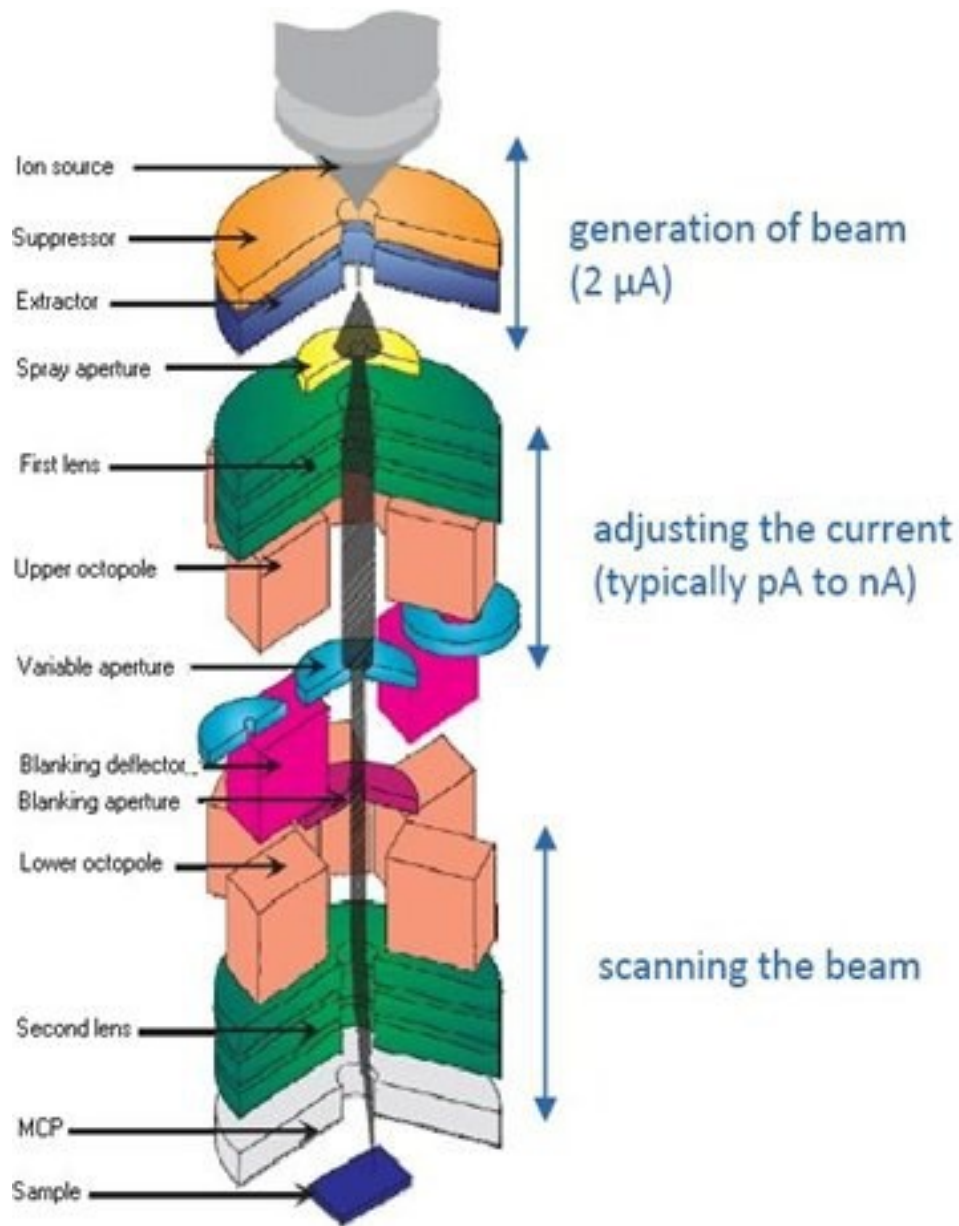


*Figure 10 – A diagram of a typical FIB column [24]*

All of the photonic devices created for this project were produced using one of two focused ion beam tools. In this case, both instruments were produced by FEI, Inc. The first tool is an FEI FIB800 pre-lens column instrument, and the second is an FEI

DualBeam835, equipped with a magnum lens ion column. Both of these instruments use a gallium liquid metal ion source to provide gallium ions.

The ion columns on these two tools are very similar; both run at up to 30kV accelerating voltage and were run at 2.2 uA emission current. The selection of available aperture sizes used for controlling beam current is comparable but not identical. The software for each instrument is also very similar, and as a consequence milling scripts are easily shared between these instruments. Of particular note are the different column lenses; the magnum column on the DualBeam allows for more beam-current to be focused on a smaller spot. Practically speaking, this means that it can achieve faster milling speeds for a given minimum desired feature size.

#### **4.1.2.1 FEI FIB800**

The FEI FIB800 is a pre-lens column, load-lock equipped, 30kV, gallium liquid metal ion source tool. It has an 8 inch platter, in this case designed to accommodate a number of standard 1/8" stubs simultaneously. This tool is equipped with two GIS (gas injection system) needles, which were configured for platinum deposition and IEE (insulator enhanced etch) for increased material removal on insulating materials (primarily silicon). The stage is fully motorized and automated, capable of 0-55 degree tilt and travel across the entire 8" platter.

#### **4.1.2.2 FEI DualBeam835**

The FEI DualBeam835 is, as the name suggests, a dual beam system. It has both a 30kV magnum ion column as well as a 30kV FEG (field emission gun) electron column. This provides considerable versatility. The DualBeam also uses a load lock and an 8 inch

platter, although the DualBeam platter is configured as a wafer holder rather than a multi-stub holder. The DualBeam is equipped with an OmniProbe needle (for physical micromanipulations), an IXRF EDS (x-ray energy dispersive spectroscopy) system, and two GIS needles that were configured for platinum and tungsten deposition. The stage is fully motorized and automated, with the same 0-55 degree tilt range as the FIB800.

#### **4.1.3 Sample/Substrate Preparation**

Steel and zircaloy samples were produced using standard machining techniques. Where possible, a Buehler Vanguard automated polisher was used to polish samples. The smallest abrasive particle size used with the auto-polisher was 0.05  $\mu\text{m}$ . Samples were hand polished when necessary.

#### **4.1.4 Other Equipment**

For optical interrogation of photonic devices, several custom designed apparatuses were used. One unit began life as a Nikon "Optiphot" high power optical microscope. The beam path optics were largely maintained, while the support structure was completely redesigned. A Meiji long travel pole-mount focus block was attached to a custom designed microscope stand. The original lenses were removed and replaced with long working distance, infinity corrected lenses. This allowed for increased flexibility in terms of lighting and sample geometry; in particular the approximately 8mm working distance of the 100x lens allows for highly oblique side-lighting at varying angles while maintaining sufficient magnification for the interrogation of smaller photonic devices (down to 5  $\mu\text{m}$  square.)

The eyepieces on the microscope can be replaced with a camera or fiber optic adapter as desired. The fiber optic was then fed into the input of a spectrophotometer for the purposes of measuring the return wavelengths of photonic devices.

Another testing rig was designed for the interrogation of photonic crystals or photonic crystal arrays of sufficient size that no significant magnification was needed. This device places the photonic crystal at the eucentric point of a number of different goniometers and rotation stages such that the sample can be illuminated and observed from a wide range of angles.

## **4.2 Production Methodology**

### **4.2.1 Sample Preparation**

Sample preparation was very similar to standard metallurgical sample preparation. In order to fit in the FIBs, all samples must be less than approximately 1/8 of an inch thick. A completely smooth surface is not required for the production of a photonic device, but is very beneficial for both milling consistency and especially ease of optical interrogation. A mirror finish surface minimizes direct reflections of the broadband light source used for interrogation when collecting data on a photonic device's optical response. This being the case, where possible all samples were polished using an automated polishing system employing abrasive slurry down to 0.05 $\mu$ m particle size.

### **4.2.2 Initial Lattice Selection**

As was discussed in the photonic theory section, there are three main types of 2D photonic crystal lattices: square, triangular and honeycomb. The honeycomb lattice is the

most desirable because it is most likely to have overlapping TE and TM band gaps. This is called a total band gap, and the presence of a total band gap is why the honeycomb lattice was chosen as the ideal structure.

### **4.2.3 Pillars or Holes**

All lattices can be composed of either voids or material, i.e. holes or pillars. The choice between them controls the prevalence of TE or TM gaps based on the lattice. The milling script included with the FIB tool is simple to use, but also somewhat limited. There are only a small number of basic shapes built in, namely rectangles, circles, annuli, lines and tetragons. Notably, there is no included method to do negative patterns, e.g. remove all of the material except a shape, such as producing a round pillar. A method to produce round pillars by milling annuli and multiple tetragons was eventually developed, but was an unacceptably large addition to total milling time. For this reason, it was decided that for lattices of round features, only holes would be used.

### **4.2.4 Honeycomb Lattice Fabrication**

It was initially thought that the easiest way to fabricate a honeycomb lattice would be to use a program included with the FIB tool that converts bitmap images to stream files. A stream file controls the motion of the beam over a large area by specifying mill points and beam dwell time. Stream files are particularly useful for milling complex shapes that cannot be easily reproduced with basic combinatorial geometry, such as curves or line art.

When using the bitmap to stream file conversion, there is no difference in difficulty between holes or pillars, but simulations showed that a honeycomb of holes would give

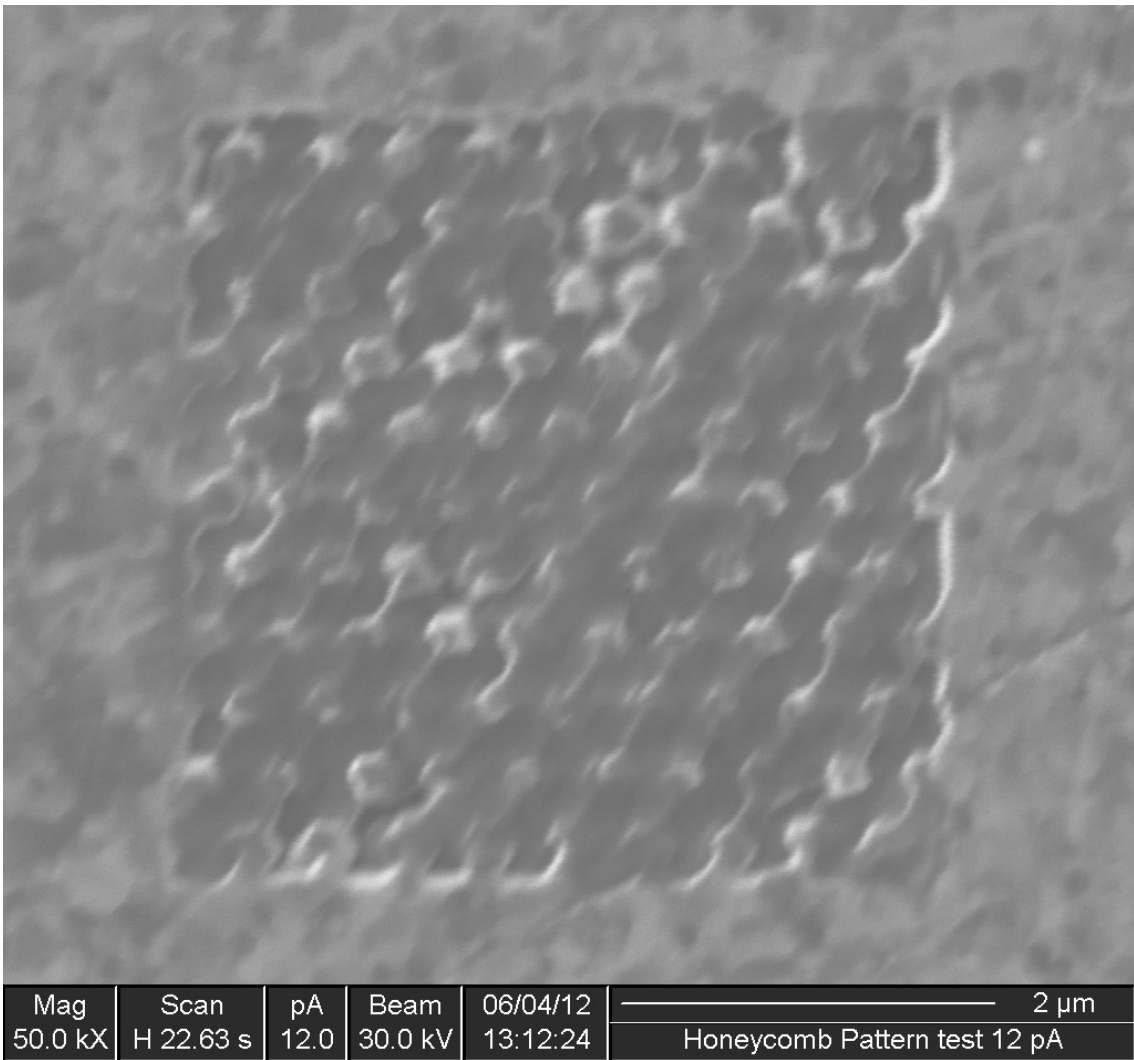


*Figure 11 - A test mill of a honeycomb lattice of holes using a parallel stream file mill on blank steel.*

better results in the materials of interest. When using the stream file method, it was quickly realized that there was undesirable erosion on non-milled portions of the pattern, as can be seen in Figure 11.

The erosion is a result of the beam constantly remaining on; the stream file specifies a large number of points and dwell time at each point, but does not turn off the beam. The FIB800 (and DualBeam835) used for this project did not have a high-speed beam blanker installed. A high-speed beam blanker is basically a mechanical shutter that can very quickly open and close to block the beam. The presence of a high speed beam blanker would allow for the beam to be blocked while it moves to the next milling point, thus eliminating undesired material removal. Unfortunately, high-speed beam blankers for these systems are notoriously maintenance intensive, and generally considered more trouble than they are worth.

The next method attempted to mill honeycomb lattices was to write a script that would lay out an appropriately spaced row of holes from the lattice. This was first attempted in parallel mode (all patterns are milled simultaneously), as it was thought that this would result in reduced undesired material removal when compared to the stream file method. Results with this method can be seen in Figure 12 and Figure 13. Undesired material removal was still considered to be unacceptably high, here manifesting as some holes being connected by trenches, leading to the attempted use of serial milling.

Serial milling differs from parallel mode milling in that each pattern is milled to completion before the beam moves to the next pattern; in this case, each circle is milled to its complete depth before the next circle begins to be milled. This milling method effectively eliminated undesired material removal; however, it appeared that material from milling was re-depositing into previously milled holes. This was partially mitigated by adding a re-mill step, an important development that would see heavy use later.

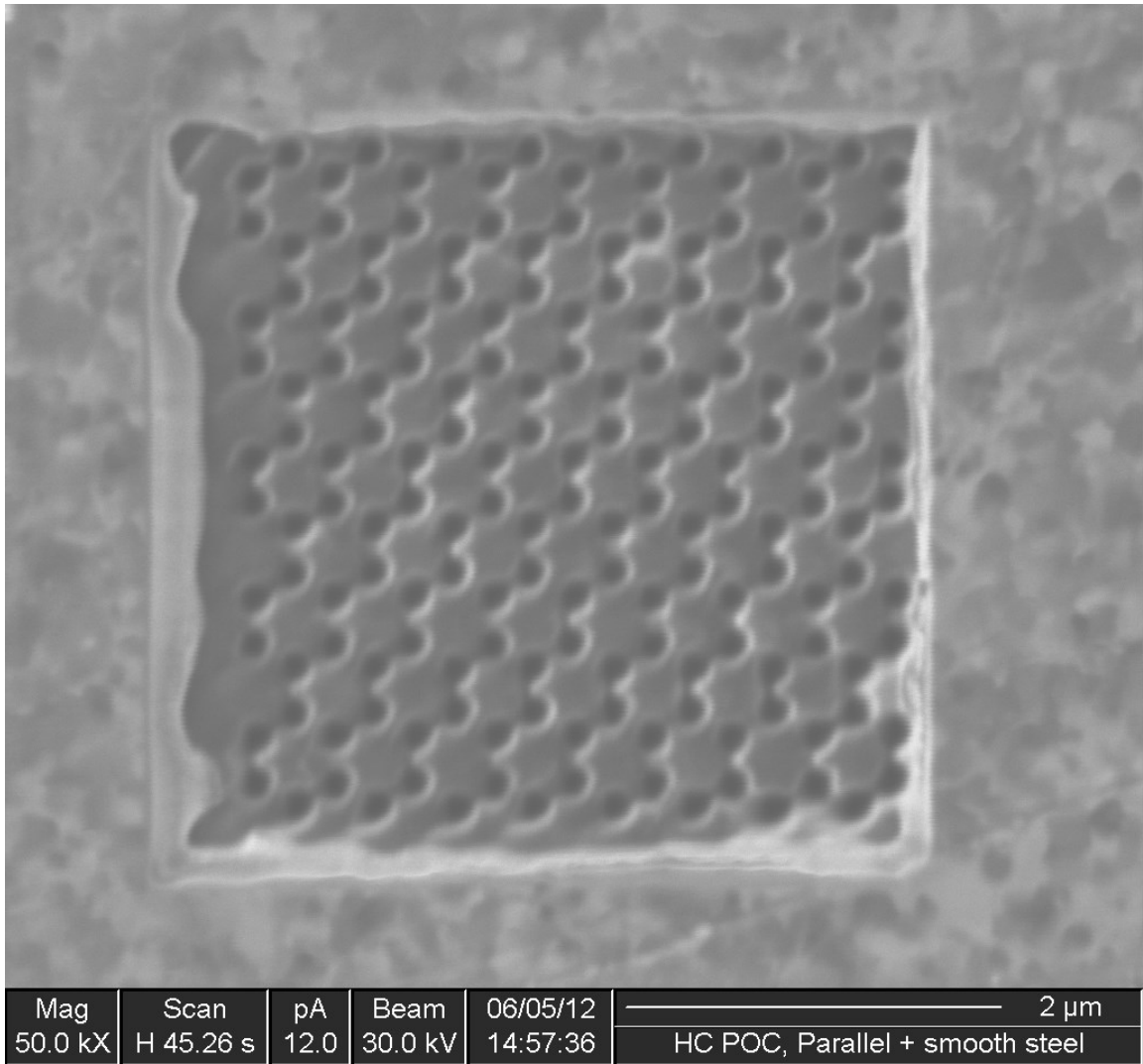


*Figure 12 - A test mill of a honeycomb lattice of holes using parallel mill script file on FIB smoothed steel.*

Ultimately, the high complexity of a honeycomb lattice proved a significant impediment to the production of large honeycomb lattices because of drift issues. Milling large areas requires precise movement with sub-micron resolution and sub-micron shift as a function of time. The shift over time is known as drift. Drift can have multiple causes (such as changes in lens temperature or sample charging), but stage drift, where the stage

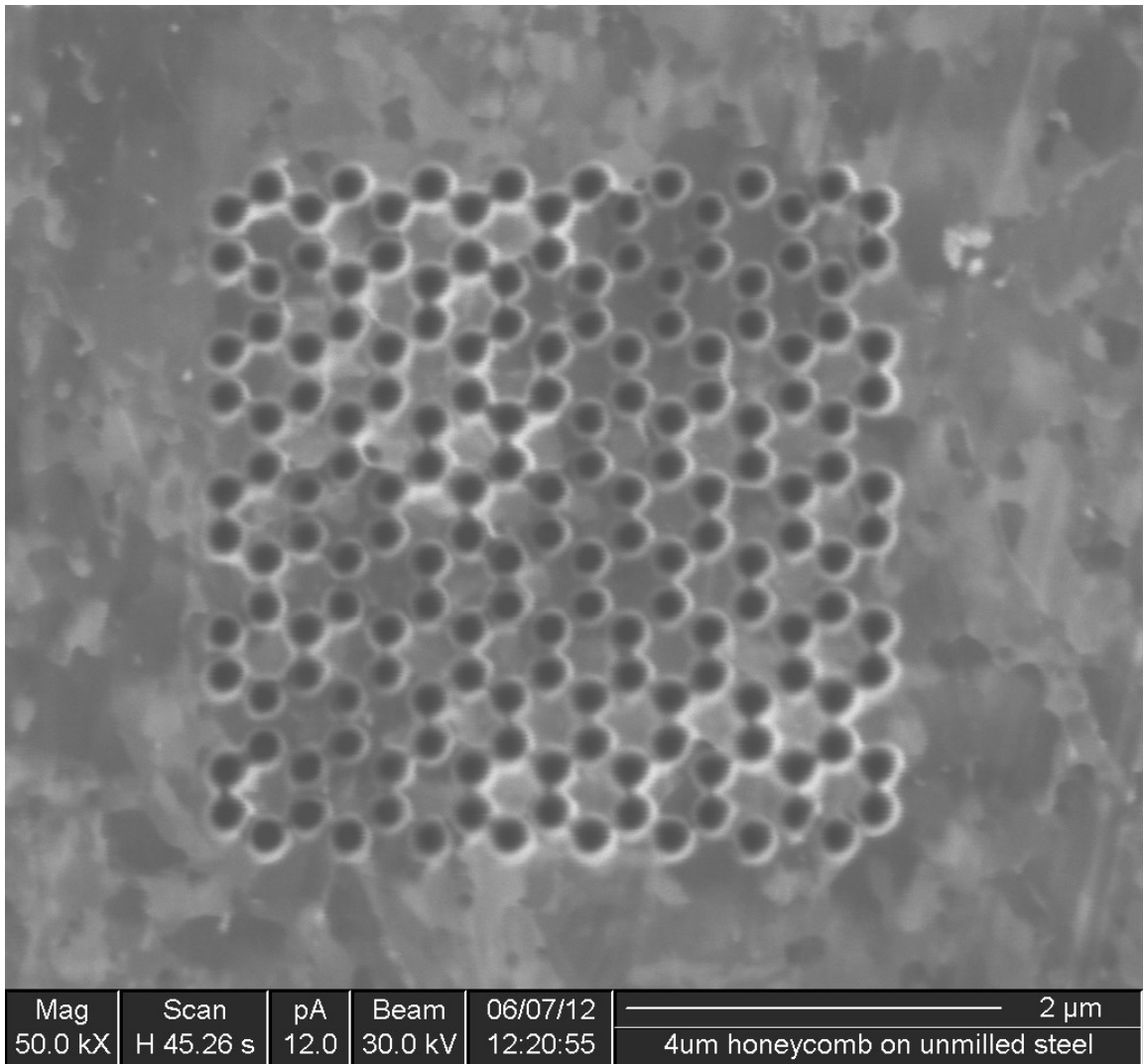


*Figure 13 - A honeycomb lattice of holes milled using a milling script in parallel on unsmoothed steel*

continues to move slowly over time, is the most common and has the largest magnitude. Aligning multiple honeycomb lattices to form a single larger photonic crystal was deemed infeasible (an example of mismatch due to drift can be seen in Figure 14), and so this lattice type was abandoned as a candidate for initial prototyping via FIB milling.

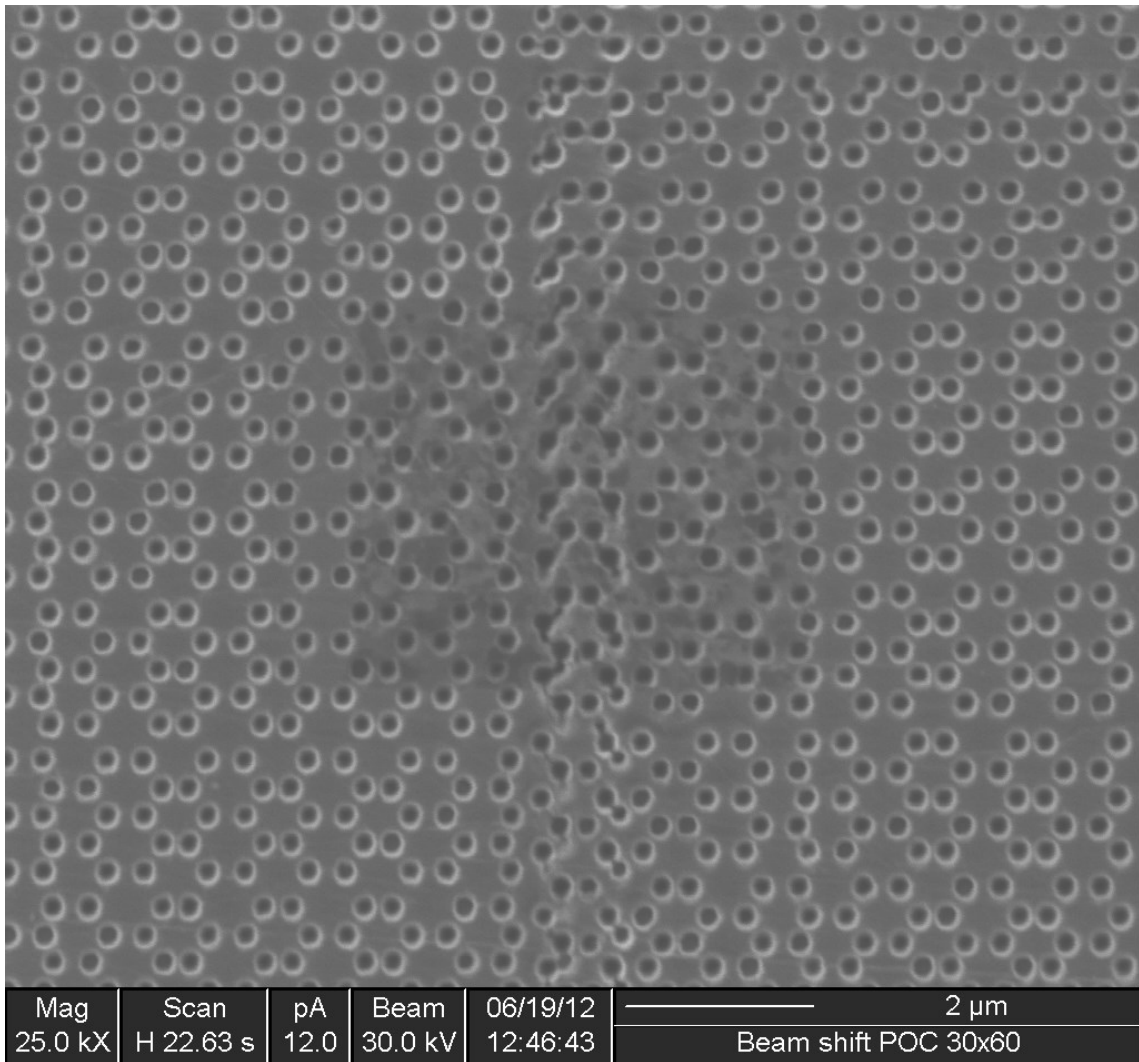


*Figure 14 - Honeycomb lattice of holes milled using a serial mode milling script. Note that holes are not connected, unlike parallel mode. Beam shift was used to try to align two patterns; overlap errors are clearly visible at the center of the image.*

#### 4.2.5 Square Lattice

With the honeycomb lattice determined impractical, a square or triangular lattice would have to be used instead. Given that a honeycomb lattice is just a triangular lattice with a two-feature unit cell and proved difficult to align, it was suspected that a triangular lattice would pose similar difficulties. After confirming that a square lattice could have useful

band gaps with the materials of interest, it was decided to proceed with square lattice designs rather than triangular.

Simulations indicated that a square lattice of round rods should yield useful band gaps. However, as mentioned earlier, the limitations of the milling script make the production of round pillars difficult and slow. Round holes were considered, but milling a lattice of round holes would have run into a similar set of problems as honeycomb milling. Serial milling tends to re-deposit material into previous holes, and parallel milling leads to unwanted material removal. Additionally, square lattices of holes ended up producing structures that were more similar to a pillar lattice than a hole lattice. After initial milling of a square lattice of holes, the pointed pillar-like structure which resulted can be seen in Figure 16, which is a tilt view of the same pattern as Figure 15.

In order to avoid these problems, and given the ease of milling rectangular structures, an obvious target of further investigation was square pillars. Simulation revealed that a square lattice of square pillars would yield useable band gaps, though the band structure is not as desirable as round pillars. Square pillars provide a major increase in ease of production; the entire pattern can be defined with a relatively small number of box patterns.

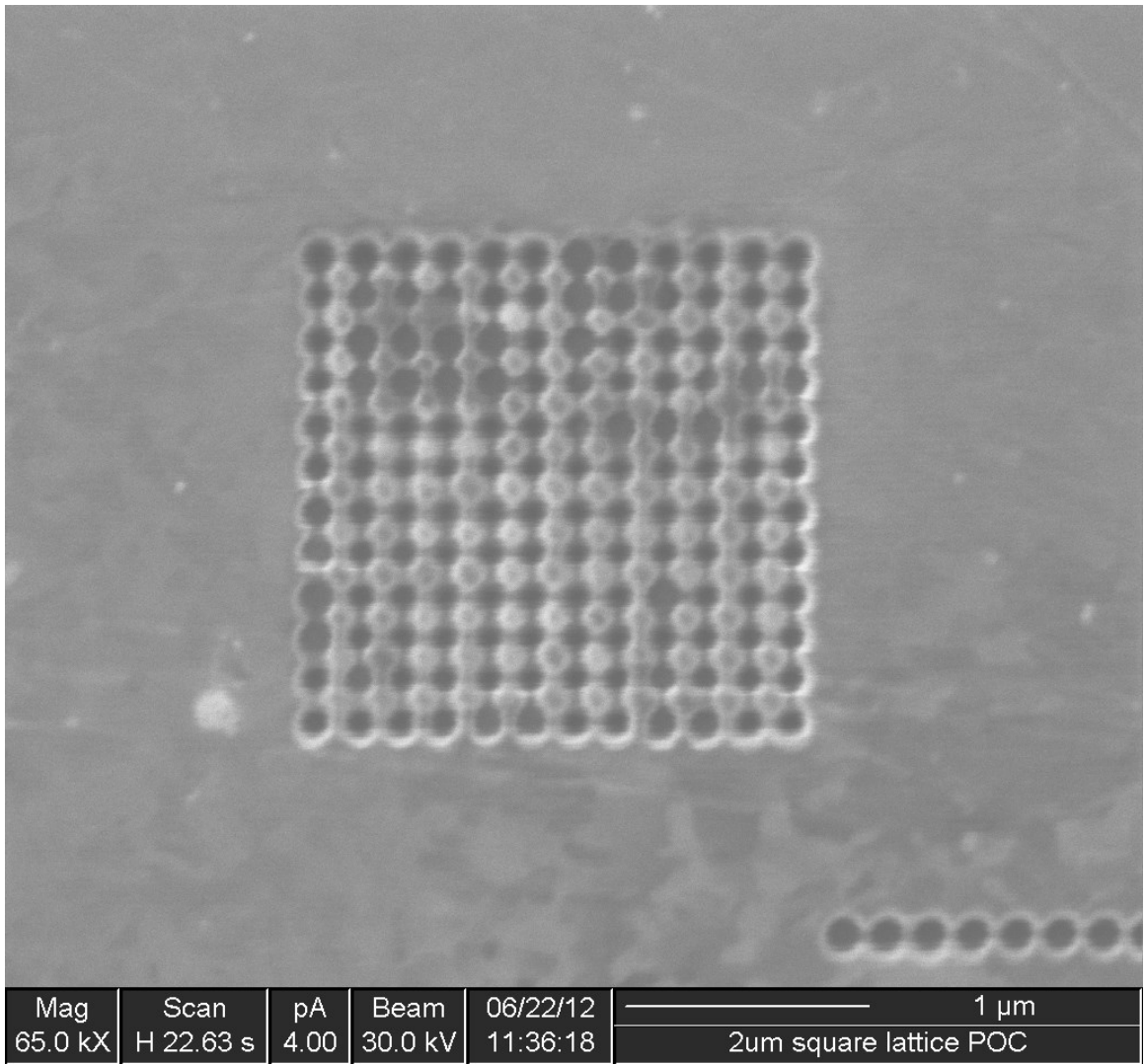


*Figure 15 - A square lattice of holes*

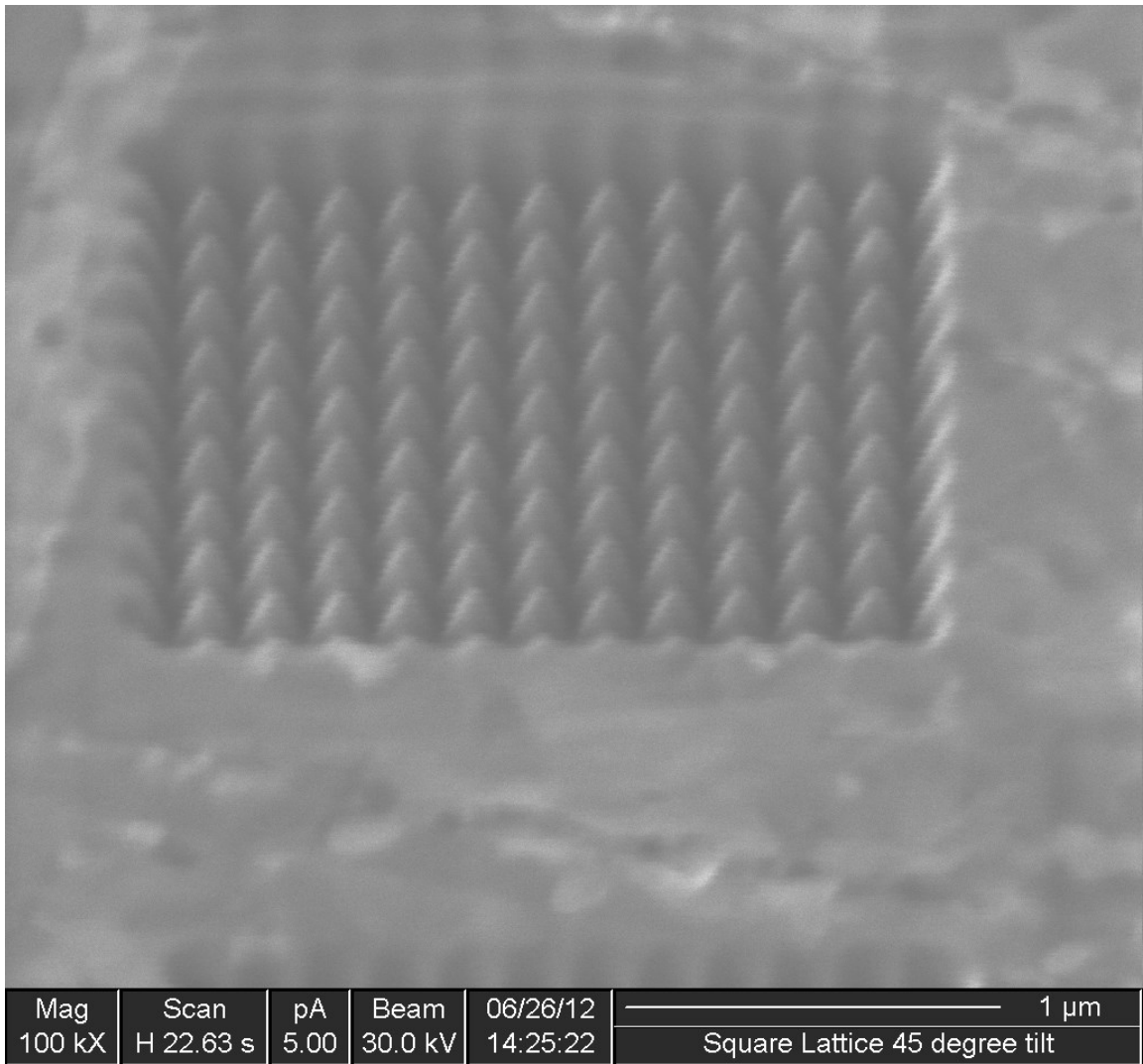


*Figure 16 - 45 degree tilt view of a square lattice of holes; note that the result more closely resembles a square lattice of pyramidal structures.*

#### **4.2.6 Parallel vs. Serial**

With a lattice selected, the ideal milling mode needed to be determined. It was recognized from previous work on honeycomb lattices that parallel milling tends to result in undesired material removal, but also has reduced re-deposition. An example of parallel milling and the undesired material removal can be seen in Figure 17 and Figure 18, where the tops of the pillars are well below the surface of the un-milled material. Building up a protective layer to mill through was considered as a method to reduce undesired material removal by having the beam remove the sacrificial coating rather than the substrate while moving from one dwell point to another. This technique was tested with moderate success with a protective/sacrificial layer of platinum deposited on silicon. Figure 19 and Figure 20 are images of a test of the protective coating method.

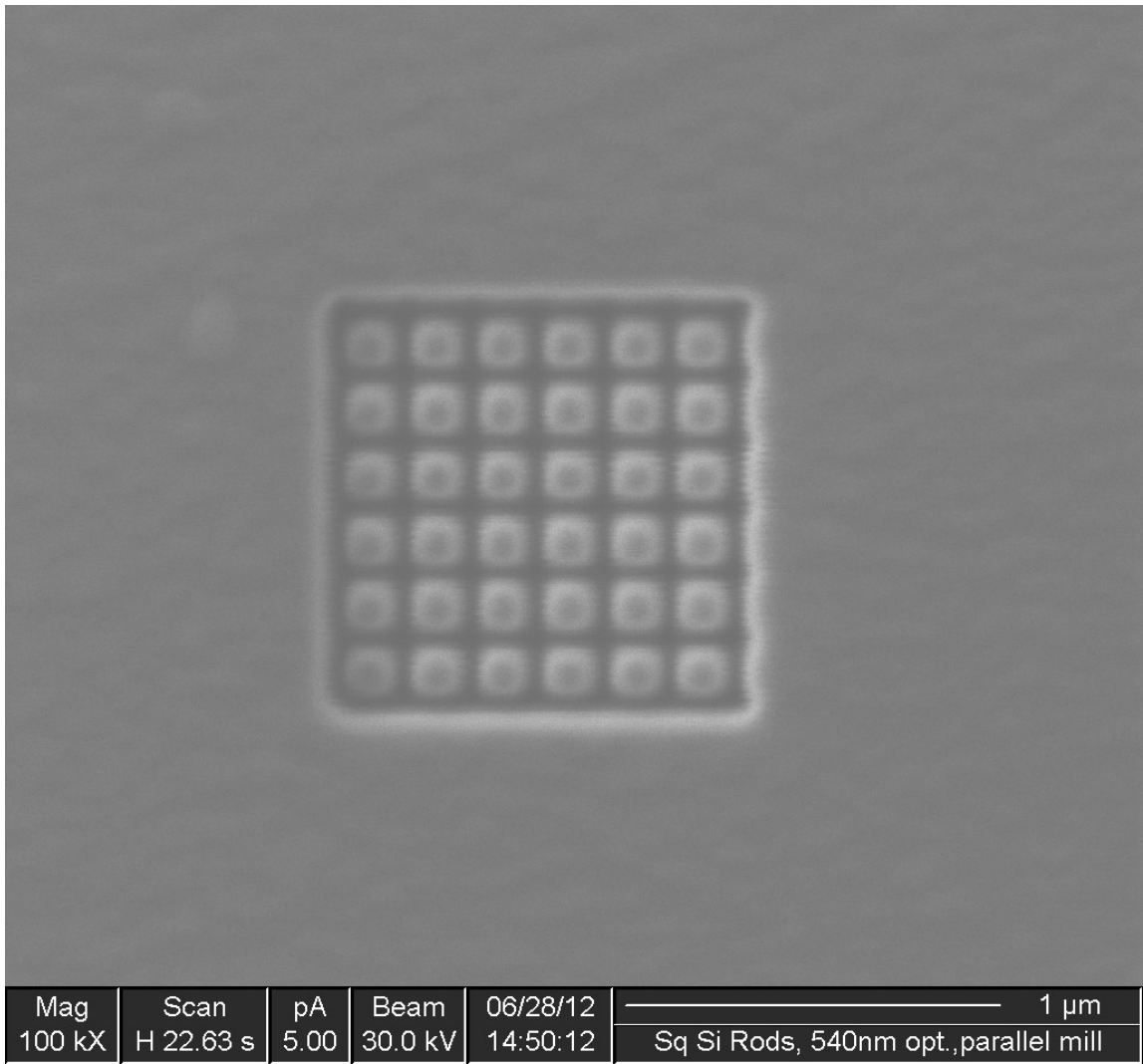


*Figure 17 - A square lattice of square rods in silicon milled in parallel*

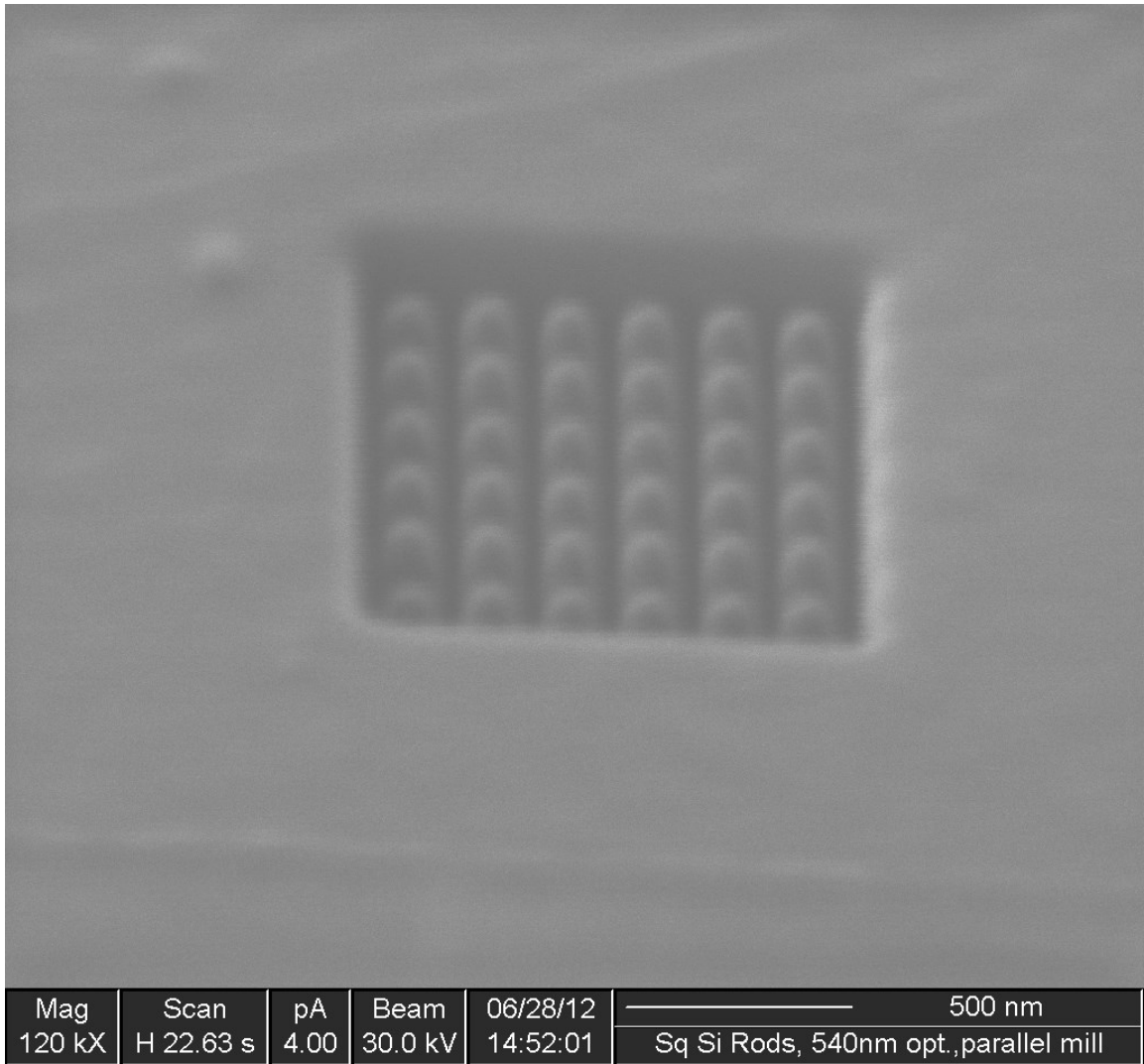


*Figure 18 - 45 degree tilt view of a square lattice of square rods on silicon milled in parallel. Note that the top of the pillars is significantly lower than the un-milled surface. This is an effect of parallel milling.*

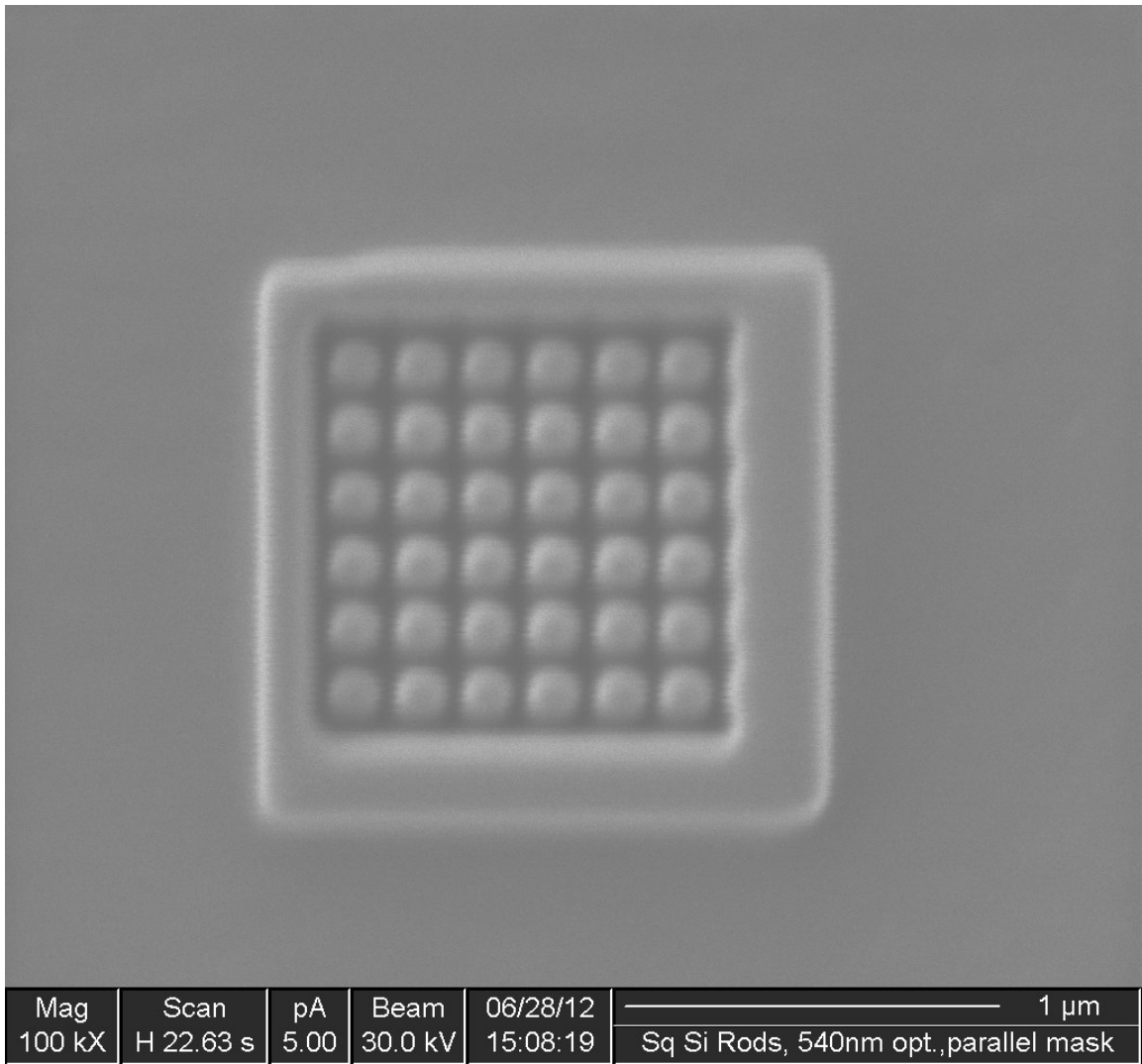


*Figure 19 - Square lattice of square rods on silicon milled in parallel through a protective layer of platinum.*

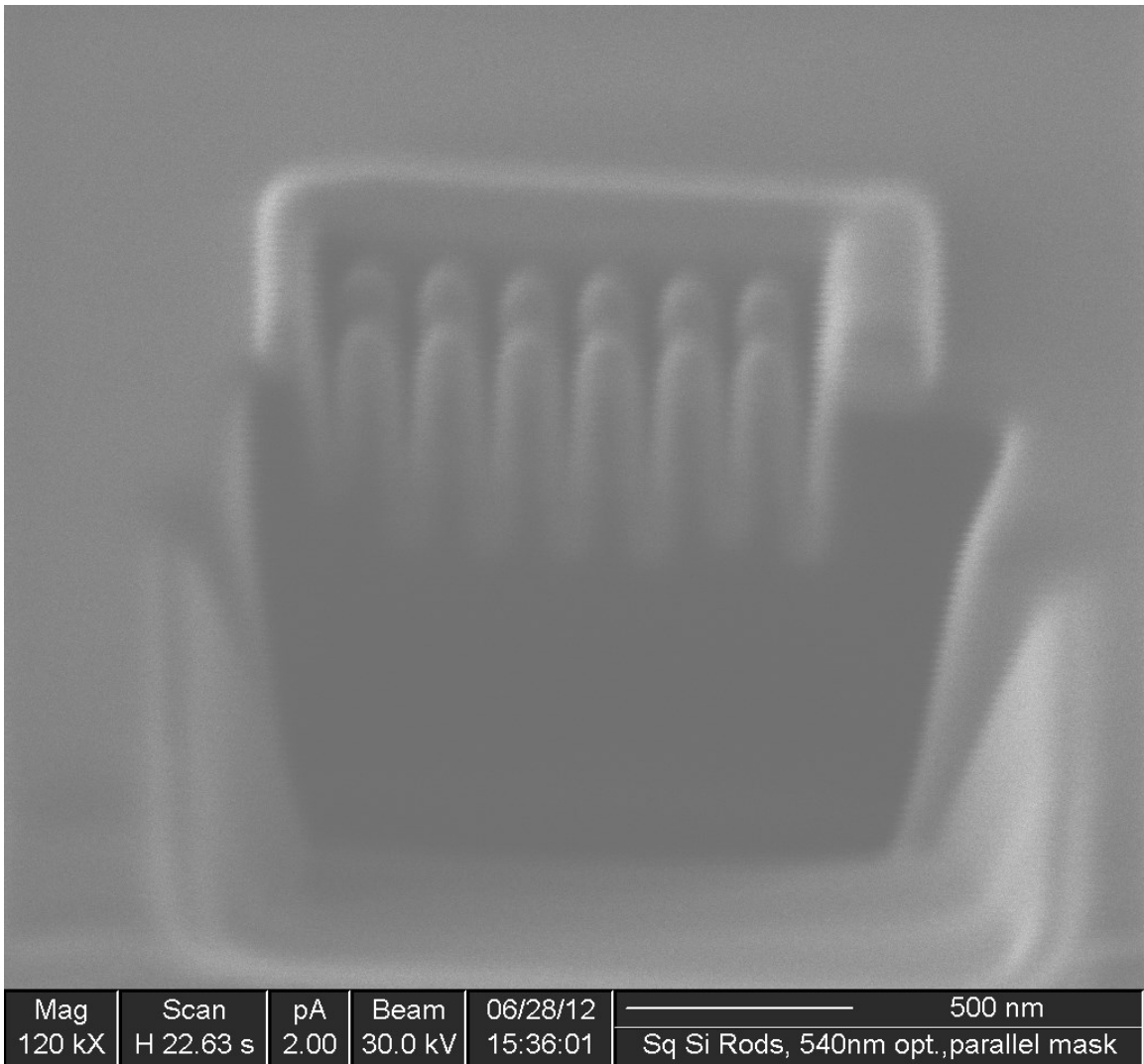


*Figure 20 - 45 degree cross section view of square lattice of square rods in silicon milled in parallel through a protective layer of platinum.*

Serial milling of the trenches was expected to produce clean patterns with some re-deposition. For initial tests, very deep trenches were used so that re-deposition would not be an issue. Initial experimentation with this milling method at very low beam currents was extremely promising; results of this test can be seen in Figure 21 and Figure 22. Small beams at small crystal sizes are able to produce very well defined trenches. It is

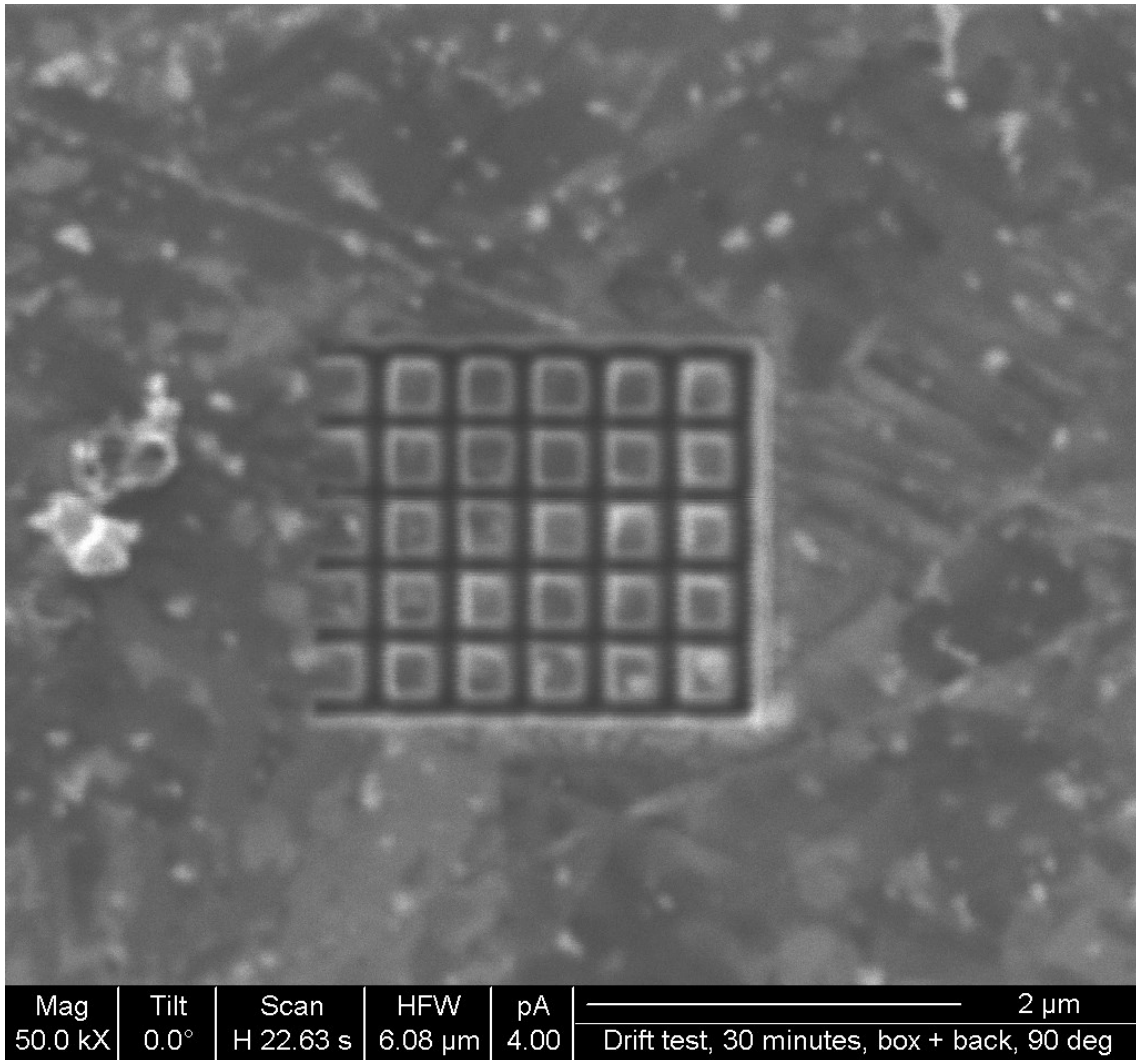


*Figure 21 - A test of a square lattice of square rods on steel*

important to achieve a structure that conforms as closely as possible to the idealized structure simulated in MPB; imperfections in the lattice, and/or shape of each pillar can have undesirable effects on the band gap structure of a photonic device. Fortunately, lattices of rods have been shown to have reduced sensitivity to size variations [25].

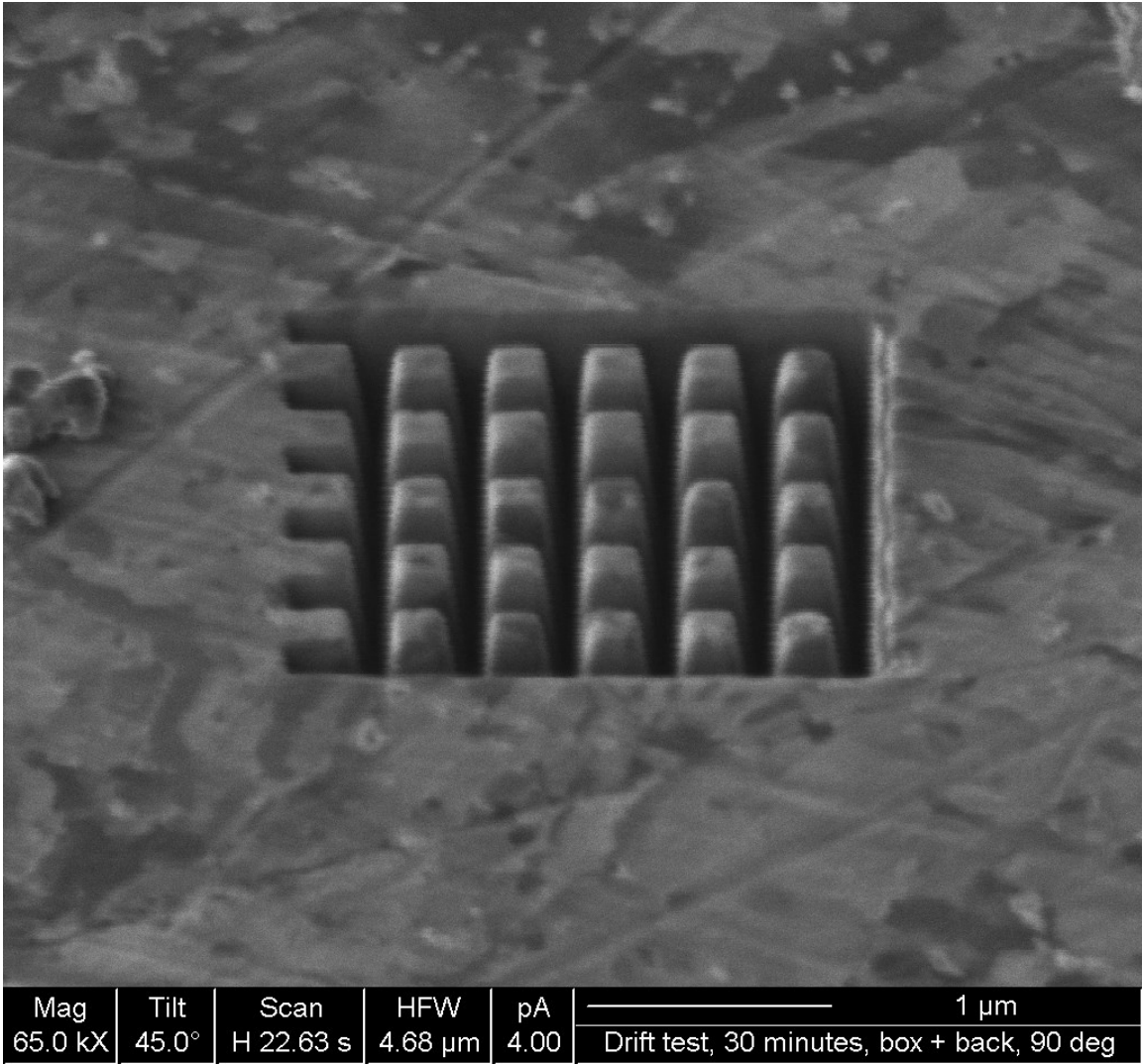


*Figure 22 - 45 degree tilt view of a test of a square lattice of square rods on steel*

### 4.3 Quality Control

#### 4.3.1 Depth

Milling depth is simply set using the included software. However, for both the FIB800 and DualBeam835, there is no feedback on the actual milled depth. Indeed, it would be very difficult if not impossible to create a method in which actual milled depth could be

determined in real time. There is a technique known as end point detection that can be used in some circumstances, typically when multiple layers with different electrical conductivities are present; end point detection is commonly used in the semi-conductor industry. The basic operating principle is that the stage current is measured, and a change can be observed once the beam has burned through one layer to a more conductive layer. For the LightGauge project, end point detection is not useful because all of the milling is taking place on bulk material; there is no layered structure to facilitate end point detection. Consequently, depth control and optimization was an empirical process.

Various depth lines or patterns were milled in the materials of interest and the results examined to determine which settings would be sufficient. For work outside of prototyping a small number of samples, it would be useful to attempt to produce an equation relating depth setting to actual milled depth on various materials. Rather than perform this correlation for the LightGauge project, a more empirical method was used; patterns were milled at a high depth first, and then increasingly shallower until no or weakened photonic effect was observed. These test patterns can be seen in Figure 23. The shallowest setting that yielded photonic effect was then used for all milling. It is important to note that the milled depth can vary significantly across the surface of a sample, most likely due to variation in local hardness or material composition.

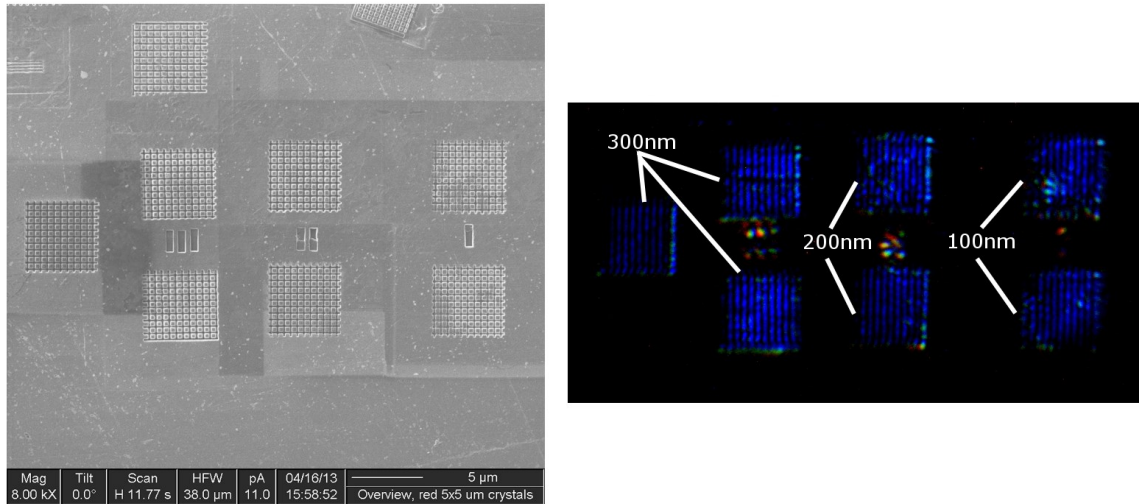


*Figure 23 - A simple depth test on steel. Pattern III was milled to a depth setting of 300nm, pattern II was milled to a depth setting of 200nm and pattern I was milled to a depth setting of 100nm. All three show an optical return signal.*

#### 4.3.2 Re-deposition

As discussed earlier, re-deposition during milling is a major issue that must be addressed.

The exact mechanism was not investigated for this project, but it was quite clear that during serial milling adjacent features tend to accumulate re-deposited material.

Obviously this is problematic for the production of photonic devices, as it negatively impacts both the depth and aspect ratio of milled features.

In order to alleviate re-deposition, a re-mill step was added to the milling process. A first pass at the full depth setting is milled for the vertical and then horizontal trenches in serial mode. Subsequent mills in the same location at lower depth settings are then performed to remove re-deposited material. Depth settings for the re-mill steps were

empirically optimized. Results were improved when the second re-mill step was not as deep as the first, as there is less re-deposition on the second primary mill.

### **4.3.3 Beam Current**

The beam current at which the pattern is milled is perhaps the most important setting for determining the quality of the resulting structure. The manner in which the ion beam is produced does not produce a spot of uniform intensity; the spot is more intense at the center than the edges. The beam current is limited by use of a physical aperture, and thus a large beam current is also a larger spot size. It was necessary to balance milling time (higher beam currents mill faster) with crystal quality (smaller beam currents produce cleaner features).

Beam spot size is one area in which the milling capabilities of the two tools vary significantly. The FIB800 is a pre-lens column tool, while the DualBeam835 is a magnum column tool. The effective difference is that the DualBeam835 can achieve a higher beam current per spot area. This is highly desirable, as it allows for smaller features to be milled with a larger current (and thus faster) than is possible with the FIB800 pre-lens column tool. It was found that similar results could be achieved at 100pA on the DualBeam835 as were machined at 11pA on the FIB800; this represents a very large savings in milling time.

In the following set of figures (Figure 24 through Figure 28) the impact of the larger beam currents used for milling is investigated. The larger beam currents have larger beam spot sizes due to the larger aperture and higher positive ion repulsion. As the beam

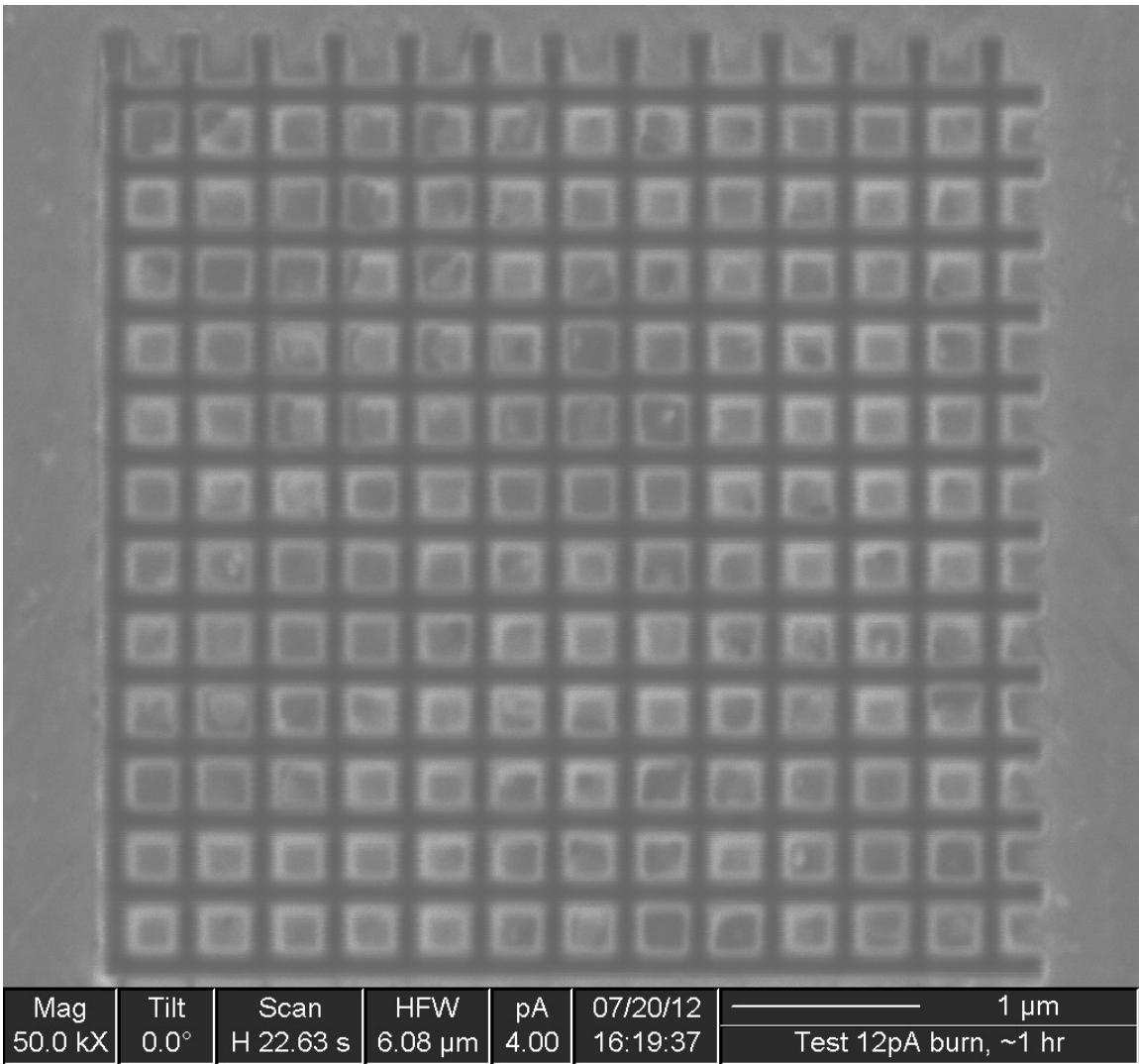


*Figure 24 - A square lattice of square rods on steel milled serially with re-mills at 12pA beam current.*

current increases the spot size increases with a Gaussian like profile. This larger beam spot results in loss of resolution of the final milled product. Higher beam currents result in a larger radius of curvature on the surface of the rod structures. This increase in radius has a negative impact on the photonic crystal device and is undesirable. Optimization was needed to minimize the radius of curvature

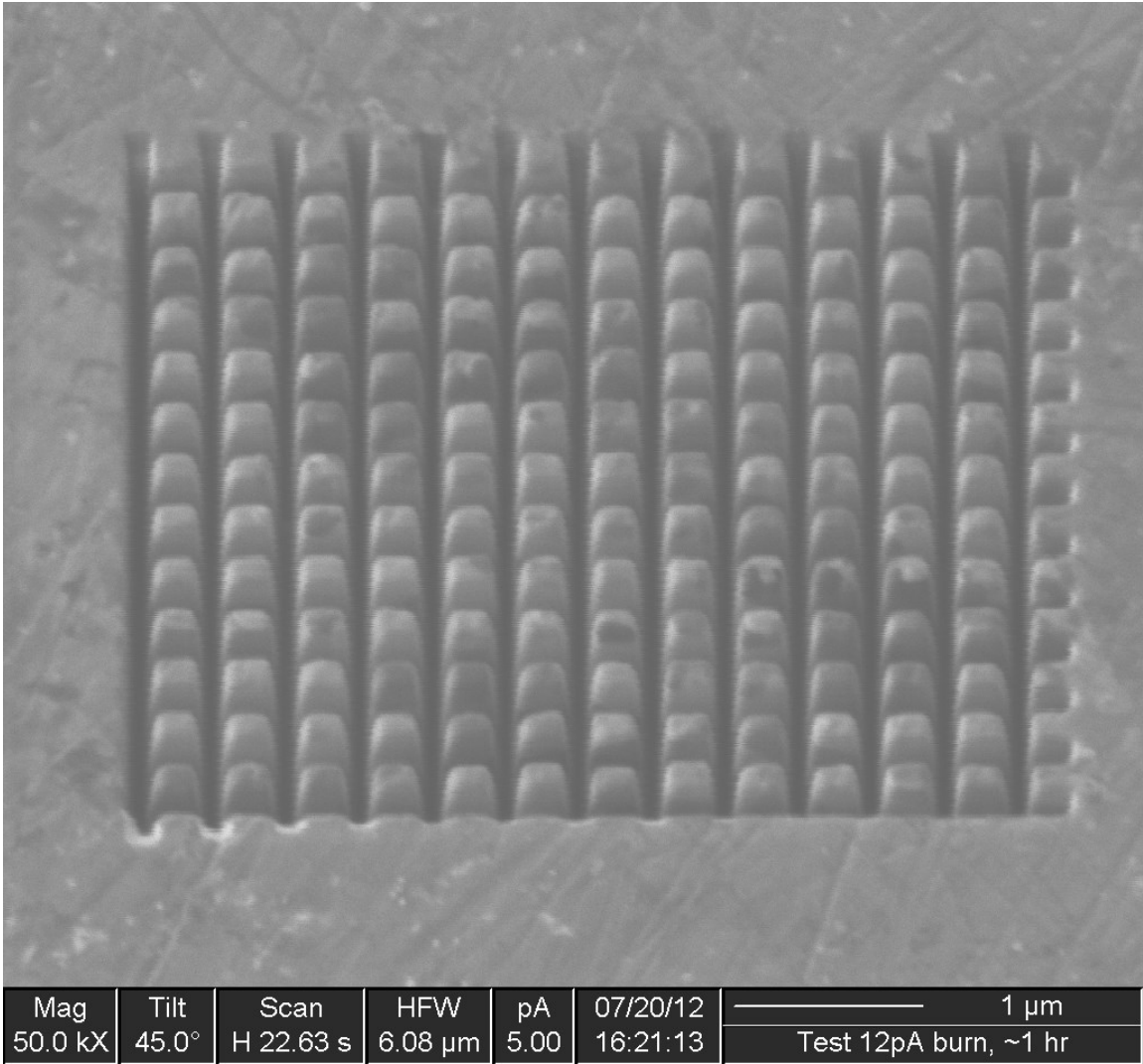


*Figure 25 - 45 degree tilt view of a square lattice of square rods on steel milled serially with re-mills at 12pA current.*

resulting from machining while also minimizing the milling time, which was inversely proportional to the beam current.

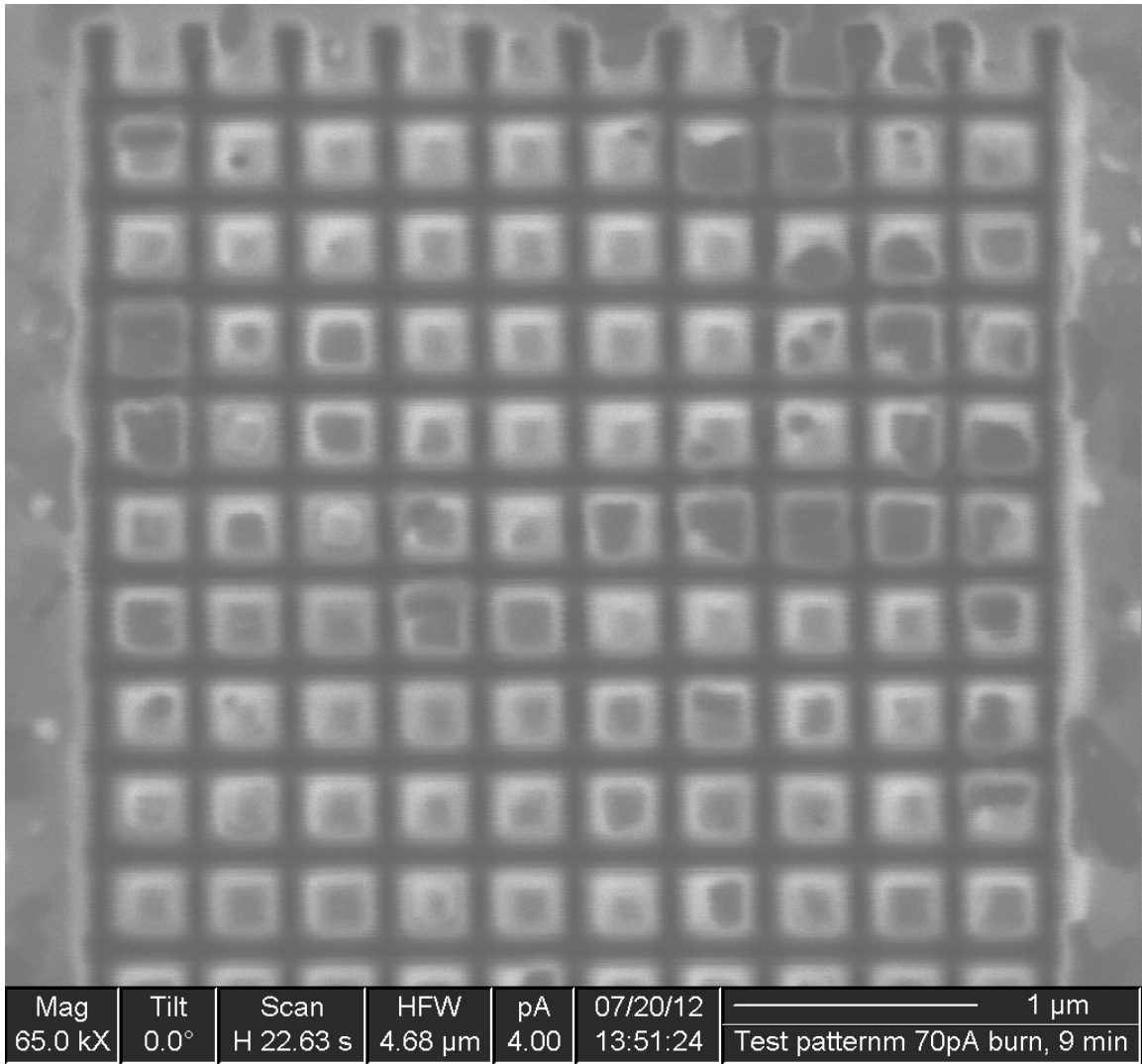


*Figure 26 - A square lattice of square rods milled serially with re-mill at 70pA*

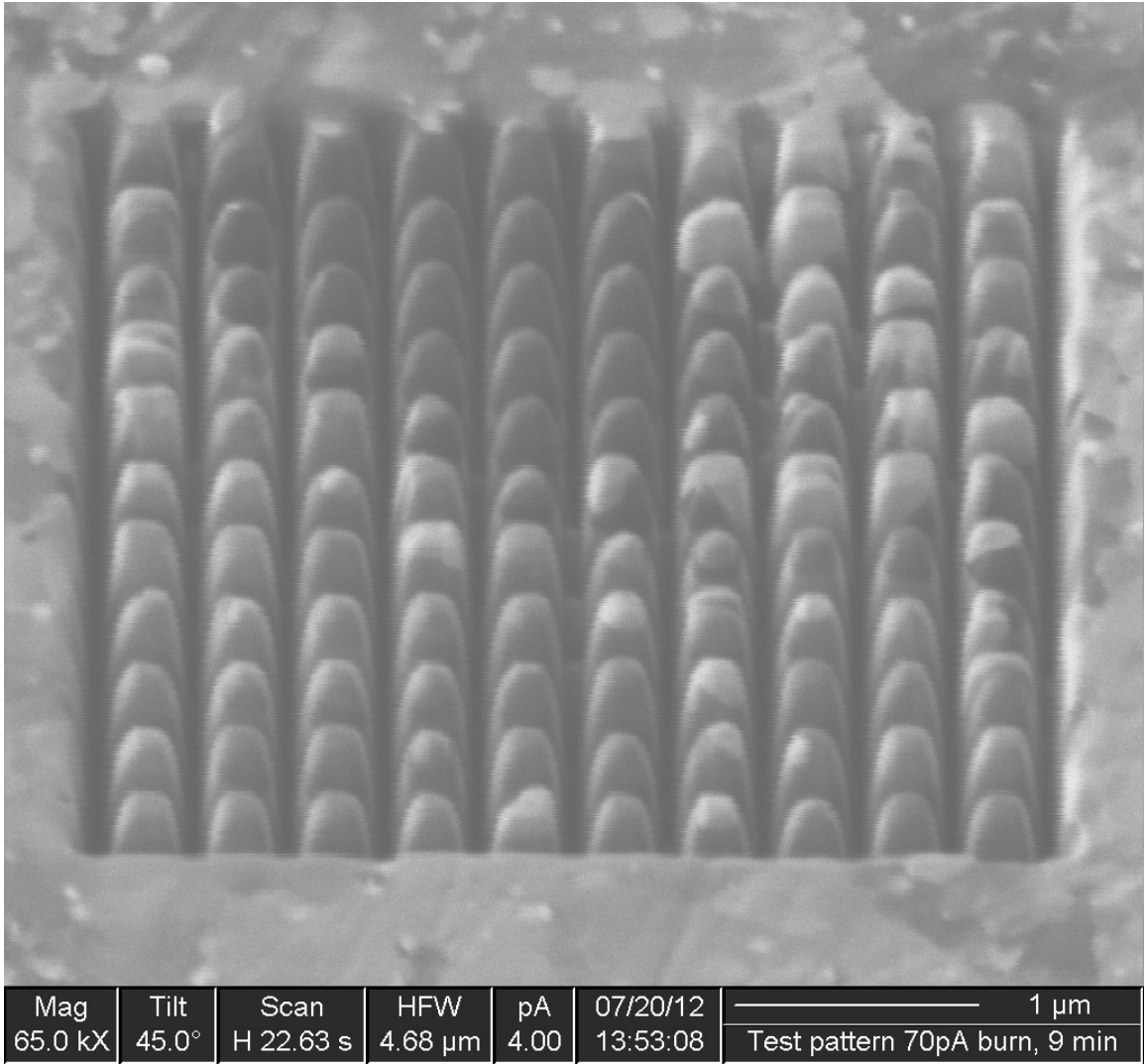


*Figure 27 - 45 degree tilt view of a square lattice of square rods milled serially with re-mill at 70pA*

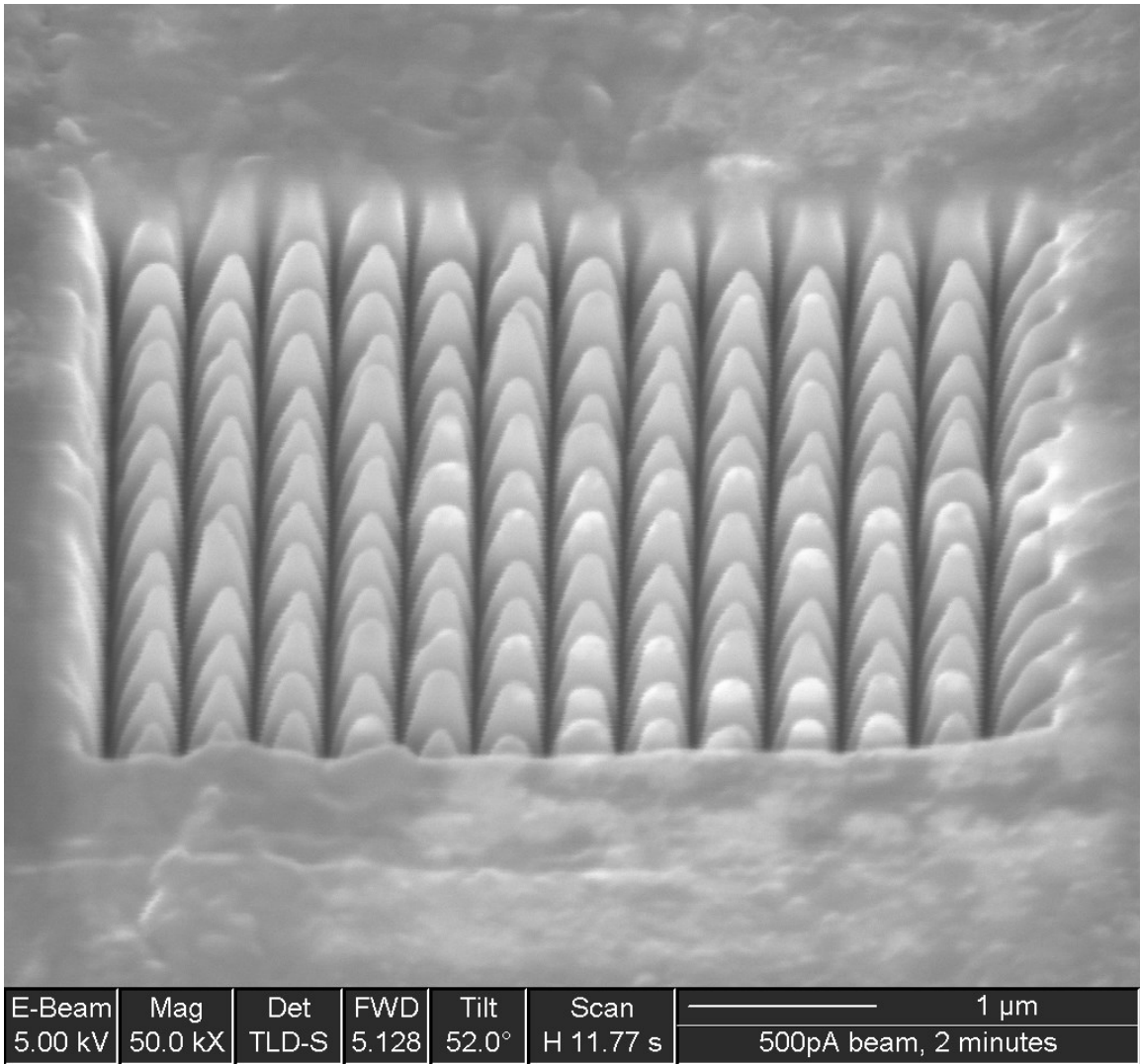


*Figure 28 - 52 degree tilt view of a square lattice of square rods milled serially with re-mill at 500pA.*

In an attempt to produce good quality structures more quickly, an alternate trench milling technique was investigated. Rather than use the milling script to draw a single box, a trench would be produced by milling a series of parallel line features with features farther from the center having decreasing depth settings. This experiment was designed on the assumption that the ion beam is significantly more intense at the center of the spot. The

idea was to overcome the slanted edges typical of a trench milled with the built in box feature at high beam currents by more precisely controlling the dwell time as appropriate. Figure 29 is a comparison of trenches milled with the line method versus the box method. Unfortunately, it was determined that a high beam current pattern with enough lines to produce the desired trench ends up taking about the same amount of time as a single lower beam current box and yields comparable results. With this being the case, this method was abandoned as a needless increase in complexity.

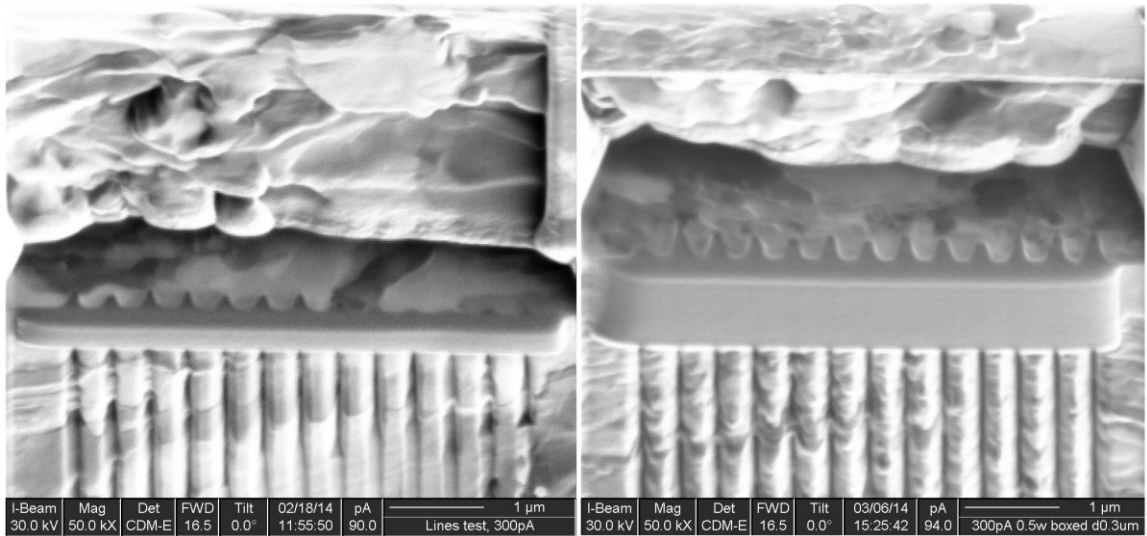


*Figure 29- A comparison of trenches milled with the multi-line method (left) and the box method (right)*

Due to the large timesaving implicit in using the DualBeam835, all four of the final samples were milled using the DualBeam835. These were milled at 100pA and 300pA beam current settings, as anything less than 100pA was too long of a mill to be practical, and anything greater than 300 to 400pA could not achieve pillars that were not clearly pyramidal. At currents of 100 and 300pA, the pillars of the photonic crystals in either material are not perfect; there is noticeable rounding of the tops of the pillars and the

sides are sloped. It is possible to achieve near perfect structures at lower beam currents. Some of the initial 4pA and 11pA test mills have excellent aspect ratios and top flatness. Unfortunately, the time required to mill an easily optically detectable array at 11pA is very long; for example, a 150um array would take approximately 900 hours to mill at this beam current.

#### **4.3.4 Drift**

Drift is a major concern when attempting to mill photonic crystal devices. The pillars of the steel photonic crystal design are approximately 120nm wide, so even a few nm drift per hour is sufficient to make milling a large photonic crystal device (10+ hours milling time) impossible, because the optical response of the crystal should be very sensitive to changes in pillar size. Additionally, this kind of drift can lead to non-uniformity in the photonic device. In Figure 30, the uncorrected drift can be seen in the serial milled array of holes. As milling sizes increased, the oscillatory nature of the drift can be seen in Figure 31. This drift was intolerable.

There are multiple potential causes of drift, including stage movement, sample charging and thermal fluctuations. The most obvious and largest contributor was found to be stage movement. On both tools, if the stage has been recently moved, the drift will be very large, potentially on the scale of microns per hour. This is clearly untenable for the milling of structures with sub-micron features. Fortunately, it was determined that stage drift could be reduced by moving to the desired milling location and then allowing the stage to settle for several hours before beginning milling operations.

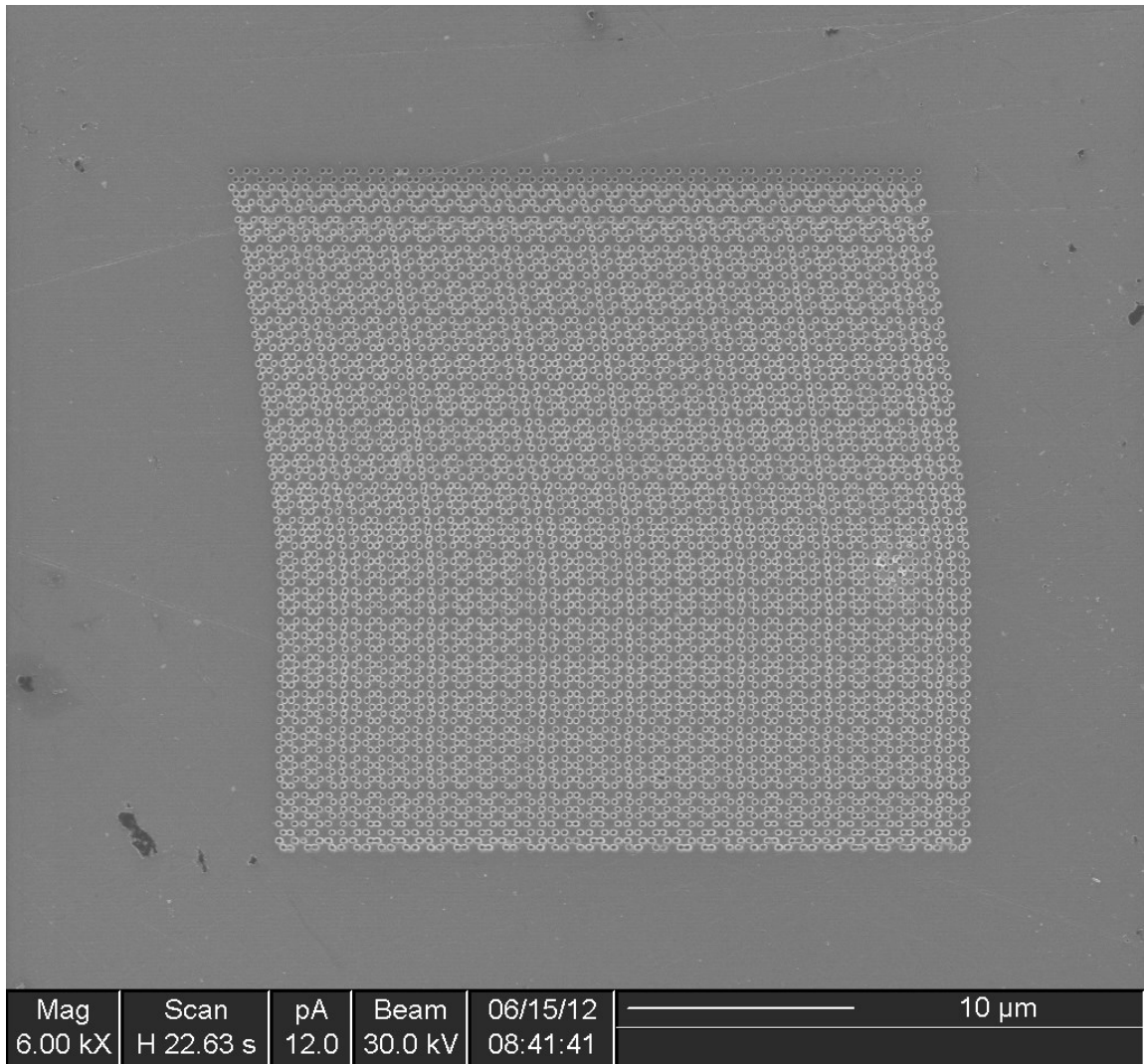


*Figure 30 - A honeycomb lattice where drift has caused the structure, which should be square, to shift to the left over time.*

While the reduction in stage drift from allowing the stage to settle is significant, there was still sufficient drift to make milling large photonic crystals problematic. A good drift correction software package could probably alleviate the remaining drift, but the performance of the drift correction included with the built in milling software was insufficient and another solution was needed.

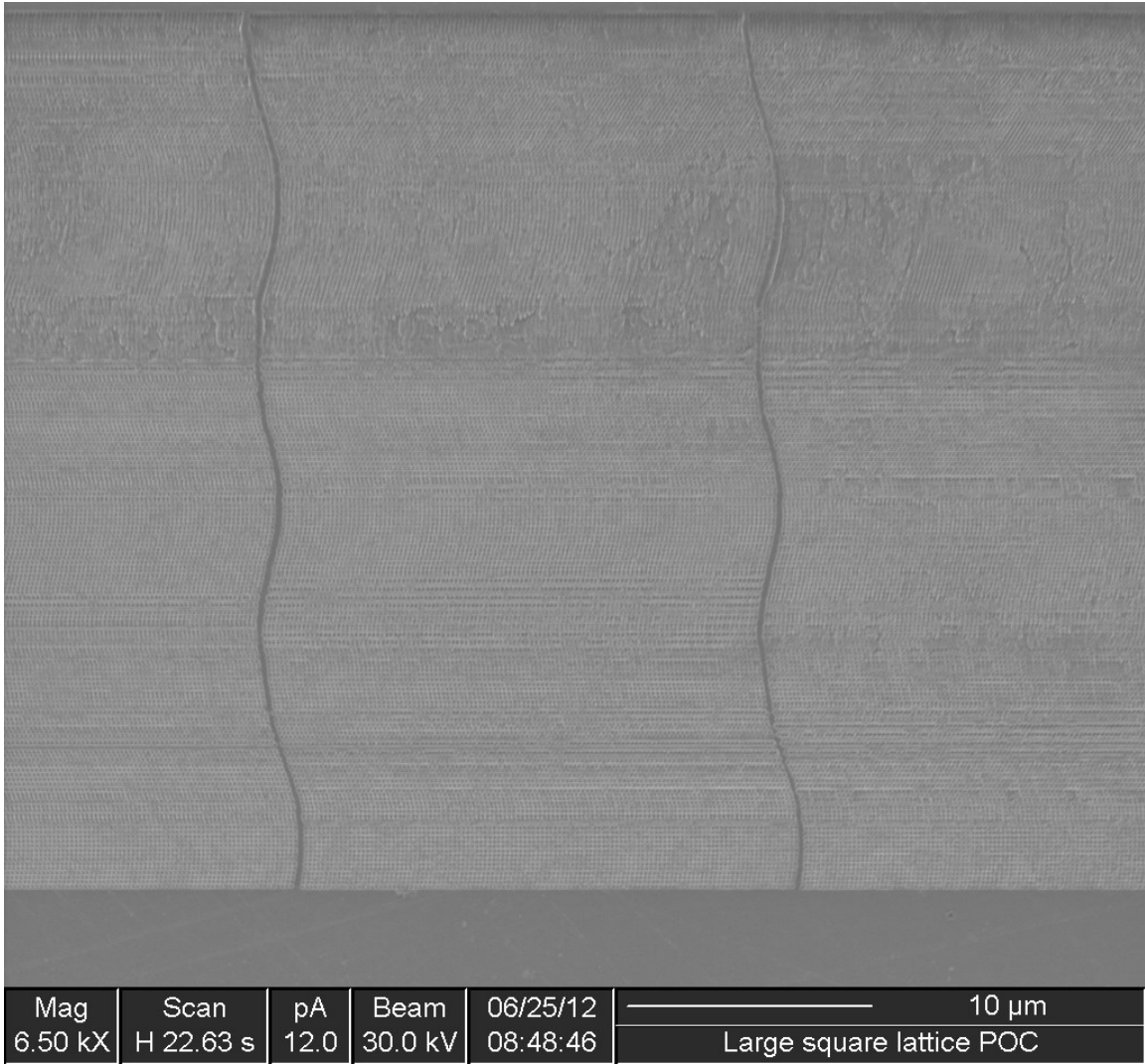


*Figure 31 - A very large honeycomb lattice test where long term cyclic drift has caused the clearly visible wavy border between structures.*

#### 4.4 Photonic Crystal Arrays

In order to be able to verify that a structure is in fact exhibiting the desired photonic behavior, it is necessary for it to be large enough to optically interrogate. The type and magnification of the interrogating sensor determine how large of a device is required. While an interrogation rig using an optical microscope with high magnification was designed and constructed, it had poor results when used in conjunction with a spectrometer, though it did provide some valuable qualitative results. In order to interrogate a device without magnification, the device must be fairly large.

In order to avoid drift issues, arrays of smaller photonic crystals were investigated. By limiting the size of each individual photonic crystal, drift induced error and non-uniformity can be minimized.  $5 \times 5 \mu\text{m}$  photonic crystals on steel could be milled at most beam currents sufficiently quickly that drift was not an issue. A single such photonic crystal is observable via optical microscopy with the custom designed microscope built for this project, as can be seen in Figure 32, which is an array of 16 such photonic crystals. In Figure 33, the same array can be seen as imaged with a FIB tool.

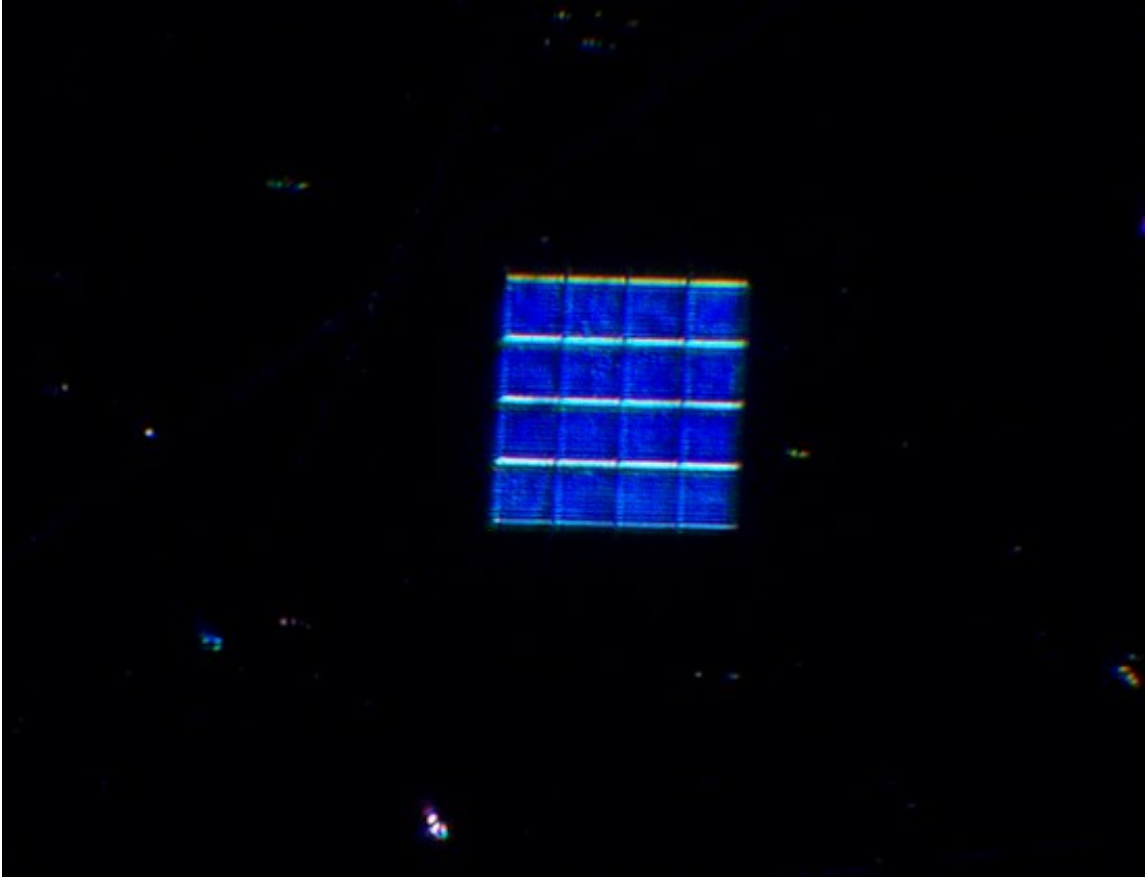


*Figure 32 - An array of 16 photonic crystals imaged via optical microscope under oblique lighting*

Multiple individual photonic crystals are then milled adjacent to each other to form larger arrays. To avoid introducing additional drift, beam shift is used to move to the next milling site rather than stage shift. Qualitative results under optical magnification were sufficiently promising to proceed to large arrays of these small photonic crystals. The final size of arrays generated using this method in a single run is limited by two factors, the length of time that the ion beam can run between heats, and the range of beam shift available. The LMIS can typically run for 50-100 hours between heats; the exact number

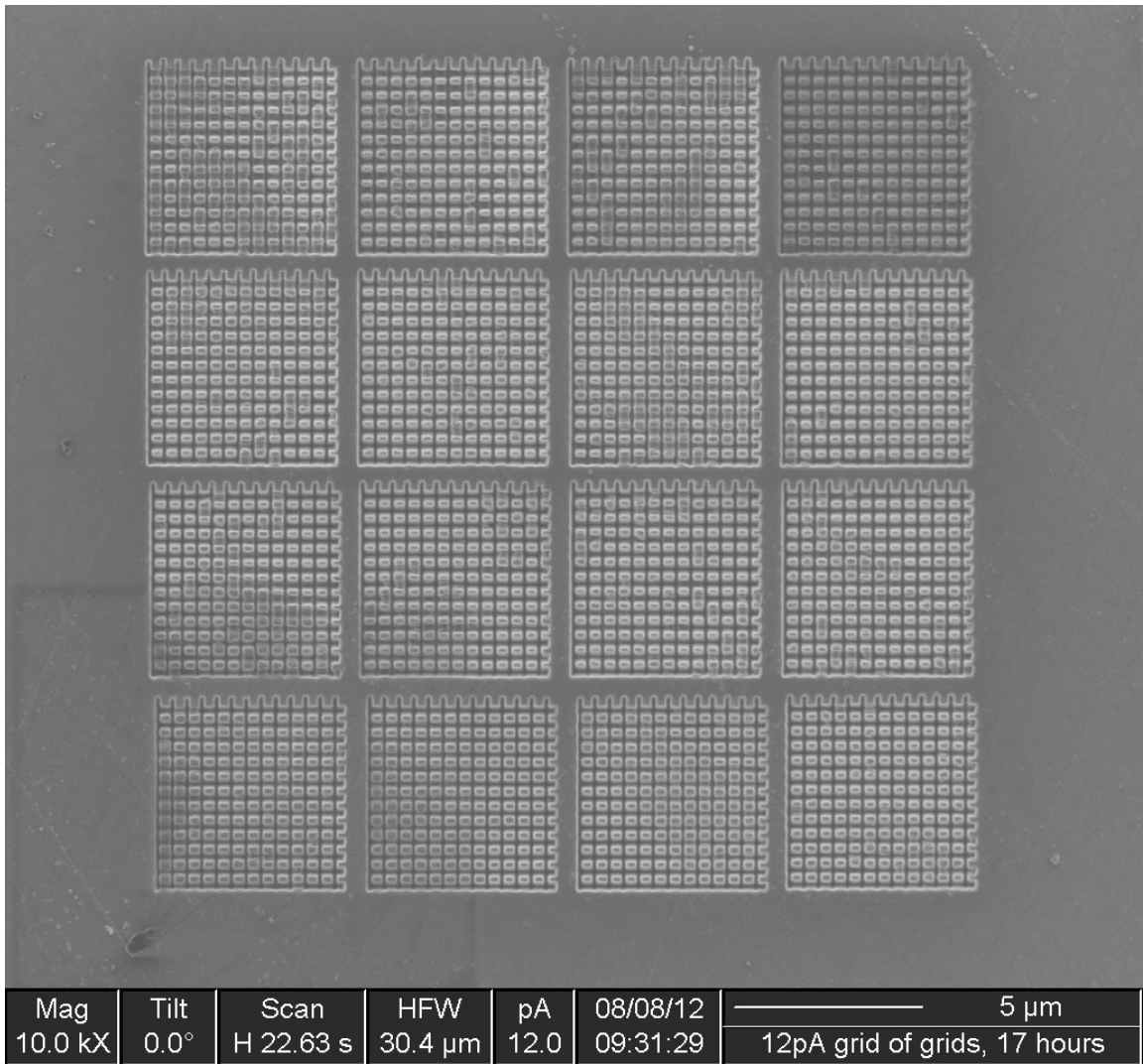


*Figure 33 - An array of 16 5 $\mu\text{m}$  photonic crystals on steel milled at 12pA*

varies, and a skilled operator can often achieve longer run times by carefully adjusting the ion source voltages. On both of the FIB tools used, the ion beam can be shifted by approximately 50  $\mu\text{m}$  away from zero, limiting the maximum single run array size to approximately 100x100  $\mu\text{m}$ . An example of four such arrays, total width about 150  $\mu\text{m}$ , can be seen in Figure 34. For something produced via FIB milling, this is a very large feature, and such arrays are easily visible without magnification.

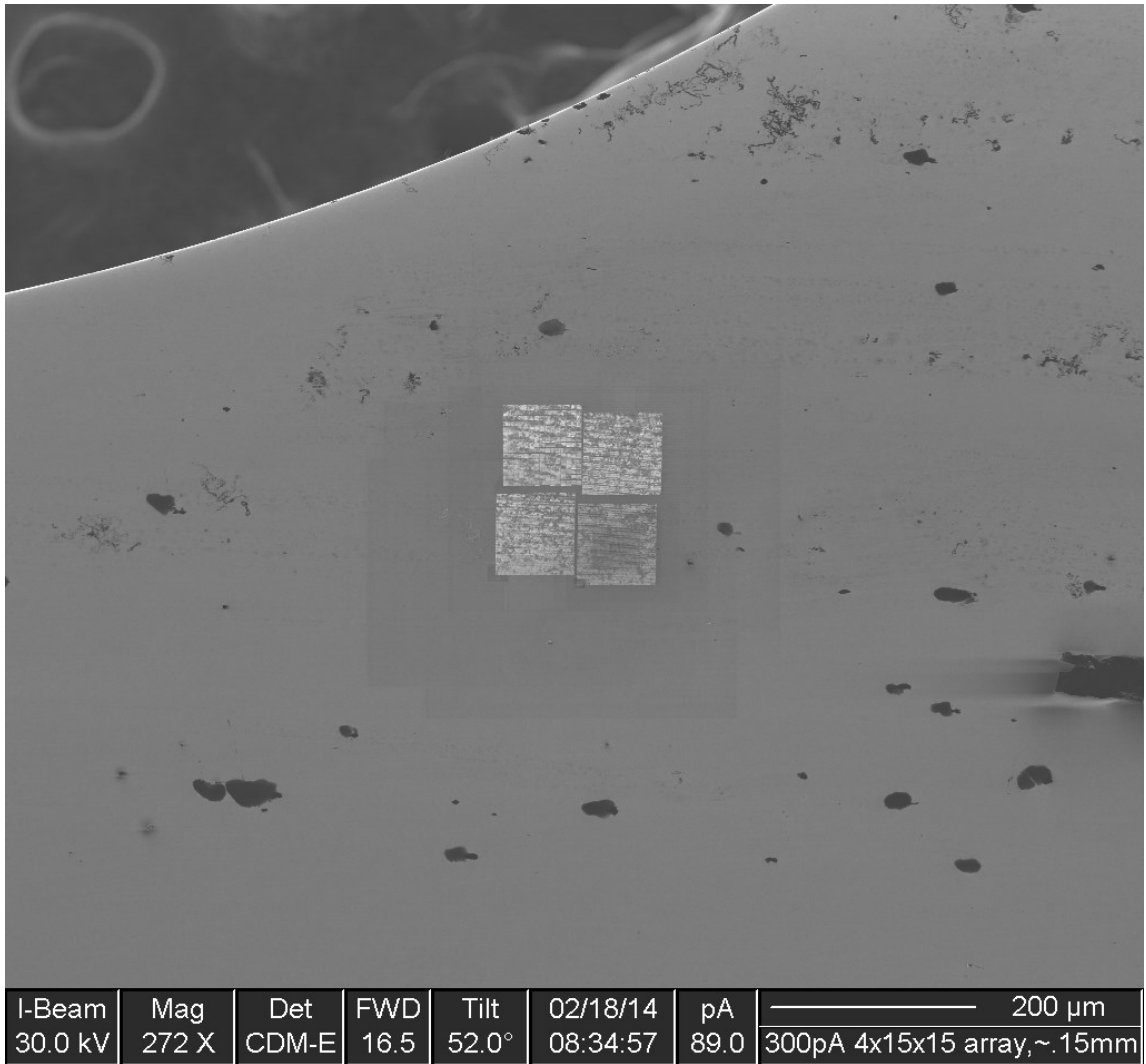


*Figure 34 – A large array of 4 arrays of 225 photonic crystals each milled on steel at 300pA*

200 μm is about one half of the width of typical fine mechanical pencil lead. The stage could be moved and multiple 100 μm arrays positioned adjacent to each other to produce any size photonic crystal array desired, provided time was not a limiting factor.

## **5. Results and discussion**

### **5.1 Photonic Device Size and Quality**

#### **5.1.1 Size**

For various reasons described in the production methodology section, the largest device produced at the writing of this thesis was approximately 150  $\mu\text{m}$  square. This is sufficiently large to be visible to the naked eye under the right circumstances, namely with a bright light source at the appropriate angle for a strong colored return. In addition, the large size provides more light to be gathered and measured by the spectrophotometer for wavelength measurements, and can be produced in a reasonable time frame with the FEI DualBeam system.

Two large array samples were produced on mild steel, and two large arrays were produced on zircaloy-4. The devices were milled with 300 $\mu\text{m}$  and 100 $\mu\text{m}$  apertures. All four of these devices were milled using the DualBeam835. In addition to these steel and zircaloy samples, some much smaller arrays were produced on  $\text{UO}_2$ . These devices were smaller due to a lack of large polished  $\text{UO}_2$  samples – because the only available flat regions were relatively small cleave planes, larger arrays could not be produced.

Figure 35 through Figure 38 are of photonic crystal arrays produced on steel. The difference in quality, most obvious in the rounding of the pillar tops, can be seen in the tilt views, Figure 36 and Figure 38. Figure 39 through Figure 42 are of photonic crystal arrays on Zircaloy. As with the steel arrays, the difference in quality (pillar top rounding) can be seen in Figure 40 and Figure 42. A much smaller photonic crystal on  $\text{UO}_2$  can be seen in Figure 43.

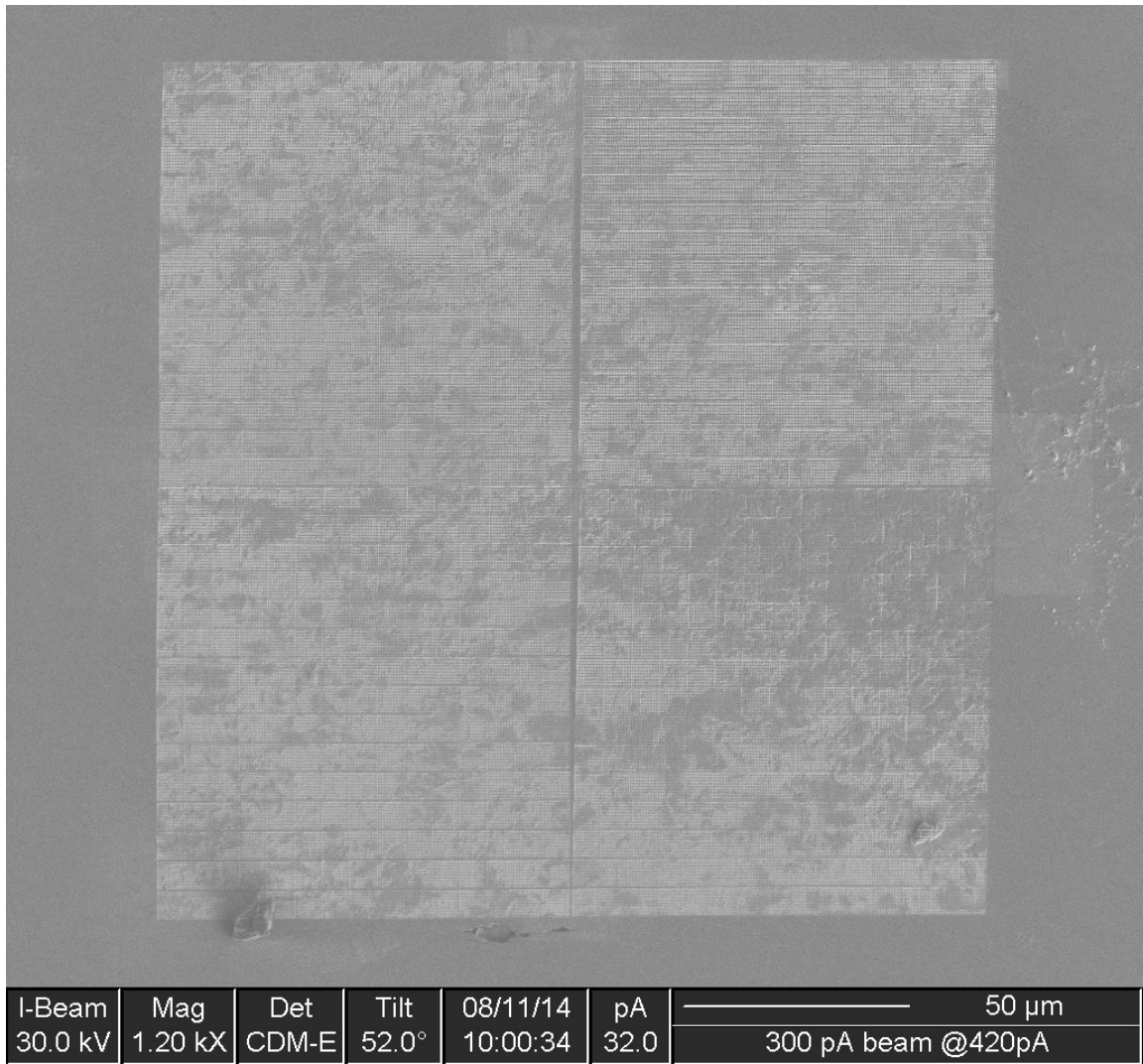


*Figure 35 - A large array of 4 arrays of 225 photonic crystals each milled on steel with a 300pA aperture*

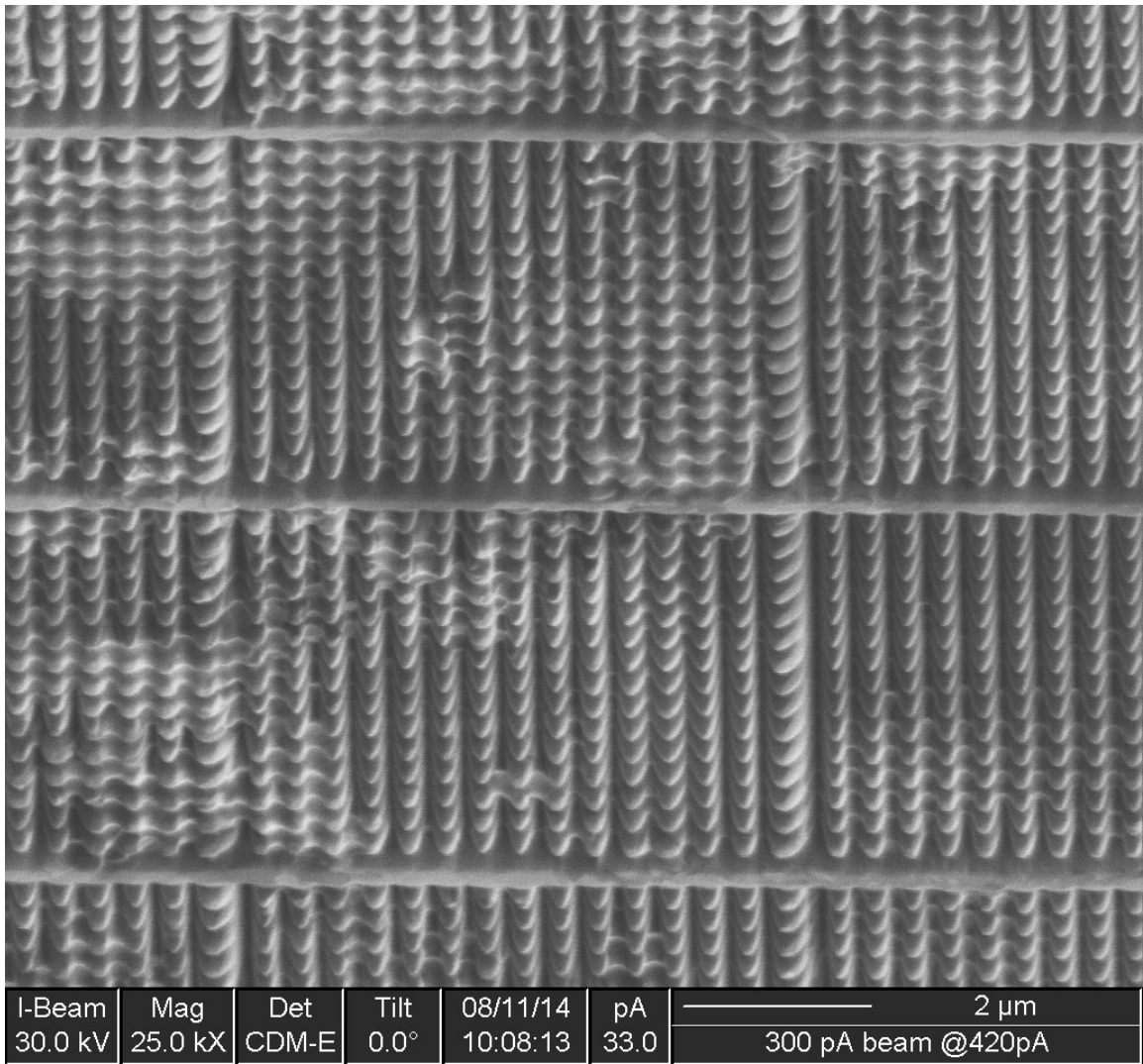
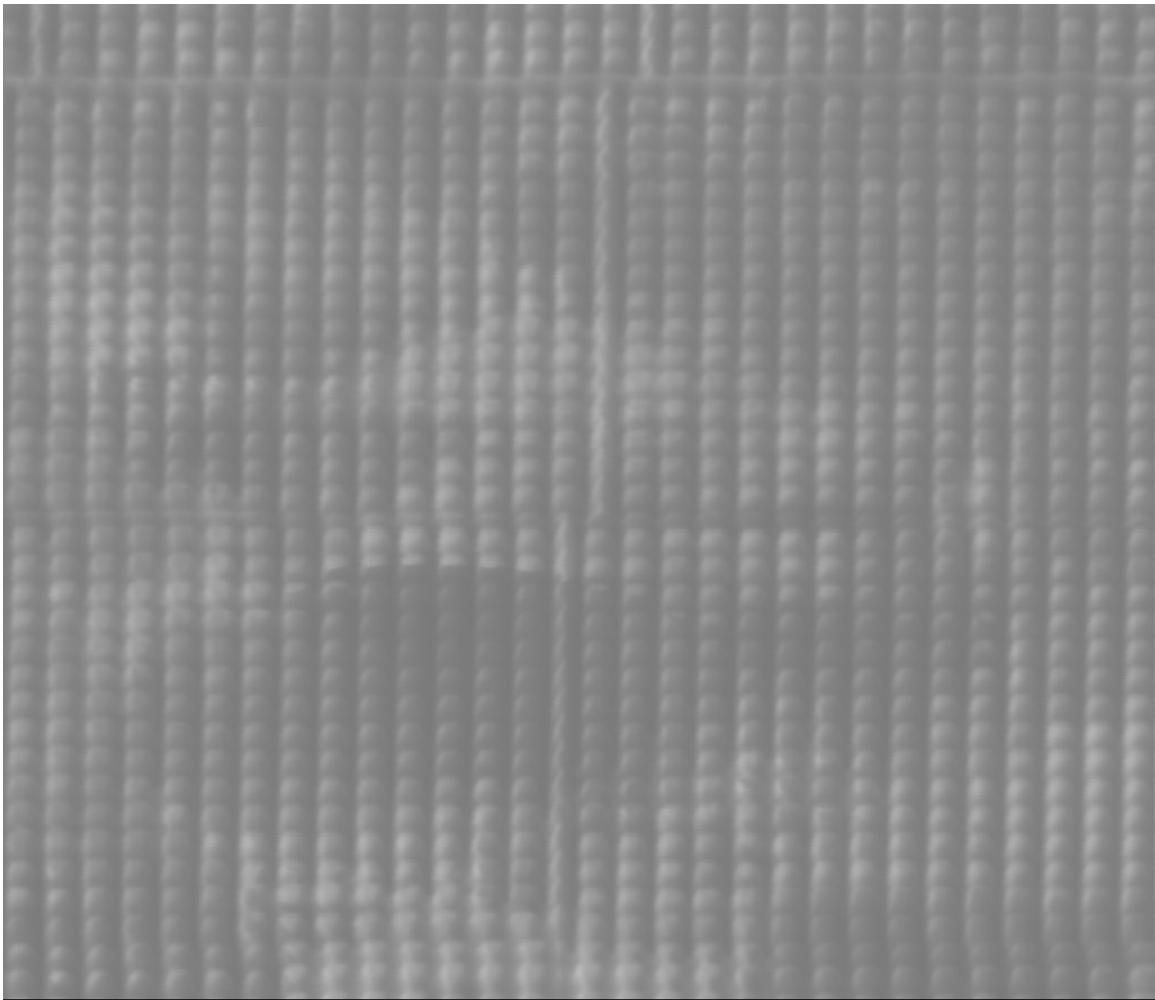


*Figure 36 - 45 degree tilt view of a section of a large array of photonic crystals each milled on steel with a 300pA aperture*



*Figure 37 - A large array of 4 arrays of 225 photonic crystals each milled on steel at 100pA. The data bar has an error – total milling time was closer to 145 hours for this array*



|         |       |              |     |          |                            |
|---------|-------|--------------|-----|----------|----------------------------|
| Mag     | Tilt  | HFW          | pA  | 10/24/14 | 2 $\mu$ m                  |
| 25.0 kX | 45.0° | 12.2 $\mu$ m | 344 | 10:54:32 | Steel PC 100pA 4*15*15*6um |

*Figure 38 – 45 degree tilt view of part of a large array of 4 arrays of 225 photonic crystals each milled on steel at 100pA*

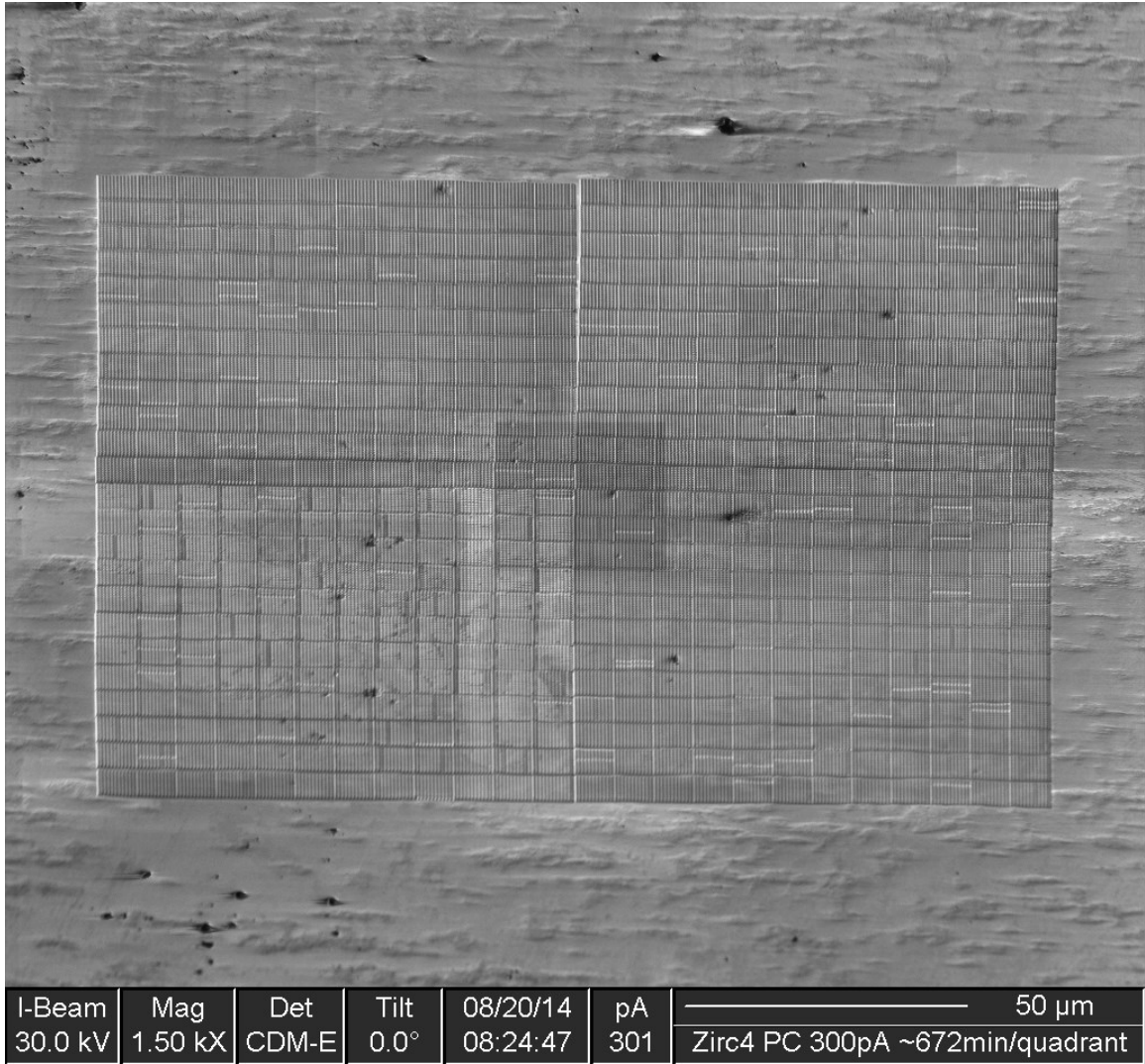


*Figure 39 - A large array of 4 arrays of 144 photonic crystals each milled on zircaloy-4 at 300pA*

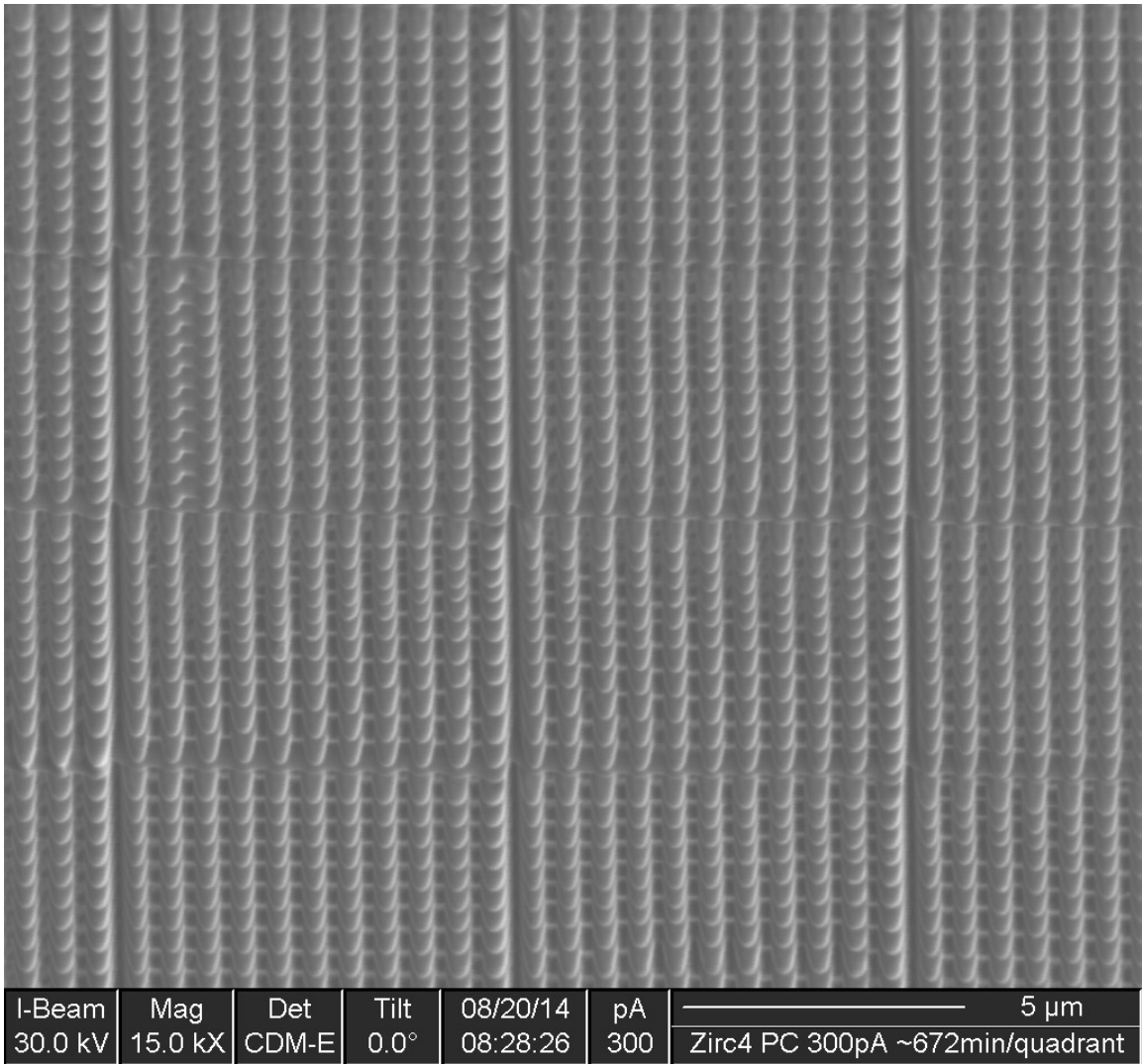


*Figure 40 - 45 degree tilt view of a section of a large array of photonic crystals milled on zircaloy-4 at 300pA*

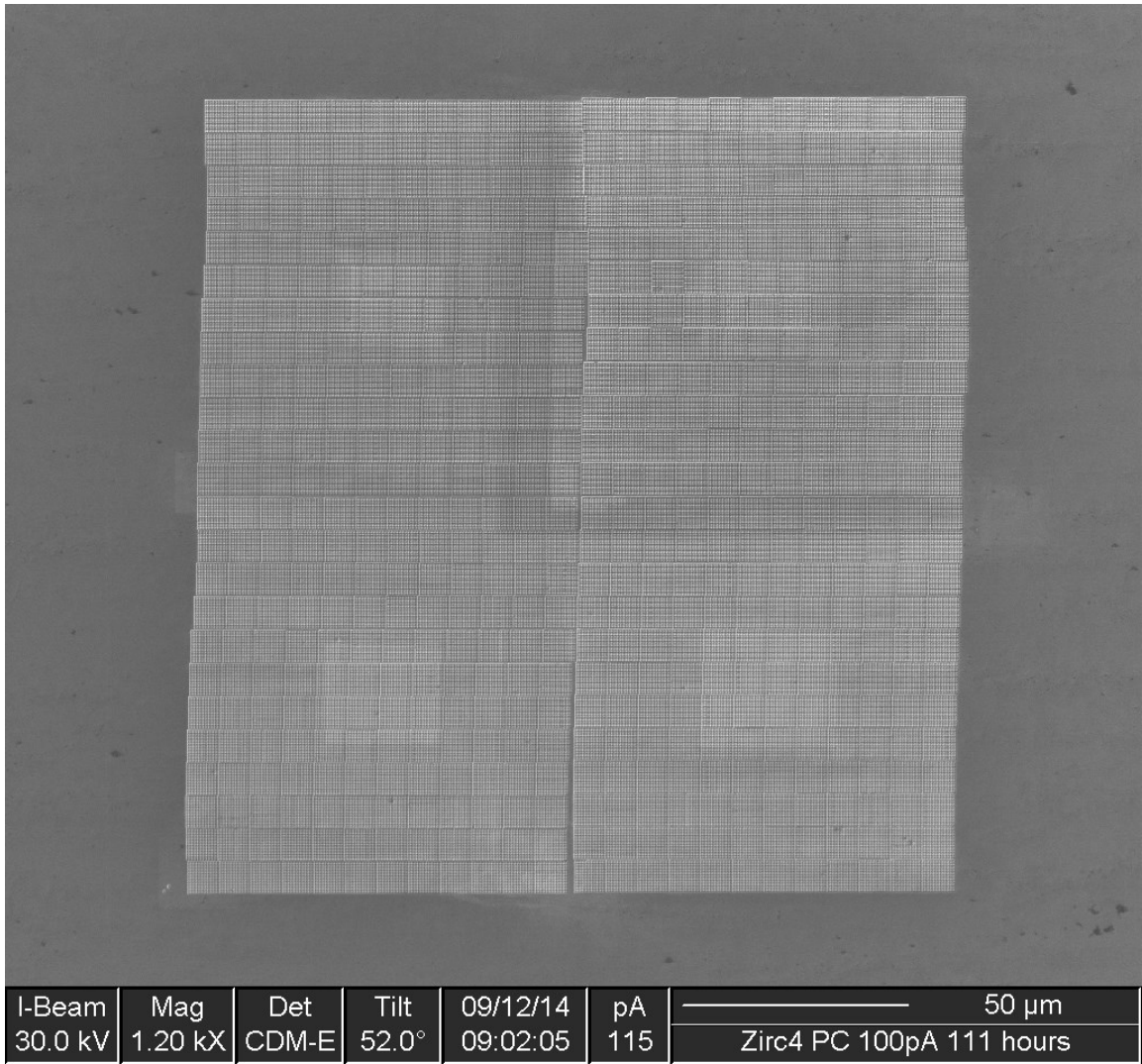


*Figure 41 - A large array of 4 arrays of 144 photonic crystals each milled on zircaloy-4 at 100pA*

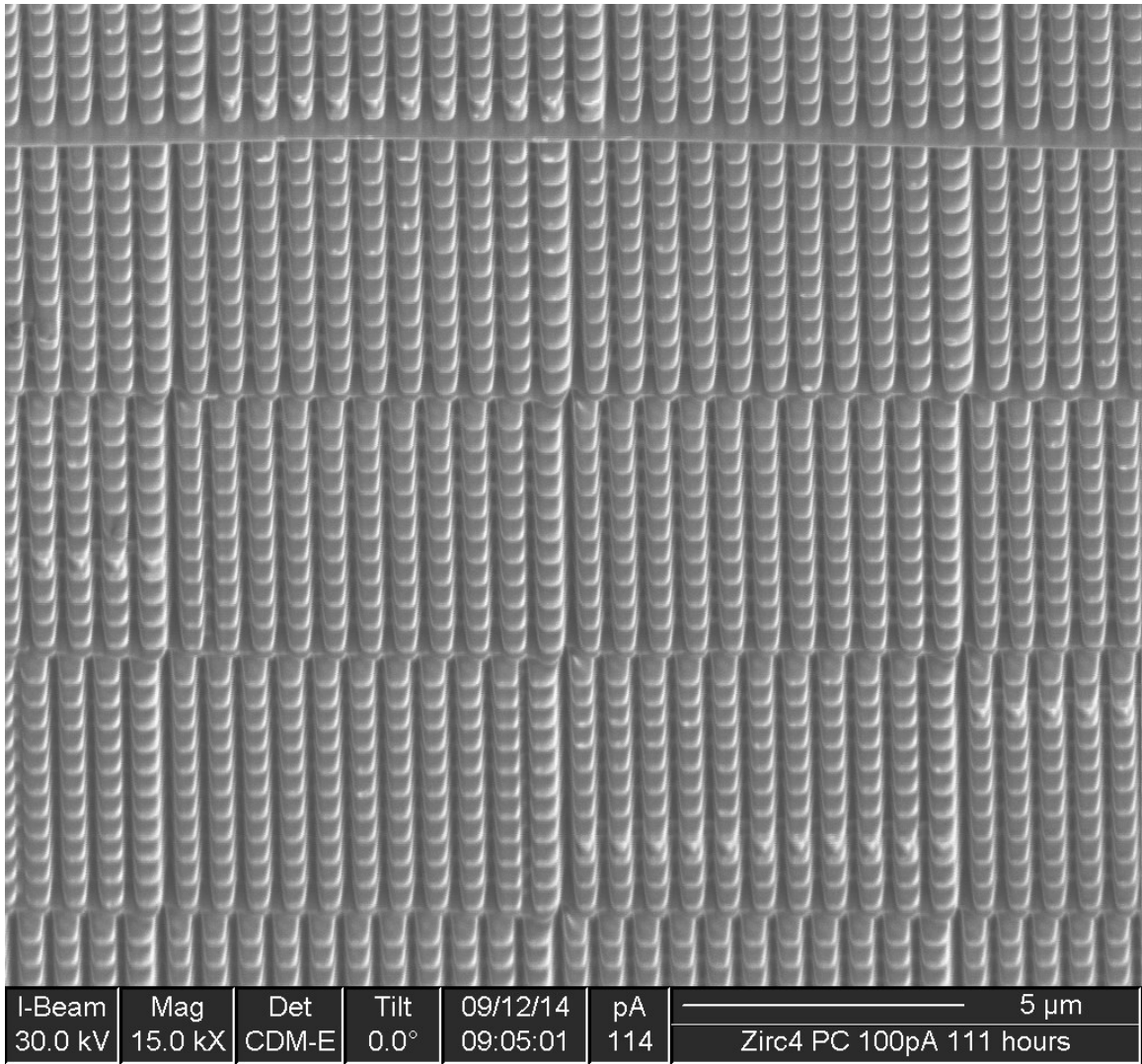


*Figure 42 - 45 degree tilt view of a section of a large array milled on zircaloy-4 at 100pA*

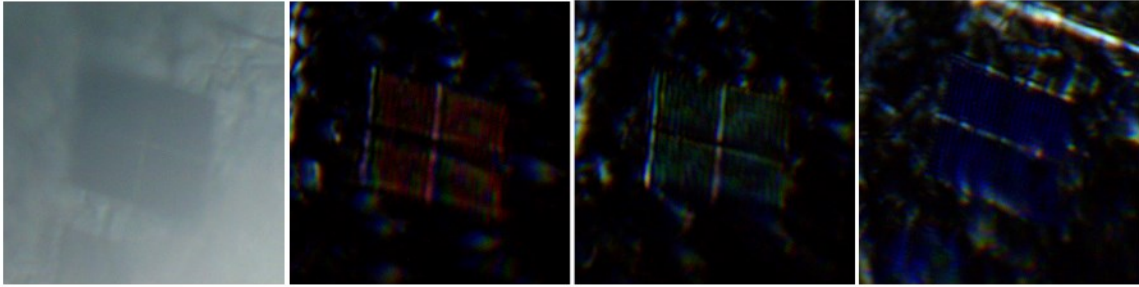


*Figure 43 – Optical micrographs of an array of photonic crystals on  $UO_2$  under top light (left) and varying oblique angles of optical illumination.*

### **5.1.2 Quality**

Geometric quality, how well the milled product conforms to the desired geometry, appears to be primarily dependent on the beam current (which controls the size of the beam) and also to some extent on the uniformity of the working material; it would appear that local changes in the hardness or composition of the working material can have a significant impact on final milled depth. Feature quality is clearly better at lower beam currents in both steel and zircaloy-4, with lower current yielding better quality down to at least 4pA.

The optical quality is of course dependent on the geometry of the photonic device. Interestingly, the photonic devices produced during the course of this thesis work appear to be fairly tolerant to geometry imperfections, a fact which certainly bears further investigation. Practically speaking, this error tolerance allows for larger crystals that are further from ideal but may still function sufficiently as photonic sensor devices.

### 5.1.3 Optical Response

One of the large arrays on steel was examined via optical interrogation. While the behavior of this device does not closely match simulation, there are interesting behaviors occurring; the device is not simply reflecting or absorbing light equally across the visible spectrum. The nature of this behavior bears further investigation.

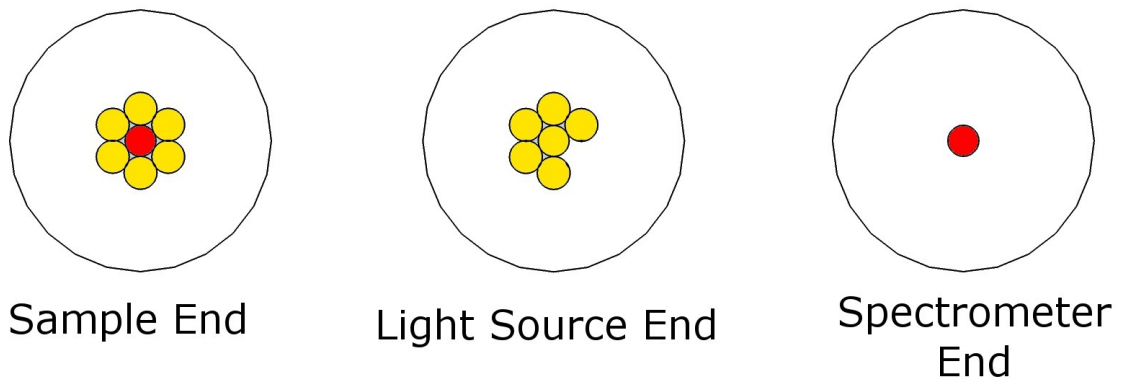


*Figure 44- A diagram showing the fiber layout of the reflection probe fiber bundle used for optical measurements*

The optical response of a large array photonic device on steel, milled at 100pA, was briefly investigated. These tests were conducted by observing the spectrum of the optical return at various angles using a custom test stand. The light source and sensor were collinear; a reflection probe fiber bundle was used. Figure 44, above, is a diagram of the layout of the fibers in the reflection probe bundle. The position of the fiber bundle for each sample was varied by theta and phi, with these angles defined as drawn in Figure 45.

It was assumed that the optical response would be symmetrical, which allowed for a decreased number of measurements.

Background measurements were obtained by moving the photonic crystal array out of the lit spot. This background spectrum was then subtracted from the optical response of the photonic array. In addition, a reflection spectrum was collected at 90 degrees on a polished, un-machined portion of the sample. The background subtracted response spectra were then divided by the reflection spectrum.

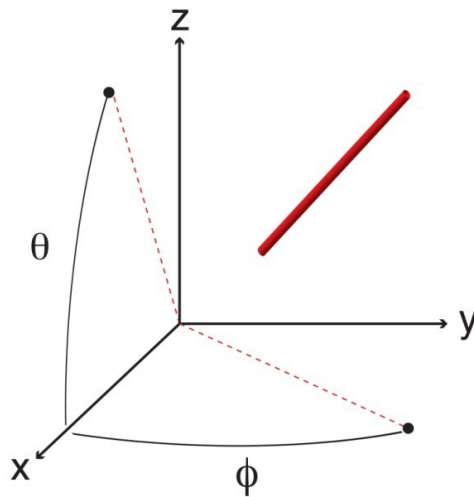


*Figure 45- A diagram defining the coordinate system used during optical measurements. The red line represents the fiber bundle reflection probe.*

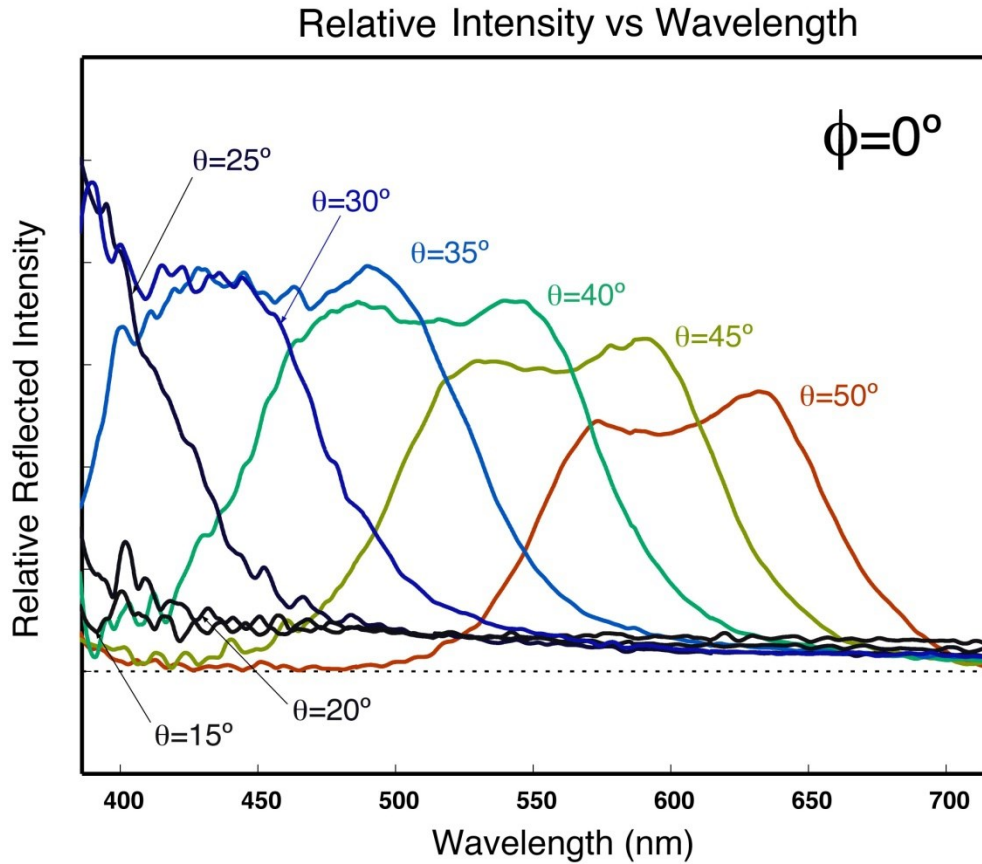


*Figure 46- Relative intensity graph of the response of a large array on steel, where phi was set to zero and theta varied.*

Figure 46 is a relative intensity plot for a measurement series on a large steel array milled at 100pA. Each spectrum was weighted and converted to a sRGB value. Figure 47 is a color plot of the response from the large array in steel milled at 100pA at a variety of angles in phi and theta.

# Optical response color plot

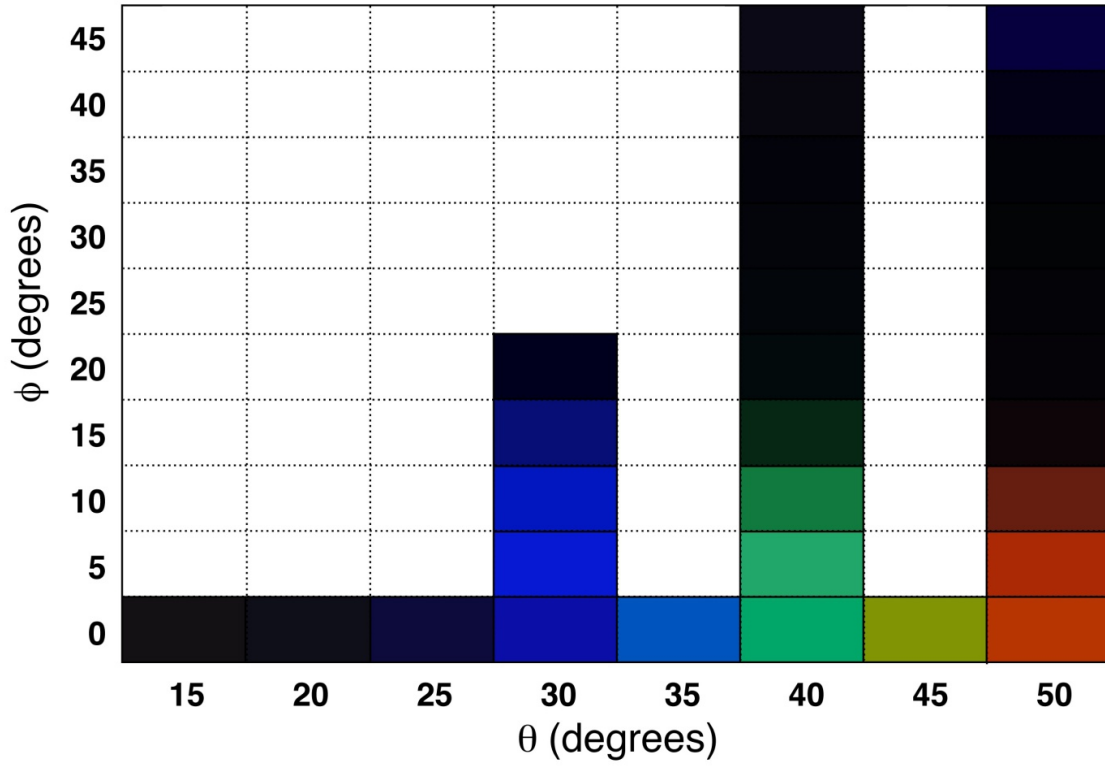


Figure 47- Color plot of the optical response of a large array on steel

## **5.2 Future Work**

### **5.2.1 Alternative Production Methods**

It is apparent that the FIB tool, while extremely useful for rapid prototyping on a variety of materials, is not well suited to large-scale production of large sensor devices. The milling time to obtain large, very high quality devices is simply too long for practical production. In order to obtain large devices, such as the 150  $\mu\text{m}$  to 200  $\mu\text{m}$  square devices discussed in this thesis, a significant sacrifice of crystal quality must be made to bring the production time to feasible levels. It is expected that when this work is continued, the decision will be made to move to fabrication techniques originally developed for the semi-conductor industry and modify them to function on the materials of interest. There are several techniques that may be considered.

The most promising potential technique is the Bosch process variant of reactive ion etching. This technique was developed to allow for very high aspect ratio trenches (many times deeper than they are wide) to be produced in semi-conductor materials. The Bosch process [26] uses an alternating cycle of etching and passivation. In preparation for etching, a hard mask on the surface is patterned to protect the material that does not need to be milled. The etch cycle begins to etch into the substrate where there is no hard mask. After a set period of time, etching is stopped and a passivation cycle is run in which a protective layer is deposited on the surfaces of the substrate. Due to the addition of energetic ion bombardment during passivation, no passivation layer can form on the bottom of the trench. Thus, the walls of the trench are protected while the bottom remains

exposed for the following etch cycle. The etching/passivation cycle is repeated at very short intervals until the desired depth is reached. The profile of trenches produced with this technique is scalloped, and the size and number of scallops is controlled by the switching frequency of the etch/passivation cycle; a shorter cycle yields a larger number of smaller scallops. An example of trenches produced via Bosch process can be seen in Figure 48.

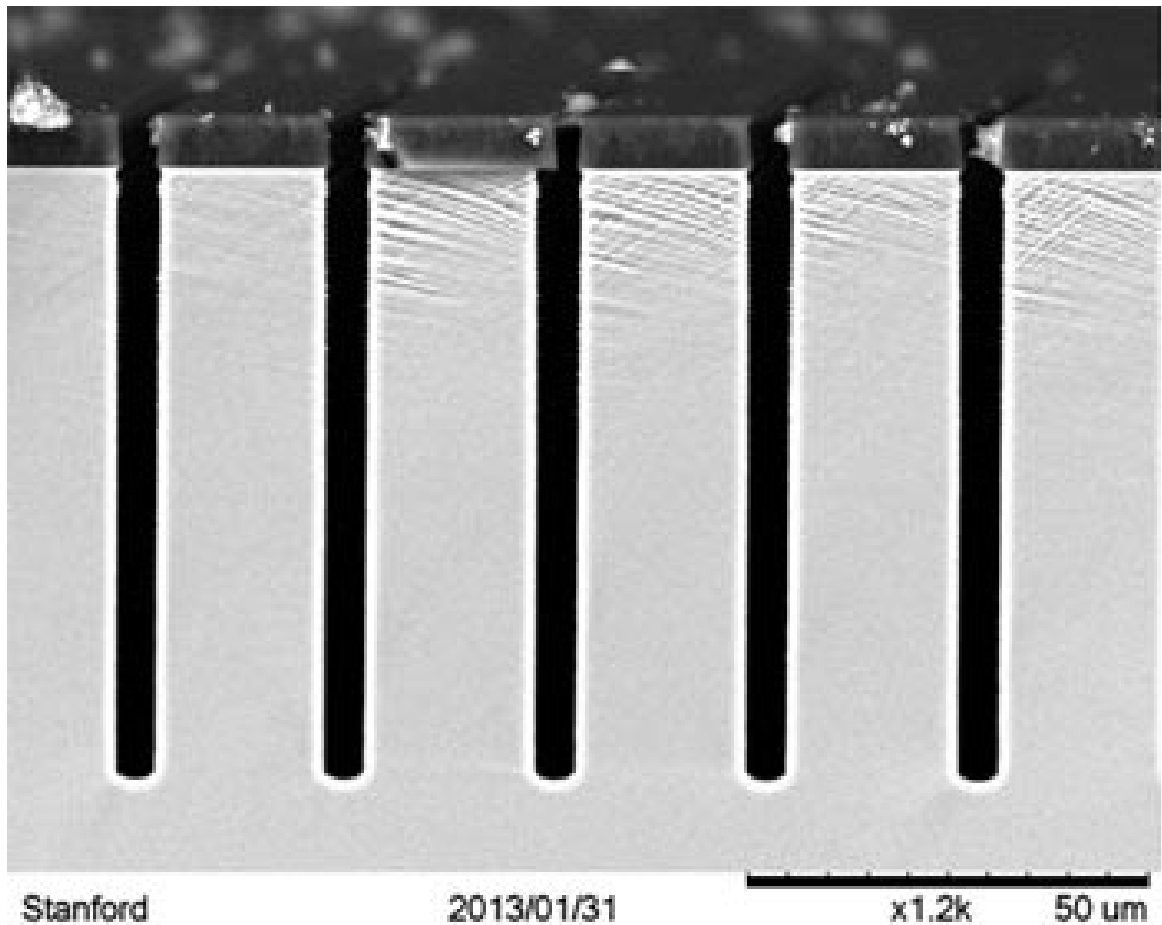


*Figure 48 - An example of deep silicon etching using a Bosch process etch [27]*

It is believed that a FIB should be able to mill through hard-mask material fairly quickly and uniformly, which would allow for quick prototyping of masks for Bosch process RIE use. There are also other methods of mask patterning that could be considered, such as the use of an electron beam lithography tool. Since the feature sizes necessary are smaller than some wavelengths of light, traditional photolithography is not feasible.

Another technique that may be considered is a deposition method. Rather than selectively removing material, a layer of photoresist is deposited and patterned such that there are holes in the photoresist where material is desired. The material comprising the photonic crystal is then deposited into these holes, and the photoresist subsequently chemically removed, leaving a lattice of pillars.

### **5.2.2 Photonic Crystal Error Tolerance**

The research conducted for this thesis has indicated that photonic crystals that are far from the ideal shape simulated during their design still appear to express readily detectable and interesting optical behaviors. This was an unexpected result and bears further investigation.

## **Glossary**

- BWR – boiling water reactor
- EDS – energy dispersive spectroscopy, a technique for semi-quantitatively analyzing the chemical composition of a sample in an electron microscope
- FDFD – finite difference, frequency domain
- FDTD – finite difference, time domain
- FEG – field emission gun, a type of electron source
- FEI – a corporation which produces various high power electron or ion microscope, including those used for this research
- FIB – focused ion beam
- GIS – gas injection system
- IEE – insulator enhanced etch
- IXRF – A corporation specializing EDS tools
- LMIS – liquid metal ion source
- LWR – light water reactor
- MEEP – MIT electromagnetic equation propagation
- MIT – Massachusetts Institute of Technology
- MOX – mixed oxide fuel, a nuclear fuel material composed of  $\text{UO}_2$  with admixtures of plutonium
- MPB – MIT photonic bands, a software package for simulating photonic band structures
- PC – photonic crystal

- PWR – pressurized water reactor
- RIA – radiation induced attenuation
- RIE – reactive ion etching
- SEM – scanning electron microscope
- TE – transverse electric, polarization
- TEM – transmission electron microscope
- TM – transverse magnetic, polarization
- UO<sub>2</sub> – chemical formula for uranium dioxide, a common nuclear fuel material

## Works Cited

- [1] J. J. Duderstadt and L. J. Hamilton, Nuclear Reactor Analysis, John Wiley & Sons, Inc., 1976.
  
- [2] "ATI Wah Chang Zirconium Alloy Zircaloy-4," matweb.com, [Online]. Available: <http://www.matweb.com/search/datasheet.aspx?matguid=a265da2e4ff94c968a8ae344870a32e3&ckck=1>. [Accessed 21 10 2014].
  
- [3] N. E. T. & M. S. Kazimi, Nuclear Systems I: Thermal Hydraulic Fundamentals, Washington, D.C.: Taylor & Francis, 1992.
  
- [4] J. & H. D. Martin, "A Recommendation for the Thermal Conductivity of UO<sub>2</sub>," *Journal of Nuclear Materials*, vol. 166, pp. 223-226, 1989.
  
- [5] World Nuclear Association, "Nuclear Fuel Fabrication," World Nuclear Association, September 2014. [Online]. Available: <http://www.world-nuclear.org/info/Nuclear-Fuel-Cycle/Conversion-Enrichment-and-Fabrication/Fuel-Fabrication/>. [Accessed 23 October 2014].
  
- [6] OMEGA, "OMEGA thermocouple guide," 6 October 2011. [Online]. [Accessed 31 July 2013].
  
- [7] Omega, Inc., "Revised Thermocouple Reference Tables, ANSI Type C, ANSI/ASTM E-230," [Online]. Available: <http://www.omega.com/temperature/Z/pdf/z239-240.pdf>. [Accessed 10 November 2014].

- [8] International Atomic Energy Agency, "Modern Instrumentation and Control for Nuclear Power Plants: A Guidebook," IAEA, Austria, 1999.
- [9] Hitec Products, Inc., "Data sheet for high temperature strain gauges," Hitec Products, Inc, 29 August 2012. [Online]. Available: [http://www.hitecprod.com/PDFfiles/HFPstraingage\\_datasheet.pdf](http://www.hitecprod.com/PDFfiles/HFPstraingage_datasheet.pdf). [Accessed 27 March 2014].
- [10] Vishay Precision Group, "Special Use Strain Gages - High-Temperature Strain Gages, Doc. 11532," 25 March 2011. [Online]. Available: <http://www.vishaypg.com/docs/11532/highpat.pdf>. [Accessed 27 March 2014].
- [11] NASA, "High-Temperature Thin-Film Strain Gauges," NASA, 2007.
- [12] G. Cheymol and B. Brichard, "Fiber Optics for Metrology in Nuclear Research Reactors - Applications to Dimensional Measurements," *IEEE Transactions on Nuclear Science*, vol. 58, no. 4, pp. 1895-1902, August 2011.
- [13] K. Haase, "Strain sensors based on bragg gratings," in *IMEKO 20th TC3, 3rd TC16 and 1st TC22 International Conference, Cultivating metrological knowledge*, Merida, Mexico, 2007.
- [14] J. D. Joannopoulos, S. G. Johnson, J. N. Winn and R. D. Meade, *Photonic Crystals Molding the Flow of Light*, Second ed., Princeton, NJ: Princeton University Press, 2008.

- [15] S. G. Johnson and A. I. P. Group, "MIT Photonic Bands," MIT, [Online]. Available: [http://ab-initio.mit.edu/wiki/index.php/MIT\\_Photonic\\_Bands](http://ab-initio.mit.edu/wiki/index.php/MIT_Photonic_Bands). [Accessed 27 March 2014].
- [16] L. Rayleigh, "On the remarkable phenomenon of crystallin reflexion described by Prof. Stokes," *Philisophical Magazine Series 5*, vol. 26, no. 180, pp. 256-265, 1888.
- [17] K. Hill, Y. Fujii, D. Johnson and B. Kawasaki, "Photosensitivity in optical fiber waveguides: Application to reflection filter fabrication," *Applied Physics Letters*, vol. 32, no. 10, 1978.
- [18] N. Bashara and Y. Peng, "Optical properties of Zircaloy and Zircaloy oxide by ellipsometry," *Applied Optics*, vol. 19, no. 18, pp. 6245-3251, 15 September 1985.
- [19] S. Hongliang, C. Mingfu and Z. Ping, "Optical properties of UO<sub>2</sub> and PuO<sub>2</sub>," *Journal of Nuclear Materials*, vol. 400, pp. 151-156, 2010.
- [20] G. Boisset, "luxpop list of index of refraction data," [Online]. Available: [http://luxpop.com/RefractiveIndexList\\_v2.html](http://luxpop.com/RefractiveIndexList_v2.html). [Accessed 27 March 2014].
- [21] "DTU Fotonik - Department of Photonics Engineering," Technical University of Denmark, 19 May 2013. [Online]. Available: <http://www.fotonik.dtu.dk/english/Research/Nanophotonics/Nanodev/Silicon-photonics>. [Accessed 15 October 2014].
- [22] G. F. Strouse, "Standard Reference Material 1751: Gallium Melting-Point Standard," National Institute of Standards and Technology, Gaithersburg, MD

20899-8363, 2004.

- [23] FEI, Inc., "FEI Components," [Online]. Available: <http://www.fei.com/components/>. [Accessed 21 10 2014].
- [24] S. R. a. R. Puers, "A review of focused ion beam applications in microsystem technology," *Journal of Micromechanics and Microengineering*, vol. 11, no. 4, p. 287, 12 January 2001.
- [25] D. Gerace and L. C. Andreani, "Effects of disorder on propagation losses and cavity Q-factors in photonic crystal slabs," *Photonics and Nanostructures - Fundamentals and Applications*, vol. 3, no. 2-3, pp. 120-128, 2005.
- [26] F. Laermer and A. Schilp, "Method of Anisotropically Etching Silicon". United States Patent 5501893, 26 March 1996.
- [27] J. Snapp, "Deep Silicon Etching at Stanford-Plasma Therm Versaline DSE," Stanford Nanofabrication Facility, [Online]. Available: <http://www.nnin.org/research-support/process-blog/deep-silicon-etching-stanford-plasma-therm-versaline-dse>. [Accessed 22 10 2014].
- [28] J. Lamarsh and A. Baratta, Introduction to Nuclear Engineering, 3 ed., Prentice Hall, 2001, p. 783.
- [29] G. Veronis, R. W. Dutton and S. Fan, "Metallic photonic crystals with strong broadband absorption at optical frequencies over wide angular range," *Journal of*

*Applied Physics*, vol. 97, 2005.

- [30] P. Johnson and R. Christy, "Optical constants of transition metals: Ti, V, Cr, Mn, Fe, Co, Ni, and Pd," *Physical Review B*, vol. 9, no. 12, pp. 5056-5070, 15 Jun 1974.
- [31] V. Kuzmiak, A. Maradudin and F. Pincemin, "Photonic band structures of two-dimensional systems containing metallic components," *Physical Review B*, vol. 50, no. 23, pp. 16835-16844, 15 December 1994.
- [32] V. Krishnamurthy, B. Klein, M. Messer, C. Wang and J. Allen, "Robust and optimum designs of non-linearly tapered slow light couplers," *Journal of Optics A: Pure and Applied Optics*, vol. 11, no. 4, 2009.
- [33] C. Luo, S. G. Johnson, J. Joannopoulos and J. Pendry, "Negative refraction without negative index in metallic photonic crystals," *Optics Express*, vol. 11, no. 7, pp. 746-754, 7 April 2003.